5-2012

On the Effect of Elasticity on Drag Reduction Due to Polymer Additives Using a Hybrid D.N.S. and Langevin Dynamics Approach

Arnout Boelens
University of Massachusetts Amherst, aboelens@uchicago.edu

ON THE EFFECT OF ELASTICITY ON DRAG REDUCTION DUE TO POLYMER ADDITIVES USING A HYBRID D.N.S. AND LANGEVIN DYNAMICS APPROACH

A Dissertation Presented

by

ARNOUT BOELENS

Submitted to the Graduate School of the
University of Massachusetts Amherst in partial fulfillment
of the requirements for the degree of

DOCTOR OF PHILOSOPHY

May 2012

Chemical Engineering

ON THE EFFECT OF ELASTICITY ON DRAG REDUCTION DUE TO POLYMER ADDITIVES USING A HYBRID D.N.S. AND LANGEVIN DYNAMICS APPROACH

A Dissertation Presented

by

ARNOUT BOELENS

Approved as to style and content by:

M. Muthukumar, Chair

T.J. Mountziaris, Member

J. Machta, Member

D. Maroudas, Member

J.B. Perot, Member

T.J. Mountziaris, Department Chair
Chemical Engineering

ACKNOWLEDGMENTS

It is a pleasure to thank those who made this thesis possible. First of all I would like to thank Muthu, my adviser, for all his support and insight, and my committee members: Prof. Mountziaris, Prof. Machta, Prof. Maroudas, and Prof. Perot. I am especially grateful to Prof. Perot, who helped me on my way parallelizing my code and always had great feedback. Furthermore I would like to thank my parents, family and girlfriend, Breanne, for all their support and encouragement. Last but not least a big thanks to all my friends, both inside and outside the Chemical Engineering department, because of whom I had a great time in Amherst.

ABSTRACT

ON THE EFFECT OF ELASTICITY ON DRAG REDUCTION DUE TO POLYMER ADDITIVES USING A HYBRID D.N.S. AND LANGEVIN DYNAMICS APPROACH

MAY 2012

ARNOUT BOELENS

B.Sc., DELFT UNIVERSITY OF TECHNOLOGY

M.Sc., DELFT UNIVERSITY OF TECHNOLOGY

Ph.D., UNIVERSITY OF MASSACHUSETTS AMHERST

Directed by: Professor M. Muthukumar

In this work the effect of elasticity on turbulent drag reduction due to polymers is investigated using a hybrid Direct Numerical Simulation (D.N.S) and Langevin dynamics approach. Simulations are run at a friction Reynolds number of $\mathrm{Re}_\tau = 560$ for 960.000 dumbbells with Deborah numbers of $\mathrm{De} = 0$, $\mathrm{De} = 1$, and $\mathrm{De} = 10$. The conclusions are that it is possible to simulate a drag reduced flow using hybrid D.N.S. with Langevin dynamics, that polymers, like other occurrences of drag reduction, reduce drag through streak stabilization, and that the essential property of polymers and fibers in having a drag reducing effect is their ability to exert a torque on the solvent when they orientate in the boundary layer of the turbulent flow.

CONTENTS

LIST OF TABLES

Table **Page**

LIST OF FIGURES

Figure **Page**

LIST OF SYMBOLS

Symbol		Page
$\bar{u}_1$	Bulk velocity of the solvent	7
μ_1	Dynamic solvent viscosity	25
ν_1	Kinematic solvent viscosity	3
ϕ	Angular direction vector	26
ρ^*	ρ_1/ρ_2	28
ρ_1	Density of the solvent	3
ρ_2	Density of the dumbbell beads	3
σ_2	Polymer stress tensor	84
τ_2	Particle relaxation time	28
τ_2	Polymer torque	84
τ_w	Wall shear	3
τ_Z	Zimm relaxation time	28
De	Deborah number	6
Re	Bulk Reynolds number	7
Re_τ	Friction Reynolds number	7
υ_2	Polymer stretch	84
$\mathbf{f}_B$	Body forces on the solvent	25
$\mathbf{f}_R$	Random force	27
$\mathbf{u}_1$	Solvent velocity vector	25
$\mathbf{x}_{2,0}$	Equilibrium distance between dumbbell beads	27
$\mathbf{x}_{2,\mathrm{Max}}$	Maximum extension between dumbbell beads	27

INTRODUCTION

When, with increasing Reynolds number, a Newtonian fluid transitions from laminar flow to turbulent flow, there is a big increase in energy losses due to dissipation at the Kolmogorov scales. However, by adding only a couple of parts per million of certain polymers to the fluid, drag reduction of up to 80 percent can be observed (Gampert & Wagner 1982).

Since the discovery of drag reducing polymers in 1948 by Toms (1948), numerous experiments and simulations have been performed (Virk et al. 1967, Rudd 1969, Den toonder et al. 1997, Sureshkumar et al. 1997). Also, drag reduction due to polymer additives has found applications in the form of adding polymers to fluids to save on the energy bill when pumping them around (Burger et al. 1980), or injecting polymers in front of a ship haul in order to save fuel (Vogel & Patterson 1964, Canham et al. 1970). However, the physics behind drag reduction, also know as the Toms effect, is still unknown.

In this work the effect of elasticity of the polymer additives on drag reduction is investigated using a hybrid Direct Numerical Simulation (D.N.S.) with Langevin dynamics approach. The questions that are addressed are: i) is it possible to observe drag reduction using only first principles i.e. using D.N.S. with Langevin dynamics instead of the more common FENE-P continuum approach. ii) can drag reduction due to polymer additives be placed in a broader context of drag reducing phenomenon, and iii) how do polymers influence the physics of drag reduction? In answering these questions, more insight is gained in turbulent drag reduction in general and in the hydrodynamic interaction with polymers in particular. From an engineering

perspective this study aims to give a better idea of which material properties to look at for better drag reducing agents.

CHAPTER 1

LITERATURE

Since the discovery of drag reducing polymers by Toms (1948), numerous experiments and simulations have been performed. However, as is also mentioned by Gampert & Wagner (1982), reviewing existing literature it can be found that there are a lot of contradicting results. For the experimental work this can be attributed to the difficult nature of performing drag reduction experiments: i) To measure the drag reduction capabilities of a polymer of a certain molecular weight, it is important to use a polymer sample which is as close as possible to having a monodisperse molecular weight distribution, and purification of a large amount of polymers is a difficult process (Nadolink 1987). ii) Properties like relaxation time, Kuhn length, and molecular weight, are important physical properties which all have their influence on the polymer/solvent interactions. Unfortunately, these quantities are very often not available in literature (Sreenivasan & White 2000) . iii) Due to high shear rates resulting from pumping the solvent around, polymers typically degrade quickly in experimental setups. To reduce this effect special equipment is needed (Den toonder et al. 1997), and the polymers need to be characterized again after the experiment (Nadolink 1987).

Numerical simulations have been able to generate a lot of new insight into the physics behind drag reduction, but have not been able to generate very consistent answers either. Some of the encountered problems are: i) Which model has to be used for the polymer phase and are all the essential physics captured in this model? The polymers can be modeled as a continuum using, for example, the Oldroyd-B model

(Min et al. 2003) or the Finitely Extensible Nonlinear Elastic model with Peterlin closure (FENE-P) (Ptasinski et al. 2003), or the polymers can be simulated as a discrete phase using Brownian or Langevin dynamics (Peters & Schumacher 2007). ii) Although computers have become faster and faster there are still severe limitations to the Reynolds numbers which can be reached and the amount of polymer molecules that can be simulated (Dubief et al. 2005). iii) A lot of data can be generated and a lot of variables are accessible that are out of reach in traditional experiments. However, they this is not of any use, when one does not know what to look for (White & Mungal 2008).

In the below sections an overview is given of the experimental and computational findings on drag reduction and a summary is given of the different theories that have been proposed to describe this phenomenon. Also, an overview can be found in the review articles of Lumley (1969), Liaw et al. (1971), Hoyt (1972), Landahl (1973), Virk (1975), and White & Mungal (2008).

1.1 Scaling

Because they scale with different length and time scales, an important way of classifying different phenomena in turbulence. is whether it is a bulk (core region) or a wall phenomenon (Tennekes & Lumley 1972). Far away from the wall, in the bulk, turbulence is dominated by the behavior of large eddies. Because of this, bulk phenomena are dominated by the behavior of these same eddies, and scale with their characteristic length and time scales. Close to the wall viscous dissipation and wall shear are dominant, and thus wall phenomena scale with their own characteristic length and time scale, based on viscosity and wall shear.

Since the maximum size an eddy in the bulk can reach is of the order of the domain size, in the case of pipe flow the pipe diameter, the characteristic length scale for bulk phenomena is the diameter, d_1. The characteristic velocity is the friction velocity,

which is defined as:

$$u_\tau = \sqrt{\frac{\tau_w}{\rho_1}} \tag{1.1}$$

with ρ_1 the density and τ_w the wall shear. This gives a turnover time for the eddies which is equal to the diameter divided by the friction velocity, d_1/u_τ, and means that bulk phenomena scale and can be non-dimensionalized, with the diameter, d_1, and the friction velocity, u_τ.

Outside the bulk, due to the proximity of the wall, eddies can never reach their maximum size and, close enough to the wall, the physics of turbulence are dominated by viscosity. The corresponding length and time scales are ν_1/u_τ, and ν_1/u_τ^2, where ν_1 is the kinematic viscosity and u_τ is the friction velocity again. Variables made non-dimensional with ν_1 and u_τ are said to be expressed in "wall units", while non-dimensionalizing with d_1 and u_τ is called using "bulk units".

Now, in order to know how to properly scale a simulation or experiment involving drag reduction, one needs to know whether it is a wall or a bulk phenomenon, a question which has received quite some debate over the years. For example, De Gennes (1986, 1990) his elastic theory considers drag reduction a universal phenomenon occurring both in the bulk and at the wall. Also, experiments injecting polymers in the flow at different locations to see when drag reduction would occur by McComb & Rabie (1979) and Bewersdorff et al. (1993) hinted at drag reduction being universal. Experiments by Cadot et al. (1998) and Reischman & Tiederman (1975) on the other hand, clearly point in the direction of drag reduction being a wall phenomenon. Also theoretical work by Joseph (1990) and Procaccia et al. (2008) considers drag reduction to be a wall phenomenon. Sreenivasan & White (2000) acknowledges De Gennes (1986) his point of view, that polymer solvent interaction occurs everywhere in the flow, but states that drag reduction is a wall phenomena simply because stresses are the highest close to the wall.

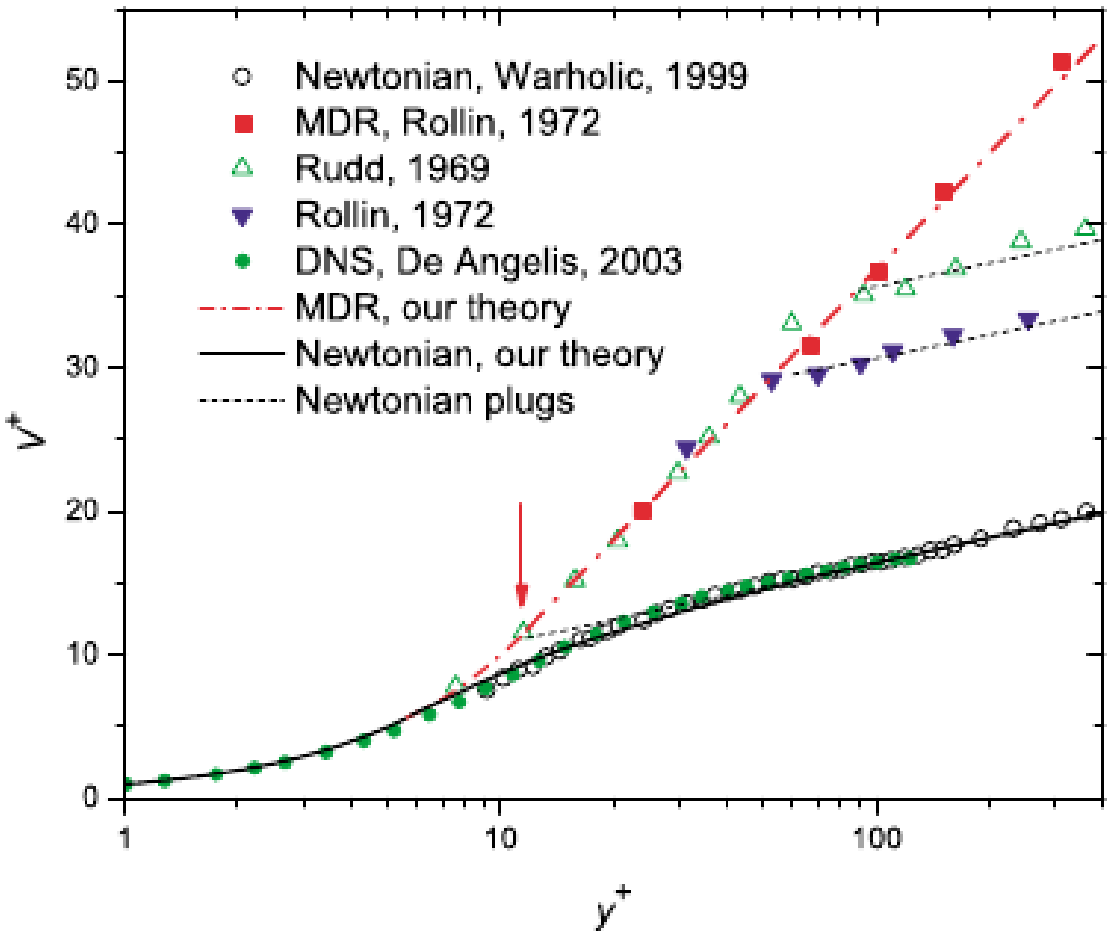

Figure 1.1 – Different velocity profiles scaled with wall units ν and u_τ. The line labeled "MDR" is the velocity profile that would be followed if drag reduction had hit the MDR asymptote, and different velocity profiles are shown which deviate from the MDR, to return to the so called Newtonian plug. (L'vov et al. 2004)

In this work drag reduction is considered a wall phenomenon, and the reason for this can be seen when looking at experimental drag reduction data like the velocity profiles shown in figure 1.1. When using wall units to display drag reduction data, universal curves seem to appear. Close to the wall the boundary layers are universal, and in the bulk the velocity profiles for the different measurements run parallel to the curve for the Newtonian velocity profile. When drag reduction is occurring, different measurements follow the same Maximum Drag Reduction (MDR) curve

before starting to run parallel to the curve for the Newtonian velocity profile again i.e. the return to the Newtonian plug. If this plot were to be scaled with the pipe diameter instead, there would not be one MDR curve for the different measurements. Because of this scaling with wall units, it seems a good assumption to consider drag reduction due to polymer additives a wall phenomenon.

1.2 Time and length scales

One of the early discussions, to understand the physics of drag reduction, was whether it was a phenomenon that resulted from the large size of polymer molecules or because of their long relaxation times (i.e. length scales versus time scales). Because even when they are fully stretched, they are smaller than the Kolmogorov length scale, the smallest length scale in turbulent flow, Lumley (1969) concluded that the length of polymers chains could not be responsible for their drag reducing effect. However, the kolmogorov time scale of the turbulent flow field can be smaller than the relaxation time of long enough polymers. It is believed that drag reduction stems from this overlap of time scales.

When looking at laminar flow of a polymer solution, one can observe that for the solvent to have an influence on polymers they need to fulfill the so called "time criterion" (e.g. Hershey & Zakin (1967), Lumley (1969) and Berman (1977*b*)). This criterion states that smallest time scale of the solvent flow field, the inverse shear rate, needs to be smaller than longest relaxation time scale of the polymer.

Generally the criterion is written in a form which requires the Deborah number to be larger than unity (e.g. Procaccia et al. (2008)), with the Deborah number defined as:

$$\mathrm{De} = \frac{t_2}{t_1} \tag{1.2}$$

Here t_2 is the characteristic time scale of the polymer, often taken to be the Zimm relaxation time, and t_1 is the characteristic time scale of the solvent, the kolmogorov

time scale. The Deborah number is used to describe flows with a non-constant stretch history, and physically represents the rate at which elastic energy is stored or released (Bird et al. 1987).

1.3 Concentration

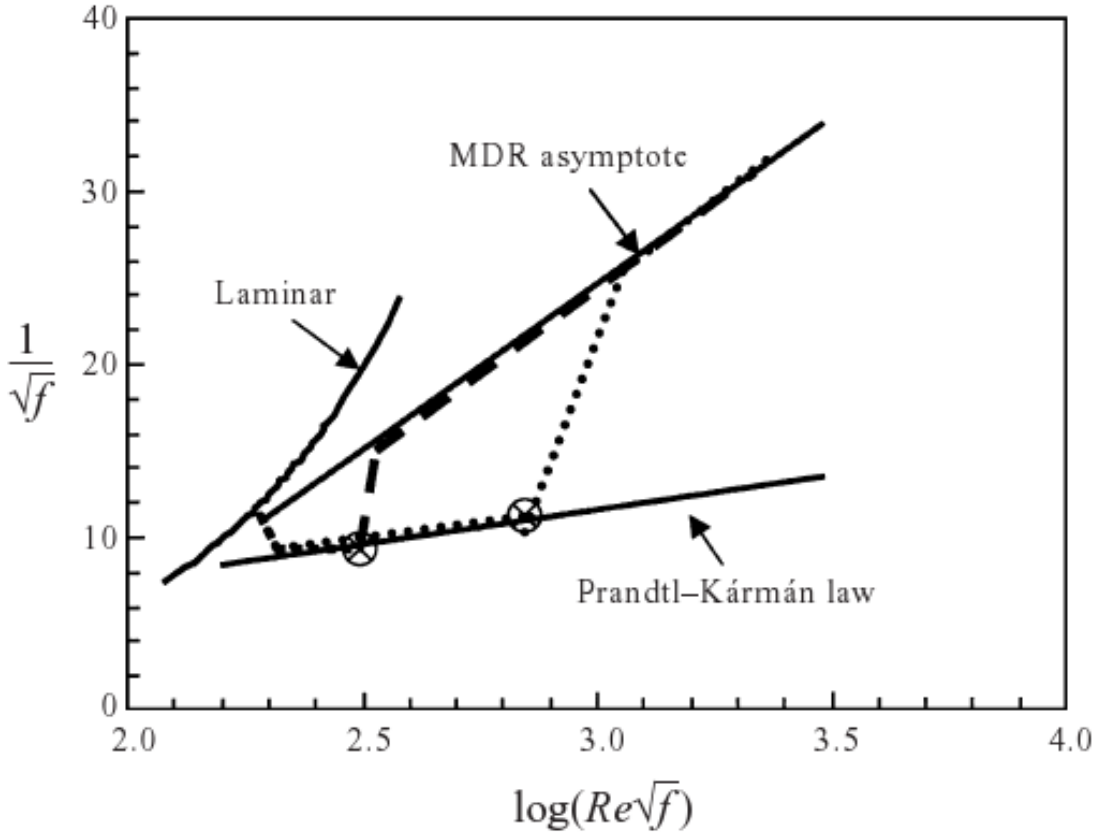

Figure 1.2 – Onset of drag reduction and the MDR asymptote. A schematic illustrating the onset of drag reduction and the maximum drag-reduction asymptote. The Prandtl-Kármán law corresponds to the turbulent flow of Newtonian fluids. The dotted and dashed lines represent qualitatively the friction factor behavior when a small amount of polymer is mixed with the fluid. The dashed line is for a larger polymer concentration. The line marked MDR asymptote represents the empirically observed limit on polymer drag reduction. (Sreenivasan & White 2000)

To show the influence of concentration on drag reduction, in figure 1.2 a schematic representation of what is called a Prandtl-Kármán plot is shown. As is derived in

appendix A, apart from showing the relation between $1/\sqrt{f}$ and $\mathrm{Re}\sqrt{f}$, where f is the friction factor and Re is the bulk Reynolds number, this type of graph can also be interpreted as showing the bulk velocity scaled with the friction velocity, $\bar{u}_1^+$, as function of the friction Reynolds number, Re_τ, for different flow regimes.

For low Reynolds numbers, for both Newtonian liquids and polymer solutions, the flow is laminar, and the bulk velocity depends on the friction Reynolds number as:

$$\bar{u}_1^+ = \frac{\mathrm{Re}_\tau}{16} \tag{1.3}$$

However, with increasing Reynolds number, the non-linear advective term of the Navier-Stokes equation will become stronger and stronger and eventually dominate the diffusive term, which results in a transition from laminar flow to turbulent flow. From there on, in the case of Newtonian liquids, the non-dimensional bulk velocity depends on the friction Reynolds number following a relationship called the Prandtl-Kármán law (Pope 2000).

When drag reducing polymers are added, creating a non-Newtonian liquid, quite different behavior can be observed. The dotted and the dashed curves represent the changed dependence of the non-dimensional bulk velocity on the friction Reynolds number when a small amount of polymers with drag reducing capabilities is added to a Newtonian liquid. The dotted line shows this dependence for a low polymer concentration and the dashed line for a high polymer concentration. When these polymers are added to the liquid, initially the fluid will behave like a normal Newtonian liquid, but when a high enough Reynolds number is reached, the bulk velocity starts to deviate from the Prandtl-Kármán law. A higher bulk velocity is observed while the friction Reynolds number is kept constant i.e. drag reduction is occurring.

This also introduces the question of whether there is a critical polymer concentration for drag reduction. If the concentration is low enough, will there be a point when drag reduction does not occur, independent of how high the friction Reynolds number

is? Paterson & Abernath (1970) and others (e.g. Nadolink (1987) and Sreenivasan & White (2000)) have observed a dependence of the onset of drag reduction on concentration and this dependence is also predicted by De Gennes (1990). However, the dependence on concentration is almost never as clearly observed as in figure 1.2, and sometimes is not at all. According to Virk (1975) there is no critical onset concentra-

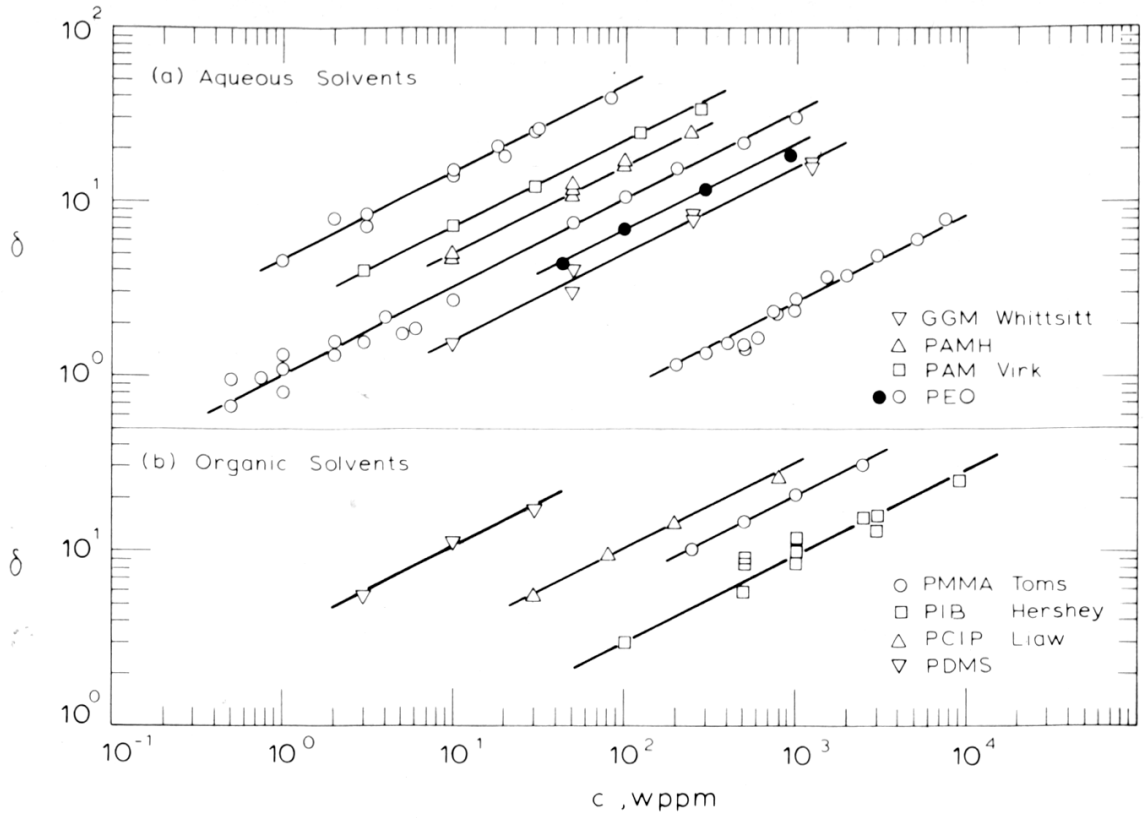

Figure 1.3 – Virk's concentration correlation. A graph by Virk (1975) showing the correlation between concentration and the slope difference, in a Prandtl-Kármán plot, between the curve of a solvent with polymers added and the slope of the Prandtl-Kármán law.

tion. He found a relation between drag reduction and concentration which is shown in figure 1.3. When plotting the drag reduction data in a Prandtl-Kármán plot, he found that:

$$S_2 - S_1 \propto \sqrt{c} \tag{1.4}$$

where S_1 is the slope of the Prandtl-Kármán logarithmic law, S_2 is the slope of the drag reduced curve, and c is the polymer concentration. From this correlation a relation can be derived of how the change in the bulk velocity in wall units depends on polymer concentration. A straight line in a Prandtl-Kármán plot can be written as:

$$\frac{1}{\sqrt{f}} = S \log\left(\mathrm{Re}\sqrt{f}\right) + C \tag{1.5}$$

Where S is either S_2 or S_1, and C equals C_2 or C_1. Assuming that f is the Fanning friction factor, this is equal to:

$$\frac{\bar{u}_1^+}{\sqrt{2}} = S \log\left(\mathrm{Re}_\tau\right) + C' \tag{1.6}$$

where $C' = C + S \log\left(\sqrt{2}\right)$. Subtracting the curves for the drag-reduced flow and the pure solvent flow gives:

$$\frac{\Delta\bar{u}_1^+}{\sqrt{2}} = (S_2 - S_1) \log\left(\mathrm{Re}_\tau\right) + (C_2' - C_1') \tag{1.7}$$

Since $S_2 - S_1 \propto \sqrt{c}$, and because the velocity difference has to go to zero when either the polymer concentration goes to zero or when the friction Reynolds number is equal to the Reynolds number where the MDR asymptote and the Prandtl-Kármán law cross, $\mathrm{Re}_\tau = \mathrm{Re}_\tau^0$, this expression can be written as:

$$\Delta\bar{u}^+ \propto \sqrt{c} \log\left(\frac{\mathrm{Re}_\tau}{\mathrm{Re}_\tau^0}\right) \tag{1.8}$$

Because Maximum Drag Reduction is independent of concentration, this correlation cannot be right in the MDR limit, but if it correcly describes the onset of drag reduction, this means that there is probably no critical onset concentration or only a very small one. As an alternative explanation why a critical concentration is found

in some experiments, Virk (1975) suggests that the turbulent flow field might not have been fully developed yet when the measurements were performed. Experiments by Warholic et al. (1999) show drag reduction for extremely low concentrations, but data also depend on how the polymer was injected, which, again, might indicate not fully developed flow.

1.4 Maximum drag reduction

Another unexplained aspect of drag reduction can also be seen in figure 1.2. At a fixed friction Reynolds number the drag can be reduced, and thus the bulk velocity increased, by adding more polymer to the solution, but at some point the bulk velocity will stop increasing and reaches the Maximum Drag Reduction (MDR) asymptote. In itself it is not surprising that there is a limit to how much drag can be reduced by increasing the concentration, because above the critical concentration polymer-polymer interaction will become important and change the physics of the flow. However, the interesting part is that the MDR asymptote is independent of the kind of polymer used, chain length, Kuhn length, solvability, or how much polymer is added to the solvent. Drag reduction does not get past the MDR asymptote, and trying to go past the MDR asymptote results in a return to laminar flow. The MDR asymptote can, for example, be observed in the data from Nadolink (1987) or the experimental data collected by (Virk 1975). As stated by Sreenivasan & White (2000), being able to describe the MDR asymptote would be a limiting behavior that any theory on drag reduction would have to be able to describe.

1.5 Molecular weight (distribution)

The molecular weight of the polymer additive is an important parameter in drag reduction. Experiments by Merrill et al. (1966) showed early on that long polymer chains are more effective as drag reducing agents than short polymer chains. Also,

Lumley (1969, 1973) suggested that a long enough relaxation time of the polymer is critical for the onset of drag reduction, which was confirmed by measurements of Berman & George Jr (1974). Berman (1978) mentions that typically a molecular weight above 10^5 is needed to be able to observe drag reduction. In figure 1.4 data is shown for two different polymer samples with about the same molecular weight, but one of which has a high molecular weight tail in its weight distribution. Consistently with the predictions made by Lumley (1969) and in agreement with earlier measurements by Huntson & Reischman (1975) and Berman (1977*a*), Nadolink (1987) also finds that a high molecular weight tail causes a polymer sample to have better drag reducing properties. Nevertheless, although the importance of molecular weight is understood, an exact dependence of drag reduction on molecular is weight still not known. As is also mentioned above, there are two reasons for this: i) it is very challenging to get a monodispersed enough sample to really investigate the influence of one molecular weight, and ii) even if the sample was fully characterized or even monodisperse, as was found by Paterson & Abernath (1970) and Fisher & Rodriguez (1971), the drag reducing capabilities of the sample deteriorate over time due to mechanical degradation resulting from pumping the fluid around, and the molecular weight distribution will not be the same anymore as when the polymer sample was added to the solvent.

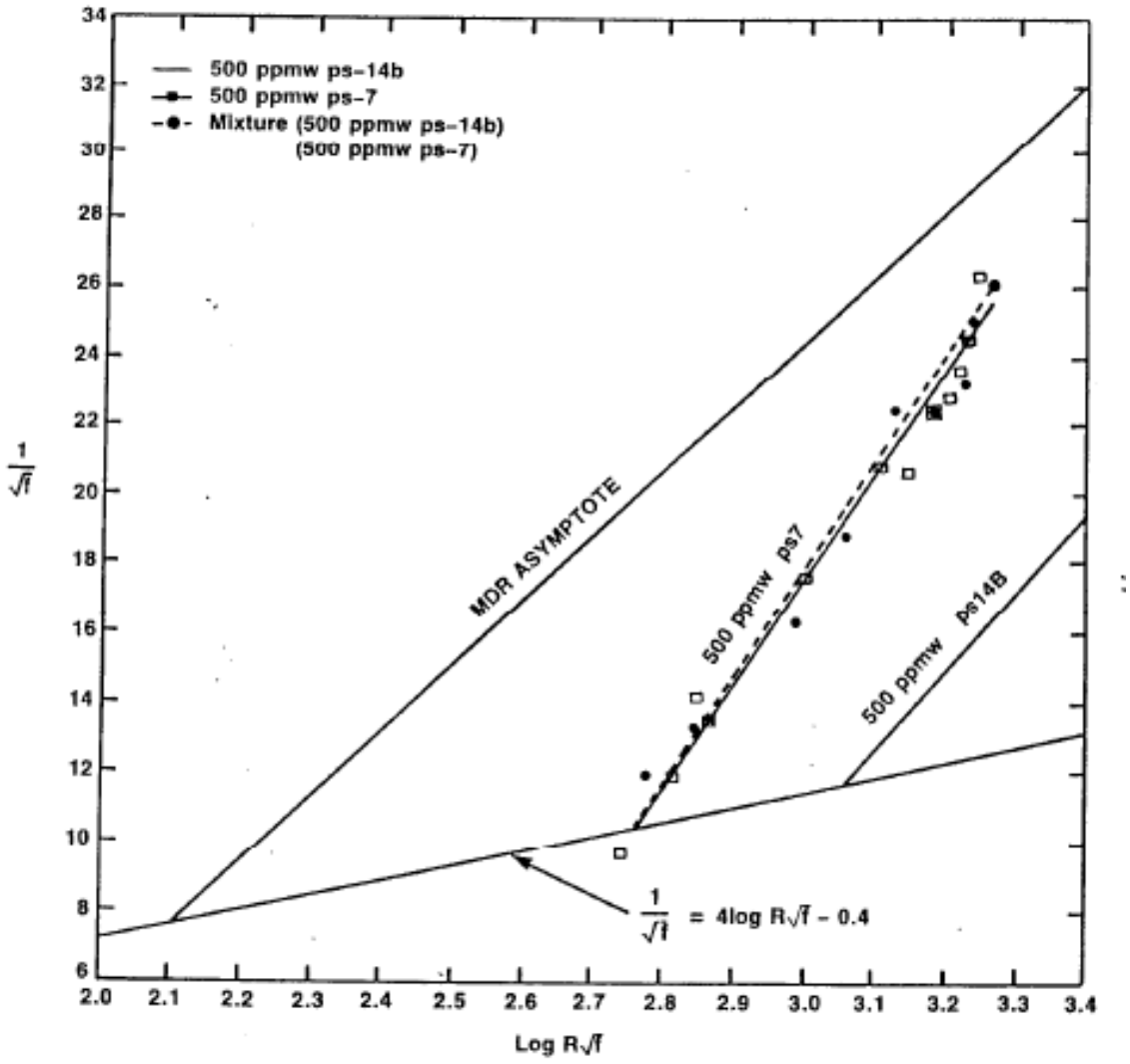

Figure 1.4 – **Effect of molecular weight distribution on drag reduction.** A Prandtl - Kármán plot by Nadolink (1987) showing the influence the of molecular weight distribution on drag reduction. The polymer sample with a high molecular weight tail shows better drag reducing capabilities than the sample without.

1.6 Elongational and elastic viscosity

Another still ongoing discussion is whether drag reduction is caused by elongational or elastic viscosity. Elongational viscosity, or extensional viscosity, is the viscosity coefficient of a non-Newtonian fluid when an extensional stress is applied. In a laminar flow field, when a critical shear rate is reached, polymer coils will get stretched significantly compared to their equilibrium state. This so called coil-stretch transition of the polymer chains results in a significant increase of the elongational viscosity, which has been observed to increase up to ten thousand fold (e.g. Metzner & Metzner (1970), and Landahl (1973)). Replacing the inverse shear rate with the Kolmogorov time scale, the coil-stretch transition was proposed by Lumley (1969) as a mechanism for drag reduction. Figure 1.5 is a sketch from Lumley (1973) and explains how extensional viscosity could cause drag reduction. The graph shows the wave numbers on the horizontal axis and the distance from the wall on the vertical axis, both on a logarithmic scale. Assuming that the size of eddies is limited by their distance from the wall, a line can be drawn which shows an inverse proportionality between the distance from the wall the turbulence wave number. As long as the turbulent wave number is smaller than the wave number corresponding to the viscous cutoff, turbulence can exist. This corresponds to the gray region shaped like a triangle. Close to the wall, where the turbulent wave number is larger than the viscous cutoff, eddies cannot exist because any turbulent kinetic energy at those wave numbers is removed out of the system through viscous dissipation. This results in the viscous sublayer close to the wall. When polymers are added and the time criterion is met, Lumley (1973) argues that the coil-stretch transition causes an increase in the elongational viscosity, which then causes a shift of the viscous cutoff to the left. The thickness of the viscous sublayer increases and drag is reduced.

Another class of theories is those of the elastic viscosity models. As opposed to Lumley's elongational viscosity model which contributes the drag reducing effect of

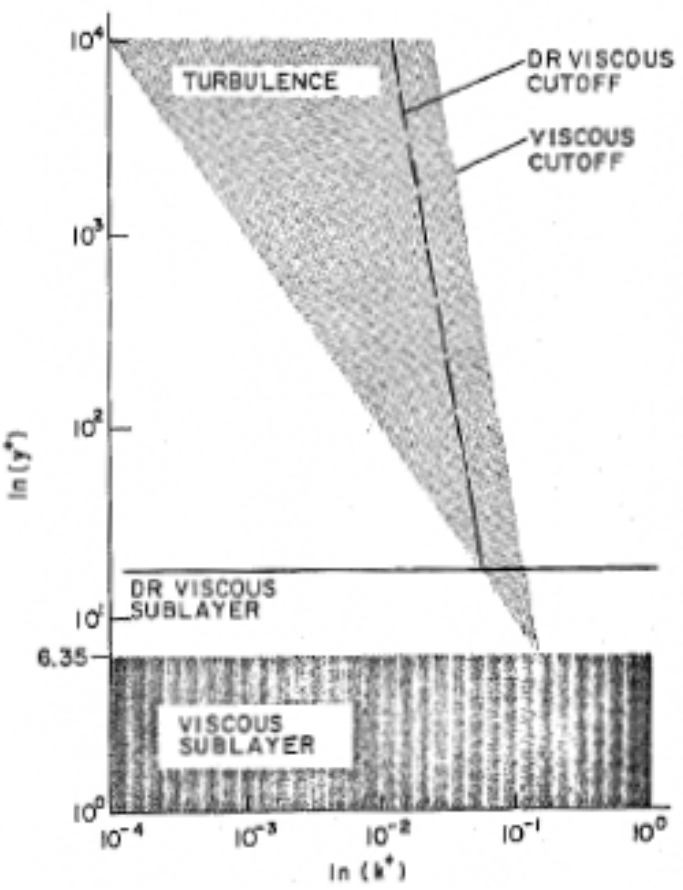

Figure 1.5 – Elongational viscosity thickening the viscous sublayer. A schematic illustrating how by increasing the elongational viscosity drag reducing polymers cause thickening of the viscous sublayer. (Lumley 1973)

polymers to the coil-stretch transition, these models assume it is the elasticity of polymer chains which is responsible for drag reduction. The first one to suggest an elastic model was De Gennes (1986). Based on work by Daoudi & Brochard (1978), later confirmed by Davoudi & Schumacher (2006), De Gennes concluded that the elongational viscosity theory could not be right due to the absence of the coil-stretch transition for polymers undergoing randomly fluctuating stresses in a turbulent velocity field (see also Tabor & De Gennes (1986), De Gennes (1990)). A schematic representation of his theory can be seen in figure 1.6. The graph shows energy as function of length scale. It can be seen how when the time criterion is met for $r = r^*$,

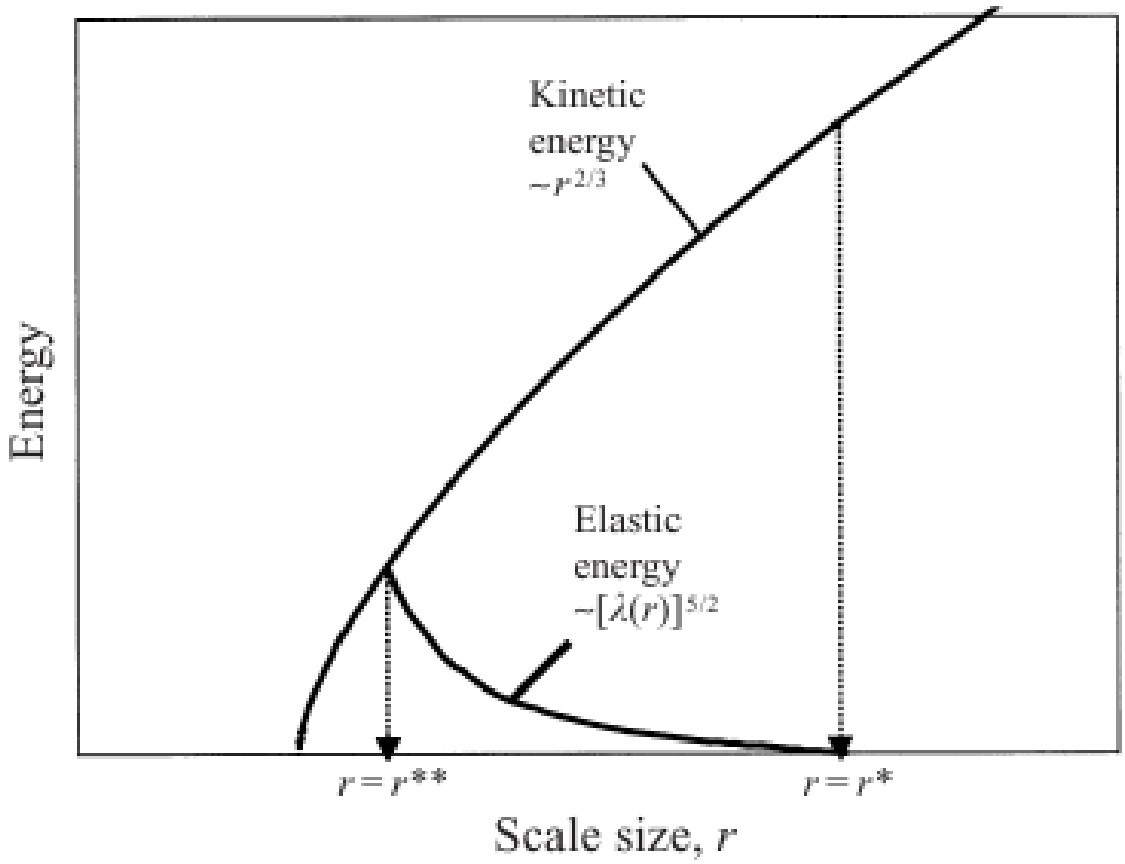

Figure 1.6 – Two onset criteria of elastic viscosity theory. A schematic representation of the two onset criteria defined in elastic viscosity theory. (Sreenivasan & White 2000)

a polymer starts to stretch because of the shear forces from the solvent. The polymer chain is storing elastic energy in its backbone, but as long as this elastic energy is less than the turbulent kinetic energy, a polymer will not be able to alter the turbulent flow field and there will be no drag reduction. However, when $r = r^{**}$ the stresses stored in the polymer's backbone is strong enough that it is able to alter the turbulent flow field and drag reduction is occurring.

Another elastic theory is suggested by Joseph (1990) and Joseph & Christodoulou (1993), who use the Maxwell model and defines the Mach number:

$$M = \frac{u_\tau}{u_c} \tag{1.9}$$

where is u_τ is friction velocity and $u_c = \sqrt{\nu\ \lambda}$ is the wave speed, with λ being the relaxation time. He predicts that for $M > 1$ a non-Newtonian liquid will start showing viscoelastic behavior. A cut-off frequency is predicted damping the smallest eddies and thus resulting in drag reduction. The existence of this cut-off frequency is confirmed by Min et al. (2003).

There are a couple of issues with both Lumley's and de Gennes' models. Both Lumley's model, because it uses the time criterion, and de Gennes' model, because it is based on the fact the polymers have elastic properties, do not predict drag reduction for fibers. However, as is show by Gillissen (2008), fibers do have a drag reducing effect on turbulent flow. Also, both models are very specific in sense that they only focus on drag reduction due to polymer additives, while for example riblets (Choi et al. 1993), and active boundary conditions (Choi et al. 1994) show drag reduction too. Both models assume that polymers change the energy cascade as it is found in isotropic homogeneous turbulence, while wall bounded turbulent flow is very strongly anisotropic. Last but not least, neither model gives a satisfying explanation for the Maximum Drag Reduction asymptote and why it is independent of properties like concentration, chemical structure of the polymer, and molecular weight.

1.7 Empirical modeling

An alternative approach to describe drag reduction is to use an empirical model. The basis for this kind of model is a plot of the streamwise velocity as function of the distance from the wall, a graph of which is show in figure 1.1. As was first noted by Virk (1975), there is a large amount of data which shows that when drag reduction is occurring, close to the wall there is a growing deviation from the Prandtl - Kármán velocity profile for Newtonian liquids, but that, unless the Maximum Drag Reduction

asymptote is reached, eventually the velocity profile falls back to the Newtonian plug and runs parallel with the Newtonian velocity profile. The velocity difference between the Prandtl - Kármán velocity profile and the drag reduced velocity profile is called the effective slip, and this class of models focuses on predicting the magnitude of the effective slip (Ryskin 1987) or finding the distance from the wall at which the fall-back to the Newtonian plug occurs, based on macromolecular properties of the polymer (Benzi et al. 2004).

The most recent incarnation of this kind of model is from Benzi et al. (2004). His model is based on simulations by De Angelis et al. (2004) who showed that, when using a viscosity which increases linearly with the distance away from the wall, a turbulent flow can be simulated with the same characteristics as a drag reduced flow. It is therefore assumed that for polymers to be able to create drag reduction, they need to generate this same linear increase of the effective viscosity. The return to the Newtonian plug occurs when the drag reducing agent cannot sustain the linear increase of viscosity anymore. Benzi et al. (2004, 2006) use this point of return to the Newtonian plug measured as distance from the wall in wall units, as scaling parameter to predict drag reduction and link it to polymer concentration, a chain length, and a hydrodynamic radius. Procaccia et al. (2008) later shows a theoretical derivation of the MDR asymptote and also comes to the conclusion that for a model to be able to describe drag reduction, it should indeed include an effective viscosity which increases linearly with the distance from the wall.

There are however a couple of issues with MDR theory which makes it unlikely that it completely describes drag reduction. First of all the results found by Benzi et al. (2004, 2006) are not consistent with the experimental concentration correlation found by Virk (1975), which is shown in section 1.3. Furthermore, as is derived in appendix C, there are some scaling issues with the equations derived by L'vov et al. (2004) and the behavior in the limit of small polymer relaxation times is not correct.

Last but not least, the theory implies that fibers would not have a drag reducing effect, which they do.

1.8 Streaks

While all the above models focus on drag reduction due to polymer additives, drag reduction is a more general phenomenon. Other ways to get drag reduction in wall bounded flows is by either modifying the wall (Karniadakis & Choi 2003), using for example riblets (Walsh 1982) or active boundary conditions (Choi et al. 1994), or by adding drag reducing agents like surfactants, fibers, and micro bubbles (Bushnell & McGinley 1989). Central in the physics behind all these occurrences of drag reduction are so called streaks, elongated regions with alternating high and low velocities close to the wall. Kline et al. (1967) find that in wall bounded flows, turbulence is generated by bursting events, lift-up, oscillation and break-up of streaks. Corino & Brodkey (1969) identify sweeps, the inrush of high speed fluid towards the wall, breaking up streaks, as the mayor contribution to turbulence generation. Any additive or modification to the wall, that stabilizes streaks and thus prevents these sweeps and ejections will result in drag reduction.

An essential tool in getting more insight in the structure of turbulence has been Direct Numerical Simulation. By completely solving the Navier-Stokes equations a very detailed view can be obtained of all the physics going on, and one has access to variables that are out of reach of traditional experiments. Also, there is the possibility of performing numerical experiments which are not possible in the real world, but which can give a lot of insight. Choi et al. (1993) studied drag reduction through riblets and found that when in drag reducing configuration, they inhibit both velocity and vorticity fluctuations at the wall. (Choi et al. 1994) used active boundary conditions to try to minimize sweeps and injections. By blowing or suction with a velocity equal to the fluid velocity at a distance $y_d^+ \approx 10$ from the wall, they obtained

a maximum drag reduction of up to 30%. De Angelis et al. (2004) simulated a drag reduced flow by imposing a linear increasing viscosity profile proportional to the distance from the wall. Gathered statistics, like stresses and velocity profiles, show a strong resemblance with the statistics found in the case of drag reduction by polymer additives.

To get more insight into the details of polymer-streak interaction two different approaches have been used. One can either consider both the solvent phase and the polymer phase to be continuous, or, because of the difference in time and length scales between solvent and polymer molecules, describe the solvent as a continuous phase and the polymers as a dispersed phase. In the case of the fully continuous description, the polymers phase is described by adding additional terms to the stress tensor using the Oldroyd-B or FENE-P model (Bird et al. 1987, Sureshkumar et al. 1997, Zhou & Akhavan 2003). For simulations which treat the polymers as a dispersed phase, Langevin or Brownian dynamics are used (e.g. Doi & Edwards (1986), Stone & Graham (2003), Terrapon et al. (2004), and Davoudi & Schumacher (2006)). As is mentioned by Peters & Schumacher (2007), there are a couple of issues with the continuum-continuum approach. The FENE-P model suffers from numerical problems (Vaithianathan & Collins 2003), failure of energy stability (Doering et al. 2006), and wrong limiting behavior of non-Newtonian liquids for very high and low frequencies (Temmen et al. 2000). Also, as shown by Dubief et al. (2005), using a continuum approach gives lack of resolution in the low drag reduction regime. Despite the above issues, using the FENE-P model it has been shown that polymers also have a streak stabilizing effect (Dubief et al. 2004). However, apart from the fact that there is consensus that polymers both orientate themselves in the streamwise direction and stretch at the wall, how polymers are able to stabilize streaks is still completely up for debate. Most of the debate focusses on a variation of the old elongational versus elastic viscosity argument. Do polymers stabilize streaks because they are

elongated and locally increase the viscosity (Terrapon et al. 2004), or because they redistribute turbulent kinetic energy by storing it temporally as elastic energy in their backbone (Stone & Graham 2003)? An exception is work by Kim et al. (2008), who observe that counter-torque exerted by polymers suppresses the breakdown of low speed streaks into hairpin vortices. Another question that has been addressed using FENE-P models is how polymers modify the turbulence regeneration cycle. Since about 80% of turbulence is produced in sweeps and ejections Lu & Willmarth (1973), the only way polymers can be so effective as drag reducing agents, is by strongly suppressing these events. However, also here there is no agreements on how this is achieved. For example, Dubief et al. (2004) suggest a model that is a variation on the autonomous regeneration cycle of near wall turbulence by (Jiménez & Pinelli 1999), while Ptasinski et al. (2003) use the shear sheltering model by Hunt & Durbin (1999) as the basis for their model.

The continuum-dispersed phase approach, on the other hand, has so far not even been successful in reproducing drag reduction itself. Apart from Peters & Schumacher (2007), who studied drag reduction in shear flow, all these simulations were one-way coupling, only taking into consideration the forces of the solvent acting on the polymer, and not the forces of the polymer chain acting back on the solvent. Therefore it was not possible to observe drag reduction. Dubief et al. (2005) mentions trying to implement two-way coupling but not being able to simulate with enough polymer chains. Also, because of limited computational resources, all the hybrid DNS Brownian dynamics simulations have been at relatively low Reynolds number. The code written for this research project has two-way coupling implemented and runs on a relatively high Reynolds number. For the first time drag reduction is observed in pressure driven flow using Direct Numerical Simulation and Langevin Dynamics.

CHAPTER 2

RESEARCH QUESTIONS

The above overview of experimental data, simulations, and the different theories that have been developed to explain drag reduction, shows that there are still quite some gaps in our understanding of the phenomenon. However, since the essential characteristic of a polymer molecule is the fact that it has a relaxation time associated with it, this work focuses on the effect of elasticity on drag reduction. More specifically, the following three questions are addressed:

- Is is possible to observe drag reduction using only first principles i.e. using an hybrid Direct Numerical Simulation and Langevin dynamics approach?
- Can drag reduction due to polymer additives be placed in the broader context of other occurrence of the drag reduction phenomenon in the sense that it also acts by reducing sweep and ejection events by streak stabilization?
- Can more insight be gained in what physics is responsible for the drag reducing effect of polymers by looking at the effect of varying their elasticity and thus the relaxation time?

CHAPTER 3

MODELING

In designing our system to study drag reduction a couple of choices had to be made. The first question was whether to study polymers in isotropic turbulence or in wall bounded flow, a discussion which goes back to De Gennes (1986) and Lumley (1973). Because of scaling arguments (Virk 1975), the notion that drag is caused by the flux of momentum from the bulk to the wall (Procaccia et al. 2008), and the fact that drag reduction in general is considered a wall phenomenon (Choi et al. 1994), it was decided that the largest chance of capturing the essential physics for drag reduction would be with a wall bounded flow. Because there was access to the code of Eggels (1994), it was decided to study the polymers in pipe flow. Also, a Reynolds number had to be chosen. Investigating the literature on hybrid Brownian motion and DNS simulations, it was found that typically simulations are performed for fairly low Reynolds numbers of below $\mathrm{Re}_\tau < 300$ (Terrapon et al. 2004, Dubief et al. 2005, Gupta et al. 2004). To make sure that the turbulent flow stays fully turbulent when drag reduction occurs and because it was found that the onset of drag reduction is earlier with higher Reynolds numbers (Sreenivasan & White 2000), it was decided to take a Reynolds number of $\mathrm{Re}_\tau = 560$.

The polymers, because it was suggested that the dominant time scale for drag reduction is their longest relaxation time (Hershey & Zakin 1967, Lumley 1969), are modeled as FENE dumbbells. The longest relaxation time is taken to be the Zimm (1956) relaxation time, and the dumbbell is dimensionalized so that it's relaxation time is at least equal to the characteristic time scale of the solvent, i.e. the Deborah

number is larger than one. Because the typical polymer concentrations (in the order of 1 p.p.m.w.) at which drag reduction is observed is a couple of orders below the critical concentration, polymer-polymer interactions are neglected. Each polymer chain is completely unaware of any other chains in the domain and will not interact with them. Polymers and solvent interact through two-way coupling, where both the solvent acting on the polymers through a drag force, and the polymers reactive force on the solvent are taken into consideration. The interaction of polymers with the wall is through hard-sphere interaction. Also, to keep the number of variables to a minimum, gravity is neglected.

3.1 Solvent

As mentioned above, the solvent is described as a continuum, and thus by using the Navier-Stokes equations for incompressible flow for the conservation of momentum:

$$\rho_1 \left(\frac{\partial \mathbf{u}_1}{\partial t} + \mathbf{u}_1 \cdot \nabla \mathbf{u}_1 \right) = -\nabla p + \mu_1 \nabla^2 \mathbf{u}_1 + \mathbf{f}_B \tag{3.1}$$

and the continuity equation for the conservation of mass:

$$\nabla \cdot \mathbf{u}_1 = 0 \tag{3.2}$$

The subscript 1 is used to indicate that the variables describe the solvent, while the polymer variables presented in the next section have a subscript 2. ρ is the density, $\mathbf{u}$ is the velocity, t is time, p is the pressure, μ_1 is the dynamic viscosity, and $\mathbf{f}_B$ are any body forces acting on the liquid, for example the forces of the polymer chains acting back in the solvent.

Scaled with the wall variables u_τ and ν, the friction velocity and the kinematic viscosity respectively, the momentum balance becomes:

$$\frac{\partial \mathbf{u}_1^+}{\partial t^+} + \mathbf{u}_1^+ \cdot \nabla \mathbf{u}_1^+ = -\nabla p^+ + \nabla^2 \mathbf{u}_1^+ + \mathbf{f}_B^+ \tag{3.3}$$

and the mass balance:

$$\nabla \cdot \mathbf{u}_1^+ = 0 \tag{3.4}$$

By making the Navier-Stokes equation non-dimensional, the first important non-dimensional number can been identified, the friction Reynolds number:

$$\mathrm{Re}_\tau = \frac{d_1 u_\tau}{\nu} \tag{3.5}$$

which, when scaling in wall units, becomes apparent as the non-dimensional diameter of the pipe, d_1, in wall units. There is also another way of looking at the friction Reynolds number. For steady state channel and pipe flow the shear at the wall, τ_w, and the pressure drop over the pipe or channel, $\Delta p/\Delta z$, have to balance each other. This means that the friction velocity for pipe flow can be written as:

$$u_\tau = \left(\frac{\tau_w}{\rho_1}\right)^{1/2} = \left(\frac{d_1}{4\rho_1}\left|\frac{\Delta p}{\Delta z}\right|\right)^{1/2} \tag{3.6}$$

Thus, when in a drag reduction experiment or simulation the friction Reynolds number is kept constant, this means that the pressure head is kept constant (assuming that the pipe diameter, and the density and viscosity of the solvent were not changed).

For a more in depth analysis of the Navier-Stokes equation and of turbulence these books by Tennekes & Lumley (1972), Hinze (1975), and Pope (2000) are recommended literature.

3.2 Polymer

The behavior of the polymer chains is described by the Langevin equation. Because it is the simplest representation of a polymer chain, the equations presented here are for dumbbells, but they can easily be extended to chains consisting of more beads, and thus to chains having more modes than only the Zimm (1956) relaxation time. Naming the two Brownian beads of the dumbbell A and B, each having a friction factor, ζ, and connected to each other by a FENE spring with spring constant, k, the equation of motion for bead A equals:

$$\rho_2 \frac{\pi d_2^3}{6} \ddot{\mathbf{x}}_{2,A} = -\zeta \left(\dot{\mathbf{x}}_{2,A} - \mathbf{u}_{1,A} \right) - k \frac{\mathbf{x}_{2,AB}}{1 - \left(\mathbf{x}_{2,AB} / \mathbf{x}_{2,\mathrm{Max}} \right)^2} + \mathbf{f}_R \left(t \right) \tag{3.7}$$

with:

$$\mathbf{x}_{2,AB} = \mathbf{x}_{2,A} - \mathbf{x}_{2,B} + \mathbf{x}_{2,0} \tag{3.8}$$

Again, the subscript 1 indicates that variables are associated with the continuous phase and the subscript 2 indicates that they are associated with the dispersed polymer phase. ρ_2 is the bead density, d_2 is the bead diameter, $\mathbf{x}_{2,A}$, $\dot{\mathbf{x}}_{2,A}$, and $\ddot{\mathbf{x}}_{2,A}$ are the position, velocity, and acceleration of bead A, $\mathbf{x}_{2,B}$, is the position of bead B, $\mathbf{x}_{2,0}$ is the equilibrium distance between beads A and B, $\mathbf{x}_{2,\mathrm{Max}}$ is the maximum extension of the polymer chain, and $\mathbf{u}_{1,A}$ is the fluid velocity at the position of bead A. The first term on the left hand side is the acceleration of the bead, which unlike in Brownian dynamics, cannot be set to zero, because then there would be no force acting back on the solvent. The first term on the right hand side of the equation of motion of bead A describes the drag force it experiences due to a velocity difference with the solvent, the second term is the FENE spring force caused by a deviation from the equilibrium distance between bead A and B, and the third term is the random force describing solvent molecules hitting the bead. This random force has the properties:

$$\begin{aligned} \langle f_R(t) \rangle &= 0 \\ \langle f_R(t)\, f_R(t') \rangle &= 2\zeta k_B T \delta(t - t') \end{aligned} \tag{3.9}$$

On average the random force is zero, and each hit by a solvent molecule is assumed to be independent from all others. In the above equation, ζ is the friction factor, k_B is the Boltzmann constant, and T is the temperature.

Assuming Stokes drag, which gives a friction factor of $\zeta = 3\pi\rho_1\nu d_2$, and writing the equation of motion also in wall units gives:

$$\tau_2^+ \ddot{\mathbf{x}}_{2,A}^+ = -\left(\dot{\mathbf{x}}_{2,A}^+ - \mathbf{u}_{1,A}^+\right) - \frac{1}{\mathrm{De}} \frac{\mathbf{x}_{2,AB}^+}{1 - \left(\mathbf{x}_{2,AB}^+ / \mathbf{x}_{2,\mathrm{Max}}^+\right)^2} + f_R^+\left(t^+\right) \tag{3.10}$$

with:

$$\mathbf{x}_{2,AB}^+ = \mathbf{x}_{2,A}^+ - \mathbf{x}_{2,B}^+ + \mathbf{x}_{2,0}^+ \tag{3.11}$$

and random force:

$$\begin{aligned} \left\langle f_R^+\left(t^+\right) \right\rangle &= 0 \\ \left\langle f_R^+\left(t^+\right) f_R^+\left(t'^+\right) \right\rangle &= 2\frac{\left(k_B T\right)^+}{\zeta^+} \delta\left(t^+ - t'^+\right) \end{aligned} \tag{3.12}$$

The non-dimensional numbers resulting from making these equations dimensionless are, τ_2^+, the particle relaxation time, De, the Deborah number, and, $\left(k_B T\right)^+ / \zeta^+ = D^+$, a diffusion constant. The particle relaxation time is defined as:

$$\tau_2^+ = \frac{1}{\rho^* d^{*2}} \frac{\mathrm{Re}_\tau^2}{18} \tag{3.13}$$

with $\rho^* = \rho_1/\rho_2$, and $d^* = d_1/d_2$, and is a measure of how sensitive a particle or bead is to velocity fluctuations in the fluid. A large particle relaxation time means that a particle is not affected by fluid velocity fluctuations and moves in a straight

line, while a small particle relaxation time means that a particle exactly moves a long with the streamlines of the fluid it is in. The Deborah number is defined as:

$$\mathrm{De} = \tau_Z^+ = \frac{R_g^{+3}}{(k_B T)^+} \tag{3.14}$$

with R_g^+ the radius of gyration of the polymer chain in wall units, and:

$$(k_B T)^+ = k_B T \frac{u_\tau}{\rho_1 \nu^3} \tag{3.15}$$

The Deborah number is defined as the ratio of the relaxation time over the characteristic time scale of the solvent. Since the characteristic time scale of the fluid in wall units is equal to one, the Deborah number is our case is equal to the Zimm relaxation time in wall units, τ_Z^+. A Deborah number smaller than one means that there is no overlap between the relaxation time spectrum of the polymer and the turbulent time spectrum, while a Deborah number larger than one means there is an overlap in the time spectra.

Instead of the Deborah number, also the Weissenberg number is used in the literature. However, since the Weissenberg number indicates the degree of anisotropy or orientation generated by the deformation, and is appropriate to describe flows with a constant stretch history, such as simple shear, it is not applicable to polymers in turbulence (Bird & Hassager 1987).

The last dimensionless group, the diffusion constant of the bead in wall units, equals:

$$D^+ = \frac{(k_B T)^+}{\zeta^+} = \frac{(k_B T)^+}{3\pi \mathrm{Re}_\tau} d^* \tag{3.16}$$

When this number is large the bead behaves like a Brownian particle because the diffusion of the bead is larger than the advection. However, when it is small, advection is dominant i.e. Brownian motion is negligible compared to the displacement of the

bead due to drag forces. This makes the diffusion coefficient in wall units an inverse Peclet number. The next step is to calculate the above non-dimensional numbers from known properties, which is done in the next section.

3.3 Parameters

After the derivation of the equations and non dimensional numbers describing the polymer solution in the previous two sections, in this section the actual values assigned to these numbers are presented. In our model system water is taken as the solvent and PEG for the polymer. In table 3.1 an overview is given of all the known parameters.

The first number on the list is the friction Reynolds number. To be sure the flow stays fully turbulent when drag reduction occurs, and because drag reduction sets in earlier for higher Reynolds numbers, the friction Reynolds number is chosen to be $\mathrm{Re}_\tau = 560$. This corresponds to a bulk Reynolds number of $\mathrm{Re} = 8800$. The pressure head and thus the friction Reynolds number is kept constant when drag reduction is occurring throughout different runs while the bulk Reynolds number is allowed to vary.

The second parameter on the list is the Deborah number De. Because elasticity is considered a very important polymer property (White & Mungal 2008) in their effectiveness as drag reducing agents, simulations were run for 3 different values: $\mathrm{De} = 1$ because it defines the onset of drag reduction, $\mathrm{De} = 10$ to have a value well within the drag reduction regime, and $\mathrm{De} = 0$ (i.e. rods) as control value.

To keep the number of polymer chains which have to be simulated as small as possible, the diameter of the pipe is chosen to be of the order of the smallest pipes found in experiments. This is of the order of $1 \cdot 10^{-4}$ m (Virk 1975). Warholic et al. (1999) found drag reduction occurring with polymer concentrations as low as in the order of 0.1 p.p.m.w., which is of the same order as the concentration used in our

Description	Symbol	Value	Units
Friction Reynolds number	Re_τ	560	
Deborah number	De	0	
		1	
		10	
Pipe diameter	d_1	$1{\cdot}10^{-4}$	m
Polymer concentration	c	0.46	p.p.m.w.
Solvent density	ρ_1	$1{\cdot}10^{3}$	kg m^{-3}
Kinematic viscosity	ν	$1{\cdot}10^{-6}$	m^2 s^{-1}
Thermal energy	k_BT	$4.14{\cdot}10^{-21}$	J
Kuhn length	a	$1{\cdot}10^{-10}$	m
Kuhn length mass	M_a	500	u
Avogadro's number	N_A	$6.02{\cdot}10^{23}$	mol^{-1}
u to kg conversion constant	u	$1.66{\cdot}10^{-27}$	kg u^{-1}

Table 3.1 – An overview of all known properties and their (chosen) values.

simulations. For the solvent water is chosen, with a density of 1000 kg m^{-3}, and a kinematic viscosity of 10^{-6} m^2 s^{-1} at room temperature. The thermal energy, k_BT, is set to be $4.142 \cdot 10^{-21}$ J. The last two parameters are properties of the polymer, the Kuhn length, a, and the mass per Kuhn length, M_a. In the case of PEG, typical values for these parameters are $a = 1 \cdot 10^{-9}$ m and $M_a = 500$ u.

In the mapping of the polymer molecule to a dumbbell, the following properties are preserved: i) The diffusion coefficient of the bead spring model is matched to the diffusion as calculated by the Zimm model (Öttinger 1989). ii) The Deborah number matches the Zimm relaxation time in wall units. iii) The mass of the bead spring model needs to be the same of weight one molecule. Using these requirements, the particle relaxation time and the diffusion constant can be determined, which are show in table 3.2. The equilibrium length between two beads $x^+_{2,0}$ is the equal to the Radius of gyration in wall units, R^+_g. With changing Deborah numbers the molecular weight of the dumbbells has been kept constant, which results in the shown values for the maximum extension of the springs. More details of the calculations of the different parameters can be found in appendix B.

Description	**Symbol**	**Value**
Density ratio	ρ^*	$2.84{\cdot}10^{-4}$
Diameter ratio	d^*	$1.85{\cdot}10^{5}$
Particle relaxation time	τ_2^+	$1.79{\cdot}10^{-3}$
Diffusion constant	D^+	$8.13{\cdot}10^{-4}$
Number of chains	N_2	$9.60{\cdot}10^{5}$
Equilibrium length	$\mathbf{x}_{2,0}^+$	$4.00{\cdot}10^{-1}$
		$2.84{\cdot}10^{-2}$
		$6.11{\cdot}10^{-2}$
Maximum extension	$\mathbf{x}_{2,\mathrm{Max}}^+$	$1.00{\cdot}\mathbf{x}_{2,0}^+$
		$1.41{\cdot}\mathbf{x}_{2,0}^+$
		$6.55{\cdot}\mathbf{x}_{2,0}^+$

Table 3.2 – An overview of all derived properties and their values. An overview of all properties calculated from table 3.1.

CHAPTER 4

COMPUTATIONAL

4.1 Why parallel programming?

The code is a modified version of the code used by Boelens & Portela (2007), which was originally written by Eggels (1994). The modifications are the implementation of Brownian Motion of the particles, the possibility to connect two or more particles with springs, to simulate polymers, and the fact that the code was parallelized. This section deals with the modifications that were made to the code to get it to run in parallel and the modifications made to the particle tracking code to simulate polymer chains. This includes modifications to the predictor and the Poisson solver, parallel particle tracking, and keeping track of the positions of the different beads in a polymer chain.

However, the first question to ask is: why would one want to run a computer program in parallel at all? Depending on the problem at hand there are two reasons: processor time and memory requirements. A calculation could be very demanding processing-time wise, and by parallelizing a code the work load gets distributed across multiple processors. Alternatively, a calculation could be very demanding memory wise and again, by parallelizing a code, the work load is distributed. In the case of fluid-mechanics problems both processing-speed requirements and memory consumption are generally very high to be able to accurately resolve all time and length scales present.

Parallelization does not come without its owns costs, though. One could assume that by just adding more and more processors to a problem, one could solve anything,

but this turns out not to be true. The problem is that it is hardly ever possible to split a problem up in completely independent sub-problems. Different processes almost always need information from other processes, and when dividing up a problem among too many processors the communication costs of exchanging this information will dominate over the speed-up gained by parallelizing the code. In the end parallelizing a code is always about finding the optimum between communication costs, memory consumption and processing speed.

4.2 (Sub)domains

Although drag reduction scales in wall units, the simulation itself is performed in bulk units, because this give a well scaled domain size which is independent of the Reynolds number. The whole computational domain is a cylinder with diameter $d_1^* = 1$ and length $l^* = 5d_1^*$. Because close to the wall the length scales that need to be resolved are smaller, the grid is non-homogeneous with grid function:

$$r_i = \frac{1}{2} \frac{\tanh\left(C_{\text{grid}} \frac{i}{i_{\max}}\right)}{\tanh\left(C_{\text{grid}}\right)} \tag{4.1}$$

The parameter C_{grid} determines the non-homogeneity of the grid and is set to 2.45 in the simulations presented here. Because of tanh, this grid function has the nice properties that it is continuous for values of i smaller than zero and larger than $i_{\max}$, so that it can also be used to define cells outside the domain. The whole domain is split up in $i_{\max} \times j_{\max} \times k_{\max}$ grid cells.

Because of the cylindrical geometry of this problem, it was decided to give the different sub-domains the shape of pie slices. While also splitting up the domain in the radial direction would have resulted in sub-domains with different boundary conditions in the center and at the wall, by taking pie slices, all sub-domains are the same. This makes it easier to program because there are no sub-domains which

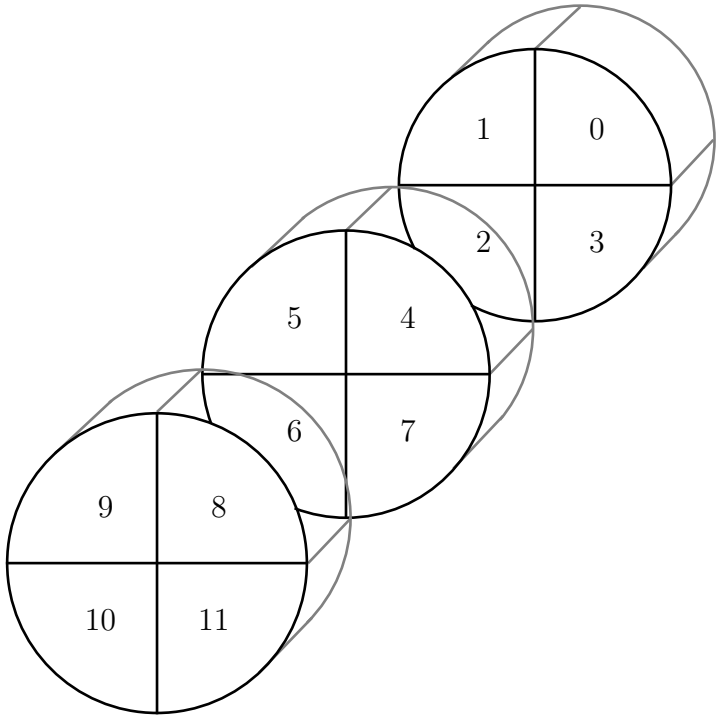

Figure 4.1 – Computational domain split up in pie slices. For the domain being split up 4 times in the angular direction and 3 times in the streamwise direction, this is what the counting of the different sub-domains would look like.

need special treatment because they are different from the rest. For communication between the different processors, each processor has its own unique identification number as show in figure 4.1. There are N_{proc} processors in total with N_z disks and N_ϕ processors per disk so that, $N_\phi \cdot N_z = N_{\text{proc}}$. The first processor with number zero is at position $\phi = 0$ and $z = 0$ and then the processor id numbers increase with increasing angle, ϕ. After the first disk is filled, the numbering continues on the second disk and so on till the complete domain is filled. Each sub-domain contains the same grid of size $ii_{\max} \times jj_{\max} \times kk_{\max}$. The values of $ii_{\max}$, $jj_{\max}$, and $kk_{\max}$ are defined as:

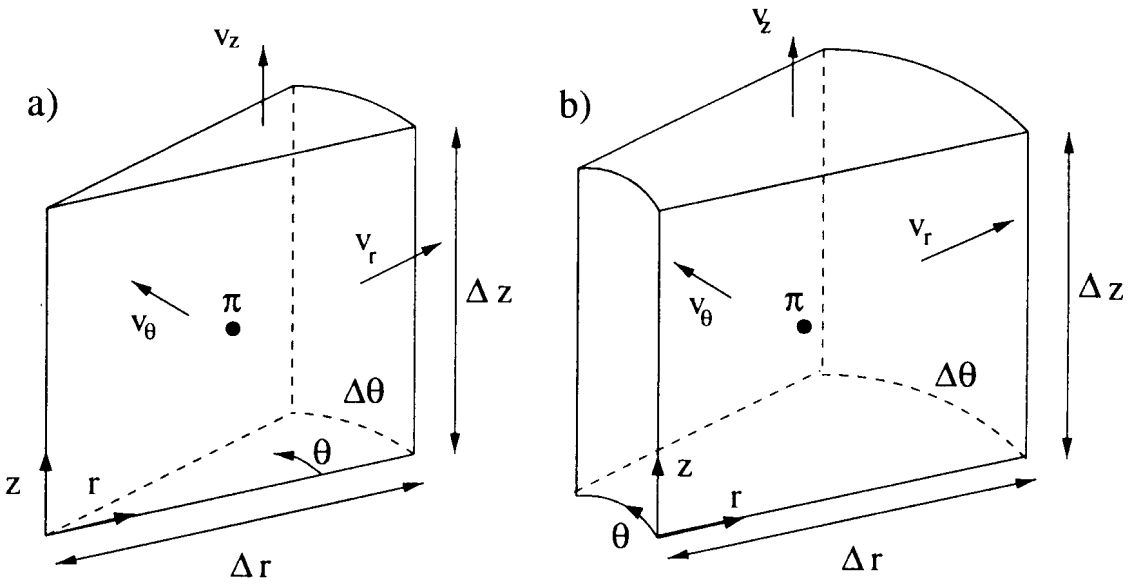

Figure 4.2 – Staggered grid cells on which the continuous phase is solved.

$$\begin{aligned} ii_{\max} &= \frac{i_{\max}}{N_r} \\ jj_{\max} &= \frac{j_{\max}}{N_\phi} \\ kk_{\max} &= \frac{k_{\max}}{N_z} \end{aligned} \tag{4.2}$$

The layout of the individual cells is show in figure 4.2. For grid cell i, j, k the pressure $p_{i,j,k}$ is defined in the center of the cell, while the velocities, $u_{i,j,k}$, $v_{i,j,k}$, and $w_{i,j,k}$, are defined on the different walls of each grid cell. The radial position of the radial velocity, $u_{i,j,k}$, is referred to as $r_{u,i}$, while the radial position of the angular velocity $v_{i,j,k}$, the streamwise velocity, $w_{i,j,k}$, and the pressure, $p_{i,j,k}$ is referred to as $r_{p,i}$. The angular position the angular velocity is called $\phi_{v,j}$. and the angular position of radial velocity $u_{i,j,k}$, the streamwise velocity, $w_{i,j,k}$, and the pressure, $p_{i,j,k}$ is $\phi_{p,j}$, The streamwise position of the streamwise velocity, $w_{i,j,k}$, is called $z_{w,k}$, while the streamwise position of the radial velocity, $u_{i,j,k}$, angular velocity, $v_{i,j,k}$, and the pressure, $p_{i,j,k}$, is $z_{p,k}$.

4.3 Advection & Diffusion

The "Advec" and "Diffus" subroutines calculate the advective and diffusive terms of the Navier-Stokes Equations. This is done in cylindrical coordinates, using a finite volume scheme. The advective term in cylindrical coordinates looks like:

$$- \left(\underbrace{\frac{1}{r}\frac{\partial}{\partial r}\left(ruu\right)}_{\mathrm{rUU}} + \underbrace{\frac{1}{r}\frac{\partial}{\partial \phi}\left(uv\right)}_{\mathrm{UV}} + \underbrace{\frac{\partial}{\partial z}\left(uw\right)}_{\mathrm{UW}} - \underbrace{\frac{vv}{r}}_{\mathrm{VV}} \right) \tag{4.3}$$

$$- \left(\underbrace{\frac{1}{r}\frac{\partial}{\partial r}\left(rvu\right)}_{\mathrm{rVU}} + \underbrace{\frac{1}{r}\frac{\partial}{\partial \phi}\left(vv\right)}_{\mathrm{VV}} + \underbrace{\frac{\partial}{\partial z}\left(vw\right)}_{\mathrm{VW}} + \underbrace{\frac{vu}{r}}_{\mathrm{VU}} \right) \tag{4.4}$$

$$- \left(\underbrace{\frac{1}{r}\frac{\partial}{\partial r}\left(rwu\right)}_{\mathrm{rWU}} + \underbrace{\frac{1}{r}\frac{\partial}{\partial \phi}\left(wv\right)}_{\mathrm{WV}} + \underbrace{\frac{\partial}{\partial z}\left(ww\right)}_{\mathrm{WW}} \right) \tag{4.5}$$

and the diffusive term looks like:

$$\underbrace{\frac{1}{r}\frac{\partial}{\partial r}\left(r\sigma_{r,r}\right)}_{\mathrm{r\Sigma rr}} + \underbrace{\frac{1}{r}\frac{\partial}{\partial \phi}\left(\sigma_{r,\phi}\right)}_{\mathrm{\Sigma r\phi}} + \underbrace{\frac{\partial}{\partial z}\left(\sigma_{r,z}\right)}_{\mathrm{\Sigma rz}} - \underbrace{\frac{\sigma_{\phi,\phi}}{r}}_{\mathrm{\Sigma\phi\phi}} \tag{4.6}$$

$$\underbrace{\frac{1}{r}\frac{\partial}{\partial r}\left(r\sigma_{\phi,r}\right)}_{\mathrm{r\Sigma\phi r}} + \underbrace{\frac{1}{r}\frac{\partial}{\partial \phi}\left(\sigma_{\phi,\phi}\right)}_{\mathrm{\Sigma\phi\phi}} + \underbrace{\frac{\partial}{\partial z}\left(\sigma_{\phi,z}\right)}_{\mathrm{\Sigma\phi r}} + \underbrace{\frac{\sigma_{\phi,r}}{r}}_{\mathrm{\Sigma\phi r}} \tag{4.7}$$

$$\underbrace{\frac{1}{r}\frac{\partial}{\partial r}\left(r\sigma_{z,r}\right)}_{\mathrm{r\Sigma zr}} + \underbrace{\frac{1}{r}\frac{\partial}{\partial \phi}\left(\sigma_{z,\phi}\right)}_{\mathrm{\Sigma z\phi}} + \underbrace{\frac{\partial}{\partial z}\left(\sigma_{z,z}\right)}_{\mathrm{\Sigma zz}} \tag{4.8}$$

with:

$$\sigma = \frac{2}{\mathrm{Re}_\tau} \begin{pmatrix} \frac{\partial u}{\partial r} & \frac{1}{2}\left(r\frac{\partial}{\partial r}\left(\frac{v}{r}\right) + \frac{1}{r}\frac{\partial u}{\partial \phi}\right) & \frac{1}{2}\left(\frac{\partial w}{\partial r} + \frac{\partial u}{\partial z}\right) \\ \frac{1}{2}\left(r\frac{\partial}{\partial r}\left(\frac{v}{r}\right) + \frac{1}{r}\frac{\partial u}{\partial \phi}\right) & \frac{1}{r}\frac{\partial v}{\partial \phi} + \frac{u}{r} & \frac{1}{2}\left(\frac{\partial v}{\partial z} + \frac{1}{r}\frac{\partial w}{\partial \phi}\right) \\ \frac{1}{2}\left(\frac{\partial w}{\partial r} + \frac{\partial u}{\partial z}\right) & \frac{1}{2}\left(\frac{\partial v}{\partial z} + \frac{1}{r}\frac{\partial w}{\partial \phi}\right) & \frac{\partial w}{\partial z} \end{pmatrix} \tag{4.9}$$

To turn these terms into a finite volume scheme, they need to be volume averaged. For this purpose, a volume is defined for each velocity component, centered around

their origin: ΔV_u for u, ΔV_v for v, and ΔV_w for w. The integrals over these finite volumes are defined as:

$$\Delta V_u = \int_{z_{w,k-1}}^{z_{w,k}} \int_{\phi_{v,j-1}}^{\phi_{v,j}} \int_{r_{p,i}}^{r_{p,i+1}} r \; dr \; d\phi \; dz \tag{4.10}$$

$$\Delta V_v = \int_{z_{w,k-1}}^{z_{w,k}} \int_{\phi_{p,j}}^{\phi_{p,j+1}} \int_{r_{u,i-1}}^{r_{u,i}} r \; dr \; d\phi \; dz \tag{4.11}$$

$$\Delta V_w = \int_{z_{p,k}}^{z_{p,k+1}} \int_{\phi_{v,j-1}}^{\phi_{v,j}} \int_{r_{u,i-1}}^{r_{u,i}} r \; dr \; d\phi \; dz \tag{4.12}$$

Which gives for the actual volumes:

$$\Delta V_u = r_{u,i} \Delta r_{u,i} \Delta\phi \Delta z \tag{4.13}$$

$$\Delta V_v = r_{p,i} \Delta r_{p,i} \Delta\phi \Delta z \tag{4.14}$$

$$\Delta V_w = r_{p,i} \Delta r_{p,i} \Delta\phi \Delta z \tag{4.15}$$

Now lets take, as an example, the first term of the radial component of the advective term of the Navier-Stokes equation, rUU. When performing the volume integral over this term, it can be seen that the term, ruu, which is differentiated with respect to r, is recovered, with integration limits $r_{p,i}$ and $r_{p,i+1}$. When also performing the integrals over ϕ and z and writing out the integration limits, uu becomes the surface averaged term $\overline{uu}$ over the surface $\Delta\phi\Delta z$ at the radial positions $r_{p,i}$ and $r_{p,i+1}$:

$$\overline{\overline{\mathrm{rUU}}} = \frac{1}{\Delta V_u} \int_{z_{w,k-1}}^{z_{w,k}} \int_{\phi_{v,j-1}}^{\phi_{v,j}} \left[ruu \right]_{r_{p,i}}^{r_{p,i+1}} d\phi \; dz \tag{4.16}$$

$$= \frac{1}{\Delta V_u} \left[r\overline{uu} \right]_{r_{p,i}}^{r_{p,i+1}} \Delta\phi \; \Delta z \tag{4.17}$$

$$= \frac{1}{\Delta V_u} \left[r_{p,i+1} \; \overline{uu}\Big|_{r_{p,i+1}} - r_{p,i} \; \overline{uu}\Big|_{r_{p,i}} \right] \Delta\phi \; \Delta z \tag{4.18}$$

This procedure can be repeated for all the different parts of the advective term and, when also writing out the volume terms, this gives the following expressions for the

radial component:

$$\overline{\overline{\mathrm{rUU}}} = \frac{1}{r_{u,i}\Delta r_{u,i}}\left[r_{p,i+1}\,\overline{uu}\Big|_{r_{p,i+1}} - r_{p,i}\,\overline{uu}\Big|_{r_{p,i}}\right] \tag{4.19}$$

$$\overline{\overline{\mathrm{UV}}} = \frac{1}{r_{u,i}\Delta\phi}\left[\overline{uv}\Big|_{\phi_{v,j}} - \overline{uv}\Big|_{\phi_{v,j-1}}\right] \tag{4.20}$$

$$\overline{\overline{\mathrm{UW}}} = \frac{1}{\Delta z}\left[\overline{uw}\Big|_{z_{w,k}} - \overline{uw}\Big|_{z_{w,k-1}}\right] \tag{4.21}$$

$$\overline{\overline{\mathrm{VV}}} = \frac{1}{r_{u,i}}\left[\overline{\overline{vv}}\right] \tag{4.22}$$

The angular component becomes:

$$\overline{\overline{\mathrm{rVU}}} = \frac{1}{r_{p,i}\Delta r_{p,i}}\left[r_{u,i}\,\overline{vu}\Big|_{r_{u,i}} - r_{u,i-1}\,\overline{vu}\Big|_{r_{u,i-1}}\right] \tag{4.23}$$

$$\overline{\overline{\mathrm{VV}}} = \frac{1}{r_{p,i}\Delta\phi}\left[\overline{vv}\Big|_{\phi_{p,j+1}} - \overline{vv}\Big|_{\phi_{p,j}}\right] \tag{4.24}$$

$$\overline{\overline{\mathrm{VW}}} = \frac{1}{\Delta z}\left[\overline{vw}\Big|_{z_{w,k}} - \overline{vw}\Big|_{z_{w,k-1}}\right] \tag{4.25}$$

$$\overline{\overline{\mathrm{VU}}} = \frac{1}{r_{p,i}}\left[\overline{\overline{vu}}\right] \tag{4.26}$$

and the streamwise component looks like:

$$\overline{\overline{\mathrm{rWU}}} = \frac{1}{r_{p,i}\Delta r_{p,i}}\left[r_{u,i}\,\overline{wu}\Big|_{r_{u,i}} - r_{u,i-1}\,\overline{wu}\Big|_{r_{u,i-1}}\right] \tag{4.27}$$

$$\overline{\overline{\mathrm{WV}}} = \frac{1}{r_{p,i}\Delta\phi}\left[\left(\overline{wv}\Big|_{\phi_{v,j}} - \overline{wv}\Big|_{\phi_{v,j-1}}\right)\right] \tag{4.28}$$

$$\overline{\overline{\mathrm{WW}}} = \frac{1}{\Delta z}\left[\left(\overline{ww}\Big|_{z_{p,k+1}} - \overline{ww}\Big|_{z_{p,k}}\right)\right] \tag{4.29}$$

All volume integrals, except the source terms $\overline{\overline{\mathrm{VV}}}$ and $\overline{\overline{\mathrm{VU}}}$, have been turned into surface integrals, which will be dicretesized with a 4th order scheme.

For the diffusive terms the same procedure is followed. This gives for the radial component:

$$\overline{\overline{\mathrm{r}\Sigma\mathrm{rr}}} = \frac{2}{r_{u,i}\Delta r_{u,i}}\left[r_{p,i+1}\left.\frac{\partial\overline{u}}{\partial r}\right|_{r_{p,i+1}} - r_{p,i}\left.\frac{\partial\overline{u}}{\partial r}\right|_{r_{p,i}}\right] \tag{4.30}$$

$$\begin{aligned}\overline{\overline{\Sigma\mathrm{r}\phi}} &= \frac{1}{r_{u,i}\Delta\phi}\left[\left.\frac{\partial\overline{v}}{\partial r}\right|_{\phi_{v,j}} - \left.\frac{\partial\overline{v}}{\partial r}\right|_{\phi_{v,j-1}}\right] \\ &+ \frac{1}{r_{u,i}^2\Delta\phi}\left[\left.\frac{\partial\overline{u}}{\partial\phi}\right|_{\phi_{v,j}} - \left.\frac{\partial\overline{u}}{\partial\phi}\right|_{\phi_{v,j-1}} - \left.\overline{v}\right|_{\phi_{v,j}} + \left.\overline{v}\right|_{\phi_{v,j-1}}\right]\end{aligned} \tag{4.31}$$

$$\overline{\overline{\Sigma\mathrm{rz}}} = \frac{1}{\Delta z}\left[\left.\frac{\partial\overline{w}}{\partial r}\right|_{z_{w,k}} - \left.\frac{\partial\overline{w}}{\partial r}\right|_{z_{w,k-1}} + \left.\frac{\partial\overline{u}}{\partial z}\right|_{z_{w,k}} - \left.\frac{\partial\overline{u}}{\partial z}\right|_{z_{w,k-1}}\right] \tag{4.32}$$

$$\overline{\overline{\Sigma\phi\phi}} = \frac{2}{r_{u.i}^2\Delta\phi}\left[\left.\overline{v}\right|_{\phi_{v,j}} - \left.\overline{v}\right|_{\phi_{v,j-1}} + \overline{\overline{u}}\Delta\phi\right] \tag{4.33}$$

For the angular component:

$$\begin{aligned}\overline{\overline{\mathrm{r}\Sigma\phi\mathrm{r}}} &= \frac{1}{r_{p,i}\Delta r_{p,i}}\left[r_{u,i}\left.\frac{\partial\overline{v}}{\partial r}\right|_{r_{u,i}} - r_{u,i-1}\left.\frac{\partial\overline{v}}{\partial r}\right|_{r_{u,i-1}}\right] \\ &+ \frac{1}{r_{p,i}\Delta r_{p,i}}\left[\left.\frac{\partial\overline{u}}{\partial\phi}\right|_{r_{u,i}} - \left.\frac{\partial\overline{u}}{\partial\phi}\right|_{r_{u,i-1}} - \left.\overline{v}\right|_{r_{u,i}} + \left.\overline{v}\right|_{r_{u,i-1}}\right]\end{aligned} \tag{4.34}$$

$$\overline{\overline{\Sigma\phi\phi}} = \frac{2}{r_{p,i}^2\Delta\phi}\left[\left.\frac{\partial\overline{v}}{\partial\phi}\right|_{\phi_{p,j+1}} - \left.\frac{\partial\overline{v}}{\partial\phi}\right|_{\phi_{p,j}} + \left.\overline{u}\right|_{\phi_{p,j+1}} - \left.\overline{u}\right|_{\phi_{p,j}}\right] \tag{4.35}$$

$$\overline{\overline{\Sigma\phi\mathrm{r}}} = \frac{1}{\Delta z}\left[\left.\frac{\partial\overline{v}}{\partial z}\right|_{z_{w,k}} - \left.\frac{\partial\overline{v}}{\partial z}\right|_{z_{w,k-1}} + \frac{1}{r_{p,i}}\left[\left.\frac{\partial\overline{w}}{\partial\phi}\right|_{z_{w,k}} - \left.\frac{\partial\overline{w}}{\partial\phi}\right|_{z_{w,k-1}}\right]\right] \tag{4.36}$$

$$\begin{aligned}\overline{\overline{\Sigma\phi\mathrm{r}}} &= \frac{1}{r_{p,i}\Delta r_{p,i}}\left[\left.\overline{v}\right|_{r_{u,i}} - \left.\overline{v}\right|_{r_{u,i-1}}\right] \\ &+ \frac{1}{r_{p,i}^2\Delta\phi}\left[\left.\overline{u}\right|_{\phi_{p,j+1}} - \left.\overline{u}\right|_{\phi_{p,j}} - \overline{\overline{v}}\Delta\phi\right]\end{aligned} \tag{4.37}$$

and:

$$
\begin{aligned}
\overline{\overline{\mathrm{r\Sigma zr}}} &= \frac{r_{u,i}}{r_{p,i}\Delta r_{p,i}}\left[\left.\frac{\partial\overline{w}}{\partial r}\right|_{r_{u,i}} + \left.\frac{\partial\overline{u}}{\partial z}\right|_{r_{u,i}}\right] \\
&- \frac{r_{u,i-1}}{r_{p,i}\Delta r_{p,i}}\left[\left.\frac{\partial\overline{w}}{\partial r}\right|_{r_{u,i-1}} + \left.\frac{\partial\overline{u}}{\partial z}\right|_{r_{u,i-1}}\right] \qquad (4.38) \\
\overline{\overline{\Sigma\mathrm{z}\phi}} &= \frac{1}{r_{p,i}\Delta\phi}\left[\left.\frac{\partial\overline{v}}{\partial z}\right|_{\phi_{v,j}} - \left.\frac{\partial\overline{v}}{\partial z}\right|_{\phi_{v,j-1}}\right] \\
&+ \frac{1}{r_{p,i}^2\Delta\phi}\left[\left.\frac{\partial\overline{w}}{\partial\phi}\right|_{\phi_{v,j}} - \left.\frac{\partial\overline{w}}{\partial\phi}\right|_{\phi_{v,j-1}}\right] \qquad (4.39) \\
\overline{\overline{\Sigma\mathrm{zz}}} &= \frac{2}{\Delta z}\left[\left.\frac{\partial\overline{w}}{\partial z}\right|_{z_{p,k+1}} - \left.\frac{\partial\overline{w}}{\partial z}\right|_{z_{p,k}}\right] \qquad (4.40)
\end{aligned}
$$

for the streamwise component. Below the sets of linear equations are given which are solved for interpolation and derivatives. To interpolate the velocity u or take its derivative with respect to r at position $r_{p,i}$, the following set of equations has to be solved:

$$
\begin{pmatrix}
1 & \Delta r_{i+1} & \Delta r_{i+1}^2 & \Delta r_{i+1}^3 \\
1 & \Delta r_i & \Delta r_i^2 & \Delta r_i^3 \\
1 & \Delta r_{i-1} & \Delta r_{i-1}^2 & \Delta r_{i-1}^3 \\
1 & \Delta r_{i-2} & \Delta r_{i-2}^2 & \Delta r_{i-2}^3
\end{pmatrix}
\begin{pmatrix} a_0 \\ a_1 \\ a_2 \\ a_3 \end{pmatrix}
=
\begin{pmatrix} u_{i+1,j,k} \\ u_{i\quad,j,k} \\ u_{i-1,j,k} \\ u_{i-2,j,k} \end{pmatrix} \qquad (4.41)
$$

with:

$$
\begin{aligned}
\Delta r_{i+1} &= r_{u,i+1} - r_{p,i} \\
\Delta r_i &= r_{u,i} - r_{p,i} \qquad (4.42) \\
\Delta r_{i-1} &= r_{u,i-1} - r_{p,i} \\
\Delta r_{i-2} &= r_{u,i-2} - r_{p,i}
\end{aligned}
$$

For interpolation only a_0 is needed, and for the derivative only a_1. To interpolate the velocity v or take its derivative with respect to r at position $r_{u,i}$, the following, slightly different, set of equations has to be solved:

$$\begin{pmatrix} 1 & \Delta r_{i+2} & \Delta r_{i+2}^2 & \Delta r_{i+2}^3 \\ 1 & \Delta r_{i+1} & \Delta r_{i+1}^2 & \Delta r_{i+1}^3 \\ 1 & \Delta r_i & \Delta r_i^2 & \Delta r_i^3 \\ 1 & \Delta r_{i-1} & \Delta r_{i-1}^2 & \Delta r_{i-1}^3 \end{pmatrix} \begin{pmatrix} b_0 \\ b_1 \\ b_2 \\ b_3 \end{pmatrix} = \begin{pmatrix} v_{i+2,j,k} \\ v_{i+1,j,k} \\ v_{i\quad,j,k} \\ v_{i-1,j,k} \end{pmatrix} \tag{4.43}$$

with:

$$\begin{aligned} \Delta r_{i+2} &= r_{p,i+2} - r_{u,i} \\ \Delta r_{i+1} &= r_{p,i+1} - r_{u,i} \\ \Delta r_i &= r_{p,i} \quad - r_{u,i} \\ \Delta r_{i-1} &= r_{p,i-1} - r_{u,i} \end{aligned} \tag{4.44}$$

This time, for interpolation only b_0 is needed, and for the derivative b_1. Both of the above sets of equations are for the non-homogeneous radial direction. For the homogeneous angular and streamwise directions the example below can easily be adapted. For the velocity v or its derivative with respect to ϕ at position $\phi_{p,j}$ this set of equations has to be solved.

$$\begin{pmatrix} 1 & \left(+\frac{3}{2}\Delta\phi\right) & \left(+\frac{3}{2}\Delta\phi\right)^2 & \left(+\frac{3}{2}\Delta\phi\right)^3 \\ 1 & \left(+\frac{1}{2}\Delta\phi\right) & \left(+\frac{1}{2}\Delta\phi\right)^2 & \left(+\frac{1}{2}\Delta\phi\right)^3 \\ 1 & \left(-\frac{1}{2}\Delta\phi\right) & \left(-\frac{1}{2}\Delta\phi\right)^2 & \left(-\frac{1}{2}\Delta\phi\right)^3 \\ 1 & \left(-\frac{3}{2}\Delta\phi\right) & \left(-\frac{3}{2}\Delta\phi\right)^2 & \left(-\frac{3}{2}\Delta\phi\right)^3 \end{pmatrix} \begin{pmatrix} c_0 \\ c_1 \\ c_2 \\ c_3 \end{pmatrix} = \begin{pmatrix} v_{i,j+1,k} \\ v_{i,j\quad,k} \\ v_{i,j-1,k} \\ v_{i,j-2,k} \end{pmatrix} \tag{4.45}$$

For the velocity w or its derivative with respect to z at position $z_{p.k}$ one can simply replace $\Delta\phi$, with Δz. As for the radial direction, c_0 gives the interpolated value and c_1 the derivative.

4.4 Predictor

As explained in Eggels (1994), the predictor calculates the velocity, $\bar{\mathbf{v}}^*$, from the advection term, the diffusion term, and the pressure gradient over the pipe. To increase the maximal time step at which the code is stable, terms containing spatial derivatives to ϕ are calculated implicitly using the Crank-Nicolson scheme for the advective terms, and the Backward Euler scheme for diffusive terms. This gives a system of equations that looks like:

$$\mathbf{A}'\,\bar{\mathbf{v}}^* = \mathbf{b} \tag{4.46}$$

where, because of the 4th order algorithm, our nearly diagonal matrix $\mathbf{A}'$ looks like:

$$A' = \begin{pmatrix} c_1 & d_1 & e_1 & \cdots & \cdots & \cdots & \cdots & a_1 & b_1 \\ b_2 & c_2 & d_2 & e_2 & \cdots & \cdots & \cdots & \cdots & a_2 \\ a_3 & b_3 & c_3 & d_3 & e_3 & & & & \vdots \\ \vdots & \ddots & \ddots & \ddots & \ddots & \ddots & & & \vdots \\ \vdots & & \ddots & \ddots & \ddots & \ddots & \ddots & & \vdots \\ \vdots & & & \ddots & \ddots & \ddots & \ddots & \ddots & \vdots \\ \vdots & & & & a_{n-2} & b_{n-2} & c_{n-2} & d_{n-2} & e_{n-2} \\ e_{n-1} & \cdots & \cdots & \cdots & \cdots & a_{n-1} & b_{n-1} & c_{n-1} & d_{n-1} \\ d_n & e_n & \cdots & \cdots & \cdots & \cdots & a_n & b_n & c_n \end{pmatrix} \tag{4.47}$$

Solving the system in equation 4.46 for $\bar{\mathbf{v}}^*$ directly, would require a lot of computational resources, both processor cycles and memory, so instead the Woodbury matrix identity is used. This identity states that the inverse of matrix A plus perturbation matrix UCV is equal to:

$$(A + UCV)^{-1} = A^{-1} - A^{-1}U(C^{-1} + VA^{-1}U)^{-1}VA^{-1} \tag{4.48}$$

This way our problem can be split up in a fully diagonal matrix:

$$A = \begin{pmatrix} (c_1 - a_1) & (d_1 - b_1) & e_1 & \cdots & \cdots & \cdots & \\ b_2 & (c_2 - a_2) & d_2 & e_2 & & & \vdots \\ \vdots & \ddots & \ddots & \ddots & \ddots & & \vdots \\ \vdots & & \ddots & \ddots & \ddots & \ddots & \vdots \\ \vdots & & & a_{n-1} & b_{n-1} & (c_{n-1} - e_{n-1}) & d_{n-1} \\ & \cdots & \cdots & \cdots & a_n & (b_n - d_n) & (c_n - e_n) \end{pmatrix} \tag{4.49}$$

and a rank-2 perturbation matrix:

$$UCV = \begin{pmatrix} a_1 & b_1 & \cdots & \cdots & \cdots & a_1 & b_1 \\ \vdots & a_2 & & & & & a_2 \\ \vdots & & & & & & \vdots \\ \vdots & & & & & & \vdots \\ \vdots & & & & & & \vdots \\ e_{n-1} & & & & & e_{n-1} & \vdots \\ d_n & e_n & \cdots & \cdots & \cdots & d_n & e_n \end{pmatrix} \tag{4.50}$$

which, when summed up, are equal to the original matrix, $A + UCV = A'$. The reason that using the Woodbury identity is very efficient, is that the diagonal matrix A and the matrix $C^{-1} + VA^{-1}U$ are a lot cheaper to invert than the full matrix A', and one can use LU factorization of matrix A to deal with all terms that involve A^{-1}.

There are several ways in which the perturbation matrix can be composed out of U, C, and V. In the predictor code the matrices have the following form:

$$U = \begin{pmatrix} a_1 & b_1 \\ 0 & a_2 \\ \vdots & \vdots \\ e_{n-1} & 0 \\ d_n & e_n \end{pmatrix} \tag{4.51}$$

$$C = \begin{pmatrix} 1 & 0 \\ 0 & 1 \end{pmatrix} \tag{4.52}$$

$$V = \begin{pmatrix} 1 & 0 & \cdots & 1 & 0 \\ 0 & 1 & \cdots & 0 & 1 \end{pmatrix} \tag{4.53}$$

This way different matrices in the code always consist of numbers of about the same order, which gives the highest accuracy and stability.

The way the algorithm works is to first factorize the matrix A using LU decomposition and use the factorized form of matrix A to solve the following set of equations:

$$AZ = U \tag{4.54}$$

$$WA = V \tag{4.55}$$

$$A\mathbf{x} = \mathbf{b} \tag{4.56}$$

Substituting these expressions back in equation 4.48 gives:

$$(A + UCV)^{-1}\mathbf{b} = \mathbf{x} - Z(C^{-1} + VZ)^{-1}W\mathbf{b} \tag{4.57}$$

Now the inverse of $(C^{-1} + VZ)$ is calculated and multiplied with Z, and $W\mathbf{b}$ is calculated:

$$R = Z(C^{-1} + VZ)^{-1} \tag{4.58}$$

$$\mathbf{s} = W\mathbf{b} \tag{4.59}$$

This gives for the predicted velocity, $\bar{\mathbf{v}}^*$:

$$\bar{\mathbf{v}}^* = (A + UCV)^{-1}\mathbf{b} = \mathbf{x} - R\mathbf{s} \tag{4.60}$$

Because only terms containing spacial derivatives in the ϕ direction are solved implicitly, $\bar{\mathbf{v}}^*$ is solved for one value of the indices i and k at a time (i.e. rings with the same i, and k index, but the j index going from $j = 1$ to $j = j_{\max}$). Since the domain is divided up in pie slices, data needs to be be redistributed into these rings on different processors, and after calculating $\bar{\mathbf{v}}^*$, the data needs to be distributed in slices again. The algorithm is designed to be non-blocking. As soon as the first data arrives at a processor, it starts solving for the resulting predicted velocity with the corresponding i and k indices, while more data is still arriving. Also, calculated velocities are immediately send back after their calculation finishes.

4.5 Poisson solver

Because the FFT library used in the original Fast Poisson Solver, written by Eggels (1994), was only suitable for serial processing, a new Poisson solver was written, based on the Fastest Fourier Transform of the West (FFTW) library.

The domain on which the Poisson equation is solved is a cylinder of radius $r = 0.5$, and length $z = 5$. The point $\phi_{i,j,k}$ is defined in the middle of a grid cell, to avoid singularities in the center. The Poisson equation in cylindrical coordinates equals:

$$\Delta\phi = \frac{1}{r}\frac{\partial}{\partial r}\left(r\frac{\partial\phi}{\partial r}\right) + \frac{1}{r^2}\frac{\partial^2\phi}{\partial\theta^2} + \frac{\partial^2\phi}{\partial z^2} = f \tag{4.61}$$

The boundary conditions in the streamwise and angular direction are periodic, and for the radial direction the Neumann boundary condition is applied at the wall:

$$g = \frac{\partial}{\partial r}\phi\,(0.5) = 0 \tag{4.62}$$

and the continuity condition is applied in the center:

$$\phi\left(0,\theta,z\right)=\phi\left(0,\theta+\pi,z\right) \tag{4.63}$$

However, because of the Neumann boundary condition at the wall the solution of this set of equations is not well defined, since every solutions plus or minus any constant is also a solution. To obtain a solution the compatibility condition needs to be applied:

$$\int_{\omega} f dV=\int_{\delta\omega} g dS \tag{4.64}$$

where, because of the cylindrical coordinates, $dV = rdr\ d\phi\ dz$. Because of the Neumann boundary condition at the wall (i.e. $g = 0$), the compatibility condition states that the integral over f needs to be zero.

Taking the Fast Fourier Transform in both streamwise and angular direction, the above equation becomes:

$$\frac{1}{r}\frac{\partial}{\partial r}\left(r\frac{\partial\tilde{\phi}_{j,k}}{\partial r}\right)-\frac{k_{\theta}^{2}}{r^{2}}\tilde{\phi}_{j,k}-k_{z}^{2}\tilde{\phi}_{j,k}=\tilde{f}_{j,k} \tag{4.65}$$

where the periodic boundary conditions in streamwise and angular direction are automatically satisfied due to the nature of FFT and the boundary conditions in radial directions are:

$$\frac{\partial}{\partial r}\tilde{\phi}_{j,k}\left(0.5\right)=0 \tag{4.66}$$

and:

$$\tilde{\phi}_{j,k}\left(0\right)=\tilde{\phi}_{j,k}\left(0\right)\exp\left(i\pi k_{\theta}\right) \tag{4.67}$$

The compatibility condition in Fourier space becomes:

$$\int_{0}^{0.5}\tilde{f}_{0,0}\left(r\right)rdr=0 \tag{4.68}$$

When discretizing the above differential equation, it has to be accounted for that the discretization has to be done on a non-uniform grid. The first version of the newly written Poisson solver dealt with this, as explained by Moin (2001), by transforming the grid back to a uniform grid and solving the differential equation on this uniform grid instead of the non-uniform grid. Defining $\zeta = g(r)$ as the grid function, which transforms evenly distributed points in ζ to non-uniform spacing in r, we can write for the first derivative:

$$\frac{d}{dr}\tilde{\phi}_{j,k} = \frac{d\zeta}{dr}\frac{d}{d\zeta}\tilde{\phi}_{j,k} = g'(r)\frac{d}{d\zeta}\tilde{\phi}_{j,k} \tag{4.69}$$

and:

$$\frac{d^2}{dr^2}\tilde{\phi}_{j,k} = \frac{d}{dr}\left[g'(r)\frac{d}{d\zeta}\tilde{\phi}_{j,k}\right] = g''(r)\frac{d}{d\zeta}\tilde{\phi}_{j,k} + g'(r)^2\frac{d^2}{d\zeta^2}\tilde{\phi}_{j,k} \tag{4.70}$$

for the second derivative. However, it was found that this method gave and increasing absolute error at the wall with decreasing mesh size instead of becoming more accurate.

Instead, it was then decided to solve equation 4.65 directly on the non-uniform grid. By solving the set of linear equations:

$$\begin{pmatrix} 1 & \Delta r_{i+2} & \Delta r_{i+2}^2 & \Delta r_{i+2}^3 & \Delta r_{i+2}^4 \\ 1 & \Delta r_{i+1} & \Delta r_{i+1}^2 & \Delta r_{i+1}^3 & \Delta r_{i+1}^4 \\ 1 & \Delta r_{i} & \Delta r_{i}^2 & \Delta r_{i}^3 & \Delta r_{i}^4 \\ 1 & \Delta r_{i-1} & \Delta r_{i-1}^2 & \Delta r_{i-1}^3 & \Delta r_{i-1}^4 \\ 1 & \Delta r_{i-2} & \Delta r_{i-2}^2 & \Delta r_{i-2}^3 & \Delta r_{i-2}^4 \end{pmatrix} \begin{pmatrix} a_{0,i} \\ a_{1,i} \\ a_{2,i} \\ a_{3,i} \\ a_{4,i} \end{pmatrix} = \begin{pmatrix} \tilde{\phi}_{i+2,j,k} \\ \tilde{\phi}_{i+1,j,k} \\ \tilde{\phi}_{i\quad,j,k} \\ \tilde{\phi}_{i-1,j,k} \\ \tilde{\phi}_{i-2,j,k} \end{pmatrix} \tag{4.71}$$

the coefficients $a_{0,i}$, $a_{1,i}$, $a_{2,i}$, $a_{3,i}$, and $a_{4,i}$ can be found. Then, after substituting:

$$\begin{aligned}
\Delta r_{i+2} &= r_{p,i+2} - r_{p,i} \\
\Delta r_{i+1} &= r_{p,i+1} - r_{p,i} \\
\Delta r_{i} &= r_{p,i} - r_{p,i} \,(=0) \\
\Delta r_{i-1} &= r_{p,i-1} - r_{p,i} \\
\Delta r_{i-2} &= r_{p,i-2} - r_{p,i}
\end{aligned} \tag{4.72}$$

the first and second derivative can be found to be:

$$\frac{d}{dr}\tilde{\phi}_{j,k}\left(r_{p,i}\right) = a_{1,i} \tag{4.73}$$

$$\frac{d^2}{dr^2}\tilde{\phi}_{j,k}\left(r_{p,i}\right) = 2a_{2,i} \tag{4.74}$$

where the other coefficients disappear because $\Delta r_i = r_{p,i} - r_{p,i} = 0$. All coefficients, including $a_{1,i}$ and $a_{2,i}$, are linear combinations of, $\tilde{\phi}_{i+2,j,k}$, $\tilde{\phi}_{i+1,j,k}$, $\tilde{\phi}_{i,j,k}$, $\tilde{\phi}_{i-1,j,k}$, and $\tilde{\phi}_{i-2,j,k}$. and thus one can also write the above equations as:

$$\frac{d}{dr}\tilde{\phi}_{j,k}\left(r_{p,i}\right) = \sum_{l=-2}^{2} a_{1,i,l}\ \tilde{\phi}_{i+l,j,k} \tag{4.75}$$

$$\frac{d^2}{dr^2}\tilde{\phi}_{j,k}\left(r_{p,i}\right) = 2\sum_{l=-2}^{2} a_{2,i,l}\ \tilde{\phi}_{i+l,j,k} \tag{4.76}$$

Substituting these equations in equation 4.65 gives its discretized form:

$$\sum_{l=-2}^{2}\left(\frac{a_{1,i,l}}{r_{p,i}} + 2\ a_{2,i,l}\right)\tilde{\phi}_{i+l,j,k} - \left(\frac{k_\theta^2}{r_{p,i}^2} + k_z^2\right)\tilde{\phi}_{i,j,k} = \tilde{f}_{i,j,k} \tag{4.77}$$

In the center the discretized boundary condition equals:

$$\tilde{\phi}_{0,j,k} = \tilde{\phi}_{1,j,k}\exp\left(i\pi k_\theta\right) \tag{4.78}$$

At the wall the discretized boundary condition is determined by first solving the set of equations:

$$\begin{pmatrix} 1 & \Delta r_{+1/2} & \Delta r_{+1/2}^2 & \Delta r_{+1/2}^3 \\ 1 & \Delta r_{-1/2} & \Delta r_{-1/2}^2 & \Delta r_{-1/2}^3 \\ 1 & \Delta r_{-3/2} & \Delta r_{-3/2}^2 & \Delta r_{-3/2}^3 \\ 1 & \Delta r_{-5/2} & \Delta r_{-5/2}^2 & \Delta r_{-5/2}^3 \end{pmatrix} \begin{pmatrix} b_0 \\ b_1 \\ b_2 \\ b_3 \end{pmatrix} = \begin{pmatrix} \tilde{\phi}_{i_{\max}+1,j,k} \\ \tilde{\phi}_{i_{\max},j,k} \\ \tilde{\phi}_{i_{\max}-1,j,k} \\ \tilde{\phi}_{i_{\max}-2,j,k} \end{pmatrix} \tag{4.79}$$

with:

$$\begin{aligned} \Delta r_{+1/2} &= r_{p,i_{\max}+1} - r_{u,i_{\max}} \\ \Delta r_{-1/2} &= r_{p,i_{\max}} - r_{u,i_{\max}} \\ \Delta r_{-3/2} &= r_{p,i_{\max}-1} - r_{u,i_{\max}} \\ \Delta r_{-5/2} &= r_{p,i_{\max}-2} - r_{u,i_{\max}} \end{aligned} \tag{4.80}$$

where $r_{u,i_{\max}} = 0.5$. Then, because the derivative at the wall is zero, b_1 is set to zero to find $\tilde{\phi}_{i_{\max}+1,j,k}$. This gives an expression of the form:

$$\tilde{\phi}_{i_{\max}+1,j,k} = \sum_{l=-2}^{0} -\frac{b_{1,l}}{b_{1,1}} \tilde{\phi}_{i_{\max}+l,j,k} \tag{4.81}$$

The actual calculation is performed in the Poisson solver in the following way: the FFTW library uses slab decomposition to split up the computational domain, while the rest of the code splits up the domain pie slices, because of the cylindrical geometry of the domain. Therefore all data of the different slices is first send to the root process, who redistributes it in slabs to the appropriate processes. Then FFTW is called to perform the 2-D FFT in streamwise and angular direction, which gives the set of linear equations shown in equation 4.77. After putting these in a matrix for each i and j index, and applying the compatibility condition, these equations are solved

using the LAPACK library. Then, after normalization and performing the backward FFT, all data is transformed from slab decomposition into slice decomposition again and the final result is returned by the subroutine.

4.6 Boundary conditions

For the continuous phase, the boundary conditions with the other processors, and the boundary conditions at the wall are enforced using ghost cells. Ghost cells are grid cells which are outside of the domain on which all equations are solved, but are given a value so that boundary conditions are obeyed. Since the algorithm for solving the Navier Stokes equation is 4th order, two rows of ghost cells are needed on each side of a sub-domain for both all the velocity components and the pressure field. All ghost cells have to be updated every time step. For the ghost cells in the angular and streamwise direction the procedure for updating them is shown in figures 4.4 through 4.7, and figure 4.3 shows the situation before any cell is updated. The updating procedure is the same for all velocity components and the pressure. "I" denotes an internal grid cell (i.e. j is on the interval $(1, jj_{\max})$ and k on $(1, kk_{\max})$), "E" denotes an external grid cell (i.e. a ghost cell), and different colors denote different positions. All sub-domains call themselves sub-domain 0, 1 is the sub-domain to the right with a smaller angle ϕ, 2 is to the left with larger ϕ, 3 is upstream with a smaller z, and 4 is downstream with a larger value of z. Figure 4.4 shows the first step in updating the ghost cells. All processors send the values of the cells with indices $j = jj_{\max} - 1$, and $j = jj_{\max}$ to processor 2, and all processors receive this information from processor 1 and update the values of the cells with indices $j = -1$, and $j = 0$. The next cells to be updated are the ghost cells with indices $k = kk_{\max} + 1$, and $k = kk_{\max} + 2$. All processors send a copy of the cells with indices $k = 1$, and $k = 2$ to processor 4, and all processors receive the data from processor 3. The result of this can be seen in figure 4.5. In figure 4.6 the ghost cells with indices $j = jj_{\max} + 1$, and $j = jj_{\max} + 2$

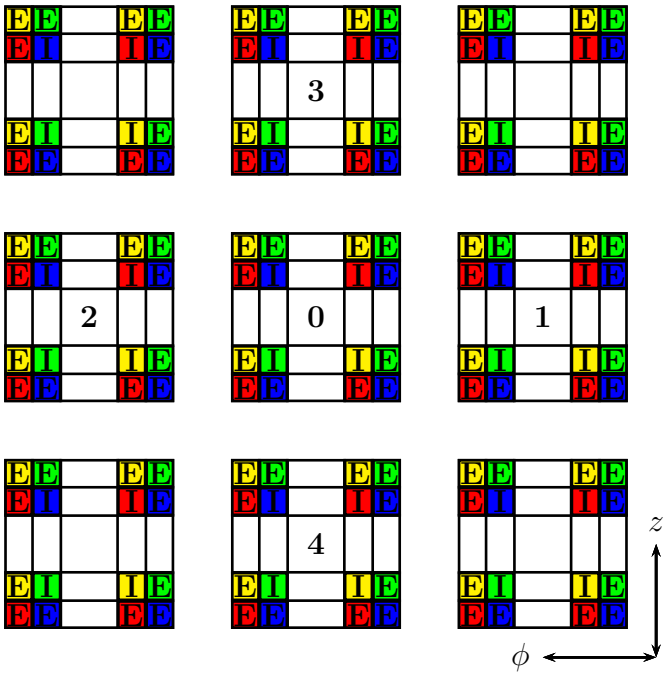

Figure 4.3 – Initial state of ghost cells. This diagram shows the sub-domain right before the ghost cells are updated.

are updated and in figure 4.7 the updating routine is completed by updating the cells with indices $k = -1$, and $k = 0$. The ghost cells now all have been updated by values of internal cells at neighboring sub-domains. Also note that by performing the update routine in clockwise (or counter clockwise) direction there is no extra communication needed to update the cells on the corner of each sub-domain. The ghost cells which have to be updated next are the ghost cells for the wall and for the center. Since the grid is staggered and because the pressure has a different boundary condition at the wall than the velocities, the updating procedure depends on the variable.

The first variable to be analyzed is the radial velocity, u. Because of the position of the u vector in the staggered grid, $u_{0,j,k}$ is exactly in the center of the pipe, and $u_{i_{\max},j,k}$ is exactly on the wall. Because of the no-slip condition at the wall, u can simply be set to zero at that position, $u_{i_{\max},j,k} = 0$. In the center initially the value

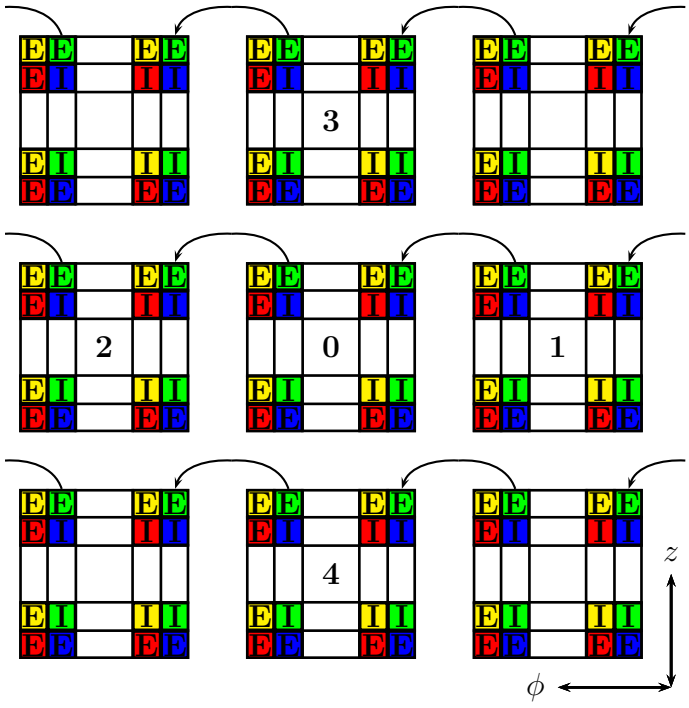

Figure 4.4 – Ghost cell configuration after the first update. The values of the ghost cells after updating the cells with indices $j = -1$, and $j = 0$.

of $u_{0,j,k}$ was calculated using a scheme which used the interpolated values of both u and v for all different angles to calculated an averaged value for $u_{0,j,k}$. However, this algorithm turned out to suppress velocity fluctuations in the center, and it was decided to switch to much simpeler interpolation using only $u_{1,j,k}$ and $u_{-1,j,k}$.

$$u_{0,j,k} = \frac{1}{2}\left(u_{1,j,k} + u_{-1,j,k}\right) \tag{4.82}$$

This is done for all values of j and now the radial velocity is well defined in the center. The value of $u_{-1,j,k}$ is calculated using the fact that $u(r, \phi, z) = -u(r, \phi+\pi, z)$, so:

$$u_{-1,j,k} = -u_{1,j+\frac{j_{\max}}{2},k} \tag{4.83}$$

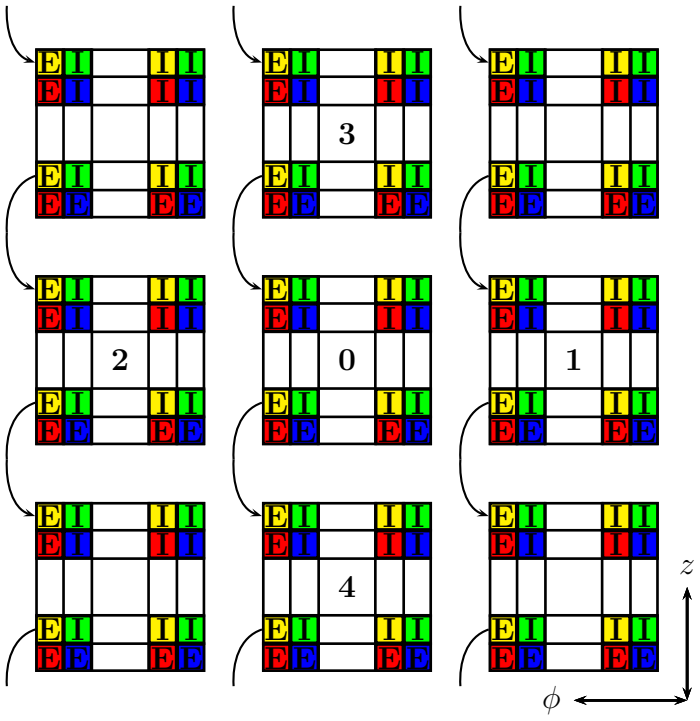

Figure 4.5 – Ghost cell configuration after the second update. The values of the ghost cells after updating the cells with indices $k = kk_{\max} + 1$, and $k = kk_{\max} + 2$.

Now only the ghost cells $u_{i_{\max}+1,j,k}$, and $u_{i_{\max}+2,j,k}$ are left. At the wall the discretized boundary condition is determined by first solving the set of equations:

$$\begin{pmatrix} 1 & \Delta r_{+1} & \Delta r_{+1}^2 & \Delta r_{+1}^3 \\ 1 & \Delta r_{-1} & \Delta r_{-1}^2 & \Delta r_{-1}^3 \\ 1 & \Delta r_{-2} & \Delta r_{-2}^2 & \Delta r_{-2}^3 \\ 1 & \Delta r_{-3} & \Delta r_{-3}^2 & \Delta r_{-3}^3 \end{pmatrix} \begin{pmatrix} b_0 \\ b_1 \\ b_2 \\ b_3 \end{pmatrix} = \begin{pmatrix} u_{i_{\max}+1,j,k} \\ u_{i_{\max}\quad,j,k} \\ u_{i_{\max}-1,j,k} \\ u_{i_{\max}-2,j,k} \end{pmatrix} \tag{4.84}$$

with:

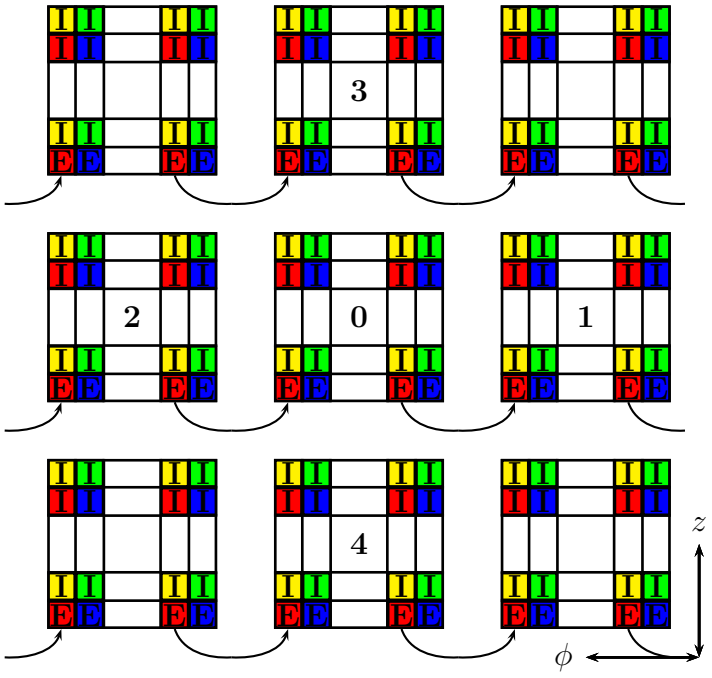

Figure 4.6 – **Ghost cell configuration after the third update.** The values of the ghost cells after updating the cells with indices $j = jj_{\max} + 1$, and $j = jj_{\max} + 2$.

$$\begin{aligned} \Delta r_{+1} &= r_{u,i_{\max}+1} - r_{u,i_{\max}} \\ \Delta r_{-1} &= r_{u,i_{\max}} - r_{u,i_{\max}} \\ \Delta r_{-2} &= r_{u,i_{\max}-1} - r_{u,i_{\max}} \\ \Delta r_{-3} &= r_{u,i_{\max}-2} - r_{u,i_{\max}} \end{aligned} \tag{4.85}$$

where $r_{u,i_{\max}} = 0.5$. Then, because the at the wall there is the no-slip condition for all velocity components, b_0 is set to zero to find $u_{i_{\max}+1,j,k}$. This gives an expression of the form:

$$u_{i_{\max}+1,j,k} = \sum_{l=-2}^{0} -\frac{b_{0,l}}{b_{0,1}} u_{i_{\max}+l,j,k} \tag{4.86}$$

where $u_{i_{\max},j,k}$ is set to zero. To determine $u_{i_{\max}+2,j,k}$, a new set of equations is solved:

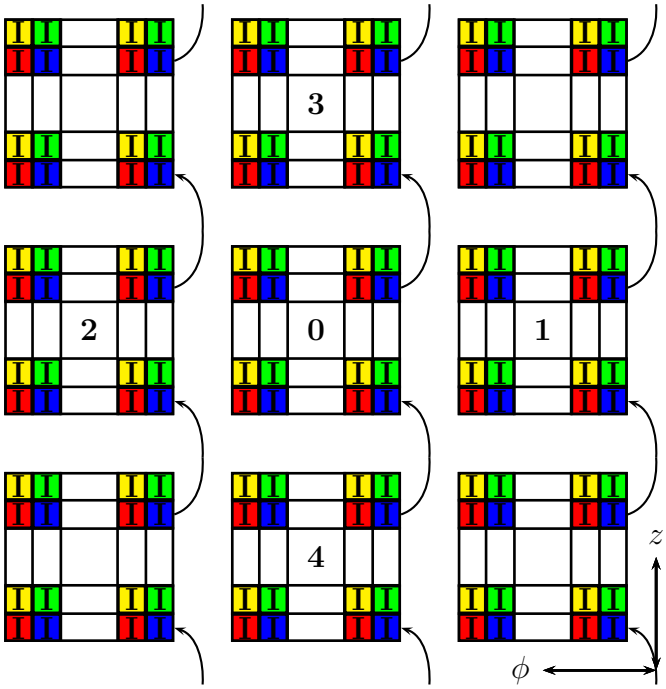

Figure 4.7 – **Ghost cell configuration after the final update.** The last and fourth stage of the update routine. The values of the ghost cells after updating the cells with indices $k = -1$, and $k = 0$.

$$\begin{pmatrix} 1 & \Delta r_{+2} & \Delta r_{+2}^2 & \Delta r_{+2}^3 & \Delta r_{+2}^4 \\ 1 & \Delta r_{+1} & \Delta r_{+1}^2 & \Delta r_{+1}^3 & \Delta r_{+1}^4 \\ 1 & \Delta r & \Delta r^2 & \Delta r^3 & \Delta r^4 \\ 1 & \Delta r_{-1} & \Delta r_{-1}^2 & \Delta r_{-1}^3 & \Delta r_{-1}^4 \\ 1 & \Delta r_{-2} & \Delta r_{-2}^2 & \Delta r_{-2}^3 & \Delta r_{-2}^4 \end{pmatrix} \begin{pmatrix} c_0 \\ c_1 \\ c_2 \\ c_3 \\ c_4 \end{pmatrix} = \begin{pmatrix} u_{i_{\max}+2,j,k} \\ u_{i_{\max}+1,j,k} \\ u_{i_{\max}\quad,j,k} \\ u_{i_{\max}-1,j,k} \\ u_{i_{\max}-2,j,k} \end{pmatrix} \tag{4.87}$$

with:

$$
\begin{aligned}
\Delta r_{+2} &= r_{u,i_{\max}+2} - r_{u,i_{\max}} \\
\Delta r_{+1} &= r_{u,i_{\max}+1} - r_{u,i_{\max}} \\
\Delta r &= r_{u,i_{\max}} - r_{u,i_{\max}} \\
\Delta r_{-1} &= r_{u,i_{\max}-1} - r_{u,i_{\max}} \\
\Delta r_{-2} &= r_{u,i_{\max}-2} - r_{u,i_{\max}}
\end{aligned}
\tag{4.88}
$$

The previously calculated expression for $u_{i_{\max}+1,j,k}$ is substituted in and also $u_{i_{\max},j,k} = 0$. Again, because of the no-slip condition at the wall, c_0 is set to zero. The resulting expression has the same form as the equation for $u_{i_{\max}+1,j,k}$ and looks like:

$$
u_{i_{\max}+2,j,k} = \sum_{l=-2}^{0} -\frac{c_{0,l}}{c_{0,2}} u_{i_{\max}+l,j,k} \tag{4.89}
$$

All ghost cells for the radial velocity u have now been updated.

For the angular and streamwise velocities, v and w,and for the pressure p the ghost cells are updated in a similar way, except that they are not located right at the wall or in the center. This changes the equations to extrapolate the values at $i = i_{\max} + 1$ and $i = i_{\max} + 2$. For $v_{i_{\max}+1,j,k}$ the equations look like:

$$
\begin{pmatrix}
1 & \Delta r_{+1/2} & \Delta r_{+1/2}^2 & \Delta r_{+1/2}^3 \\
1 & \Delta r_{-1/2} & \Delta r_{-1/2}^2 & \Delta r_{-1/2}^3 \\
1 & \Delta r_{-3/2} & \Delta r_{-3/2}^2 & \Delta r_{-3/2}^3 \\
1 & \Delta r_{-5/2} & \Delta r_{-5/2}^2 & \Delta r_{-5/2}^3
\end{pmatrix}
\begin{pmatrix} b_0 \\ b_1 \\ b_2 \\ b_3 \end{pmatrix}
=
\begin{pmatrix}
v_{i_{\max}+1,j,k} \\
v_{i_{\max},j,k} \\
v_{i_{\max}-1,j,k} \\
v_{i_{\max}-2,j,k}
\end{pmatrix}
\tag{4.90}
$$

with:

$$
\begin{aligned}
\Delta r_{+1/2} &= r_{p,i_{\max}+1} - r_{u,i_{\max}} \\
\Delta r_{-1/2} &= r_{p,i_{\max}} - r_{u,i_{\max}} \\
\Delta r_{-3/2} &= r_{p,i_{\max}-1} - r_{u,i_{\max}} \\
\Delta r_{-5/2} &= r_{p,i_{\max}-2} - r_{u,i_{\max}}
\end{aligned}
\tag{4.91}
$$

and for $v_{i_{\max}+2,j,k}$ the equations are equal to:

$$
\begin{pmatrix}
1 & \Delta r_{+3/2} & \Delta r^2_{+3/2} & \Delta r^3_{+3/2} & \Delta r^4_{+3/2} \\
1 & \Delta r_{+1/2} & \Delta r^2_{+1/2} & \Delta r^3_{+1/2} & \Delta r^4_{+1/2} \\
1 & \Delta r_{-1/2} & \Delta r^2_{-1/2} & \Delta r^3_{-1/2} & \Delta r^4_{-1/2} \\
1 & \Delta r_{-3/2} & \Delta r^2_{-3/2} & \Delta r^3_{-3/2} & \Delta r^4_{-3/2} \\
1 & \Delta r_{-5/2} & \Delta r^2_{-5/2} & \Delta r^3_{-5/2} & \Delta r^4_{-5/2}
\end{pmatrix}
\begin{pmatrix} c_0 \\ c_1 \\ c_2 \\ c_3 \\ c_4 \end{pmatrix}
=
\begin{pmatrix}
v_{i_{\max}+2,j,k} \\
v_{i_{\max}+1,j,k} \\
v_{i_{\max},j,k} \\
v_{i_{\max}-1,j,k} \\
v_{i_{\max}-2,j,k}
\end{pmatrix}
\tag{4.92}
$$

with:

$$
\begin{aligned}
\Delta r_{+3/2} &= r_{p,i_{\max}+2} - r_{u,i_{\max}} \\
\Delta r_{+1/2} &= r_{p,i_{\max}+1} - r_{u,i_{\max}} \\
\Delta r_{-1/2} &= r_{p,i_{\max}} - r_{u,i_{\max}} \\
\Delta r_{-3/2} &= r_{p,i_{\max}-1} - r_{u,i_{\max}} \\
\Delta r_{-5/2} &= r_{p,i_{\max}-2} - r_{u,i_{\max}}
\end{aligned}
\tag{4.93}
$$

Solving these expressions for $b_0 = 0$, and $c_0 = 0$ gives the values of $v_{i_{\max}+1,j,k}$ and $v_{i_{\max}+2,j,k}$ respectively. The equations for extrapolating the streamwise velocity, w, are exactly the same as the equations for v. However, for the pressure the boundary condition at the wall is that the derivative of the pressure normal to the wall has to be zero. Therefore the ghost cell values for the pressure are calculated by setting b_1,

and c_1 to zero instead of b_0, and c_0. Also, in the center a similar procedure is followed as for the radial velocity:

$$\begin{aligned} v_{\ 0,j,k} &= -v_{1,j+\frac{j_{\max}}{2},k} \\ v_{-1,j,k} &= -v_{2,j+\frac{j_{\max}}{2},k} \\ w_{\ 0,j,k} &= w_{1,j+\frac{j_{\max}}{2},k} \\ w_{-1,j,k} &= w_{2,j+\frac{j_{\max}}{2},k} \\ p_{\ 0,j,k} &= p_{1,j+\frac{j_{\max}}{2},k} \\ p_{-1,j,k} &= p_{2,j+\frac{j_{\max}}{2},k} \end{aligned} \tag{4.94}$$

for all values of j, and k. This completes the updating routine for all ghost cells on all sides of each sub-domain.

4.7 Beads

The bead/particle tracking code is a Velocity Verlet algorithm (Swope et al. 1982) with the RATTLE (Andersen 1983) algorithm to take care of polymer chains which are fully stretched and fibers, and 2-way coupling with the solvent. The following conventions are used: the subscript n denotes time, the superscripts $*$ denotes the code's scaling in bulk units, and the index i_p denotes the index number of each bead. In its most basic form, the Velocity Verlet algorithm follows the following procedure: For each bead the intermediate velocity is determined at time $n + 1/2$:

$$\mathbf{v}^*_{n+1/2}(i_p) = \mathbf{v}^*_n(i_p) + \frac{1}{2}\mathbf{a}^*_n(i_p)\Delta t^* \tag{4.95}$$

The intermediate velocity is used to find the new position at time $n + 1$:

$$\mathbf{x}^*_{n+1}(i_p) = \mathbf{x}^*_n(i_p) + \mathbf{v}^*_{n+1/2}(i_p)\Delta t^* \tag{4.96}$$

The acceleration $\mathbf{a}_{n+1}(i_p)$ is determined at the new position $\mathbf{x}^*_{n+1}(i_p)$, and the velocity is updated using this acceleration:

$$\mathbf{v}^*_{n+1}(i_p) = \mathbf{v}^*_{n+1/2}(i_p) + \frac{1}{2}\mathbf{a}^*_{n+1}(i_p)\Delta t^* \tag{4.97}$$

Now all variables, $\mathbf{x}^*_{n+1}$, $\mathbf{v}^*_{n+1}$, and $\mathbf{a}^*_{n+1}$, are known at time $n+1$, and the algorithm starts all over again to find the positions, velocities, and accelerations for the next time step.

The acceleration $\mathbf{a}^*_{n+1}(i_p)$ has three contributions. i) a drag force ii) a spring force and iii) Brownian motion. To determine the drag force, first the slip velocity, $\mathbf{v}^*_s$, the difference between the velocity of the fluid at the position of a bead and the velocity of the bead itself, needs to be calculated:

$$\mathbf{v}^*_s = \mathbf{v}'^* \left(x_{n+1}\right) - \mathbf{v}^*_{n+1} \tag{4.98}$$

Here $\mathbf{v}'^* \left(x_{n+1}\right)$ is the solvent velocity at the position of the bead for which the drag is calculated, x_{n+1}. Using the slip velocity gives an acceleration due to drag which looks like:

$$\mathbf{a}^*_{\text{drag}}(i_p) = \frac{\mathbf{v}^*_s}{\tau^*_2} \tag{4.99}$$

where τ^*_2 is the non-dimensional particle relaxation time in bulk units:

$$\tau^*_2 = \frac{\text{Re}_\tau}{18}\frac{1}{\rho^* d^{*2}} \tag{4.100}$$

Because the slip velocity is based on the bead velocity at $n+1$ and not $n+1/2$, velocity $\mathbf{v}^*_{n+1}$ will have to be calculated implicitly.

The spring force between beads is calculated using the Finite Extensible Nonlinear Elastic (FENE) model. For two beads i_p, and j_p the spring force between them is

calculated as follows. Their separation is calculated by subtracting their position vectors:

$$\Delta \mathbf{x}^* = \mathbf{x}^*(j_p) - \mathbf{x}^*(i_p) \tag{4.101}$$

and then taking the square root of their inner product:

$$\Delta r^* = \sqrt{\Delta \mathbf{x}^* \cdot \Delta \mathbf{x}^*} \tag{4.102}$$

The deviation of the equilibrium value, Q, is equal to:

$$Q = \Delta r^* - \Delta r^*_{\text{eq}} \tag{4.103}$$

and with this value, $\Delta \mathbf{x}'^*$ can be calculated:

$$\Delta \mathbf{x}'^* = \frac{Q_0^2}{|Q_0^2 - Q^2|} Q \frac{\Delta \mathbf{x}^*}{\Delta r^*} \tag{4.104}$$

with:

$$Q_0 = \Delta r^*_{\text{max}} - \Delta r^*_{\text{eq}} \tag{4.105}$$

The absolute value in the denominator is there for computational stability. without it, in case the shear from the solvent accidently is so large in one time step that the polymer would be over-stretched, the attraction between two beads would change in repulsion. The Deborah number and particle relaxation time are used to calculate the non-dimensional acceleration caused by the spring force:

$$\mathbf{a}^*_{\text{spring}}(i_p) = \frac{\Delta \mathbf{x}'^*}{\text{De } \tau_2^*} \tag{4.106}$$

The last contribution to the acceleration is the Brownian motion. The equation for the acceleration components due to Brownian motion is:

$$\mathbf{a}^*_{\text{brown}}(i_p) = \sqrt{2D^*} \frac{f'^*_R}{\tau_2^*} \tag{4.107}$$

where $f_R'^*$ is a Gaussian variable with zero mean and unit variance created by a random number generator.

The the case polymers get stretched more than the FENE model allows or when simulating fibers, the RATTLE algorithm is used to keep beads at the right distance. This algorithm works by first adjusting the relative position of two beads, and then setting their relative velocity to zero. Combined with the force of the beads back on the solvent, the Velocity Verlet algorithm works as follows: First, just as in the algorithm shown above, the intermediate velocity is calculated:

$$\mathbf{v}^*_{n+1/2}(i_p) = \mathbf{v}^*_n(i_p) + \frac{1}{2}\mathbf{a}^*_n(i_p)\Delta t^* \tag{4.108}$$

and the intermediate velocity is used to find the new position at time $n+1$:

$$\mathbf{x}^*_{n+1}(i_p) = \mathbf{x}^*_n(i_p) + \mathbf{v}^*_{n+1/2}(i_p)\Delta t^* \tag{4.109}$$

Now the relative distance between two adjacent beads is determined by first subtracting their position vectors:

$$\Delta\mathbf{x}^* = \mathbf{x}^*(j_p) - \mathbf{x}^*(i_p) \tag{4.110}$$

and then taking the square root of inner product of the position difference:

$$\Delta r^* = \sqrt{\Delta\mathbf{x}^* \cdot \Delta\mathbf{x}^*} \tag{4.111}$$

The relative distance is used to calculate a correction term for the bead positions:

$$\mathbf{x}^*_0 = \frac{1}{2}\frac{\Delta\mathbf{x}^*}{\Delta r^*}\left(\Delta r^* - \Delta r^*_{\max}\right) \tag{4.112}$$

$$\mathbf{x}^*(i_p) = \mathbf{x}^*(i_p) + \mathbf{x}^*_0 \tag{4.113}$$

$$\mathbf{x}^*(j_p) = \mathbf{x}^*(j_p) - \mathbf{x}^*_0 \tag{4.114}$$

and also to to correct the velocities:

$$\begin{aligned} \mathbf{a}_0^* &= 2\frac{\mathbf{x}_0^*}{\Delta t^{*2}} && (4.115)\\ \mathbf{v}^*(i_p) &= \mathbf{v}^*(i_p) + \frac{1}{2}\mathbf{a}_0^*\Delta t^* && (4.116)\\ \mathbf{v}^*(j_p) &= \mathbf{v}^*(j_p) - \frac{1}{2}\mathbf{a}_0^*\Delta t^* && (4.117) \end{aligned}$$

The different contributions to the acceleration are calculated on the new corrected position:

$$\mathbf{a}_{n+1}^*(i_p) = \mathbf{a}_{\text{drag}}^*(i_p) + \mathbf{a}_{\text{spring}}^*(i_p) + \mathbf{a}_{\text{brown}}^*(i_p) \qquad (4.118)$$

with:

$$\mathbf{a}_{\text{drag}}^*(i_p) = \frac{1}{\tau_2^*}\left(\mathbf{v}'^*\left(x_{n+1}\right) - \mathbf{v}_{n+1}^*\right) \qquad (4.119)$$

This gives for the updated velocity:

$$\begin{aligned} \mathbf{v}_{n+1}^*(i_p) = & \\ & \left[\mathbf{v}_{n+1/2}^*(i_p)\right] / \left(1 + \frac{1}{2}\frac{\Delta t^*}{\tau_2^*}\right) \\ + \quad & \frac{\Delta t^*}{2}\left[\frac{\mathbf{v}'^*\left(x_{n+1}\right)}{\tau_2^*} + \mathbf{a}_{\text{spring}}^*(i_p) + \mathbf{a}_{\text{brown}}^*(i_p)\right] / \left(1 + \frac{1}{2}\frac{\Delta t^*}{\tau_2^*}\right) \qquad (4.120) \end{aligned}$$

The next part of the algorithm now corrects the velocity in such a way that for two neighboring beads the relative velocity in the direction of their connection vector is zero i.e. $\Delta v^* \cdot \Delta x^* = 0$. Using the usual procedure the connection vector is calculated:

$$\begin{aligned} \Delta\mathbf{x}^* &= \mathbf{x}^*(j_p) - \mathbf{x}^*(i_p) && (4.121)\\ \Delta r &= \sqrt{\Delta\mathbf{x}^* \cdot \Delta\mathbf{x}^*} && (4.122) \end{aligned}$$

Also, the total amount by which the velocity needs to be corrected, $\Delta v'^*$, is determined:

$$\Delta \mathbf{v}^* = \mathbf{v}^*(j_p) - \mathbf{v}^*(i_p) \tag{4.123}$$

$$\Delta v'^* = \Delta \mathbf{v}^* \cdot \frac{\Delta \mathbf{x}^*}{\Delta r} \tag{4.124}$$

After calculating the correction for each velocity component, the correction is applied to both the velocity:

$$\mathbf{v}_0 = \frac{\Delta v'^*}{2} \frac{\Delta \mathbf{x}^*}{\Delta r} \tag{4.125}$$

$$\mathbf{v}(i_p) = \mathbf{v}(i_p) + \mathbf{v}_0 \tag{4.126}$$

$$\mathbf{v}(j_p) = \mathbf{v}(j_p) - \mathbf{v}_0 \tag{4.127}$$

and the acceleration:

$$\mathbf{a}_0 = 2\frac{v_0}{\Delta t} \tag{4.128}$$

$$\mathbf{a}(i_p) = \mathbf{a}(i_p) + \mathbf{a}_0 \tag{4.129}$$

$$\mathbf{a}(j_p) = \mathbf{a}(j_p) - \mathbf{a}_0 \tag{4.130}$$

The last step now is to determine the force exerted on the solvent by the beads. To calculate the feedback an algorithm proposed by Elghobashi & Truesdell (1993) is used. The acceleration of the beads was calculated at position $\mathbf{x}^*_{n+1}(i_p)$ and the contribution from the solvent consist of the Brownian motion and the drag force. This means that the feedback on the solvent is equal to:

$$-\mathbf{a}^*_{\text{feedback}}(i_p) = \mathbf{a}^*_{\text{drag}}(i_p) + \mathbf{a}^*_{\text{brownian}}(i_p) \tag{4.131}$$

Multiplying the acceleration with the beads mass gives the actual force exerted on the fluid where the mass of a bead equals:

$$m^*_2 = \frac{3\pi}{\text{Re}_\tau} \frac{\tau^*_2}{d^*} \tag{4.132}$$

Using tri-linear interpolation in the bulk and barry-centric interpolation in the center, the force contribution to each grid cell in calculated. When summing up the different contributions of different beads, the force is divided by the volume of the grid cell it is acting on to turn it into a body force. The Velocity algorithm works in Cartesian coordinates so for the feedback the particle accelerations are converted to cylindrical coordinates.

Apart from the above algorithm to calculate the particle trajectories also the communication between processors when a polymer chain crosses from one sub-domain to an adjacent sub-domain needs to be implemented. To accurately capture the Brownian motion and the spring force, there are 100 iterations for the trajectories of the beads for every fluid time step. However, because the center of mass of a polymer chain moves along with the same velocity as the solvent, communication for chains crossing between sub-domains only takes place once every fluid time step. Chains can cross into neighboring sub-domains positioned either to the left, right, down stream, up stream, or the opposite laying sub-domain. To reduce communication overhead, there is a fixed buffer size for the amount of particles being send over. This way there is no extra communication needed to notify the receiving processor how large of a buffer it needs to allocate to receive all the particle data. When, after a number of iterations, the buffer size turns out to be too small or too large, it is adjusted automatically.

CHAPTER 5

RESULTS

In this section the results are show of the simulations for the three different Deborah numbers De = 0, De = 1, and De = 10. All simulations are at a friction Reynolds number $\mathrm{Re}_\tau = 560$ on a grid of $128 \times 256 \times 256$ grid cells. This is a slightly coarse grid, but considering other drag reduction work it is expected that the results will remain valid when the simulations are performed on a finer mesh (Choi et al. 1994).

5.1 Solvent

In figure 5.1 the average velocity profiles are shown. Because of the low polymer concentration not much drag reduction can be seen. However, considering the polymer stress tensor shown below, the highest amount of drag reduction is observed for a Deborah number of De = 0. Especially interesting is the comparison between the case of Deborah number of De = 0 and the other two cases. The Deborah numbers De = 1 and De = 10 are dumbbells consisting of two beads connected by FENE springs, while De = 0 is a dumbbell consisting of two beads connected by a fixed rod (i.e. the limit of an infinitely stiff spring) . With this comparison the fundamental difference between Lumley (1969) and De Gennes (1986) is addressed. Lumley considers drag reduction a local phenomenon, in the sense that he proposes that drag reduction stems from polymers locally changing the flow. De Gennes on the other hand considers it a non-local phenomenon. Polymers are stretched at one point in the flow storing turbulent kinetic energy in their backbone as potential energy, and release it at another place in the flow field, thus transporting turbulent kinetic

energy. Because the fibers (De = 0) show the most drag reduction, it has to be concluded that the dominant effect of polymers on the flow, at least in the low drag reduction regime, is the local modification of the flow, and that energy transport is negligible. Graph 5.2 shows the normal components of the Reynolds stress tensor. As

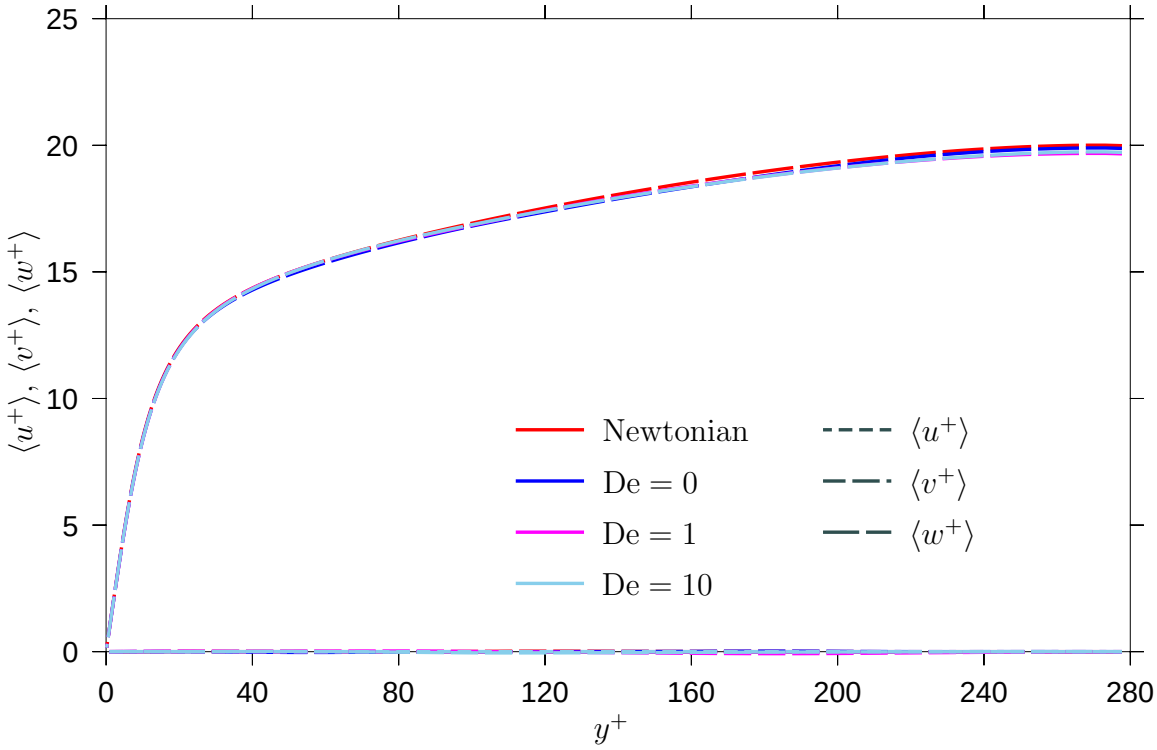

Figure 5.1 – Average mean velocity profiles for the solvent.

expected, the velocity fluctuations for simulations in which drag reduction is observed are lower than the simulation of a turbulent purely Newtonian liquid. In figure 5.3 the Reynolds shear stress, $\langle u^+w^+\rangle$, and total shear stress, $\langle\sigma_{rz}^+\rangle$, are plotted for all simulations. When steady state is reached, the total shear stress must be a straight line to balance the pressure gradient and the following relation can be derived from the momentum equation for mean stream wise velocity:

$$\left\langle\sigma_{rz}^+\right\rangle = \left\langle u^+w^+\right\rangle - \frac{\partial w^+}{\partial r^+} = 2\frac{r^+}{Re_\tau} \tag{5.1}$$

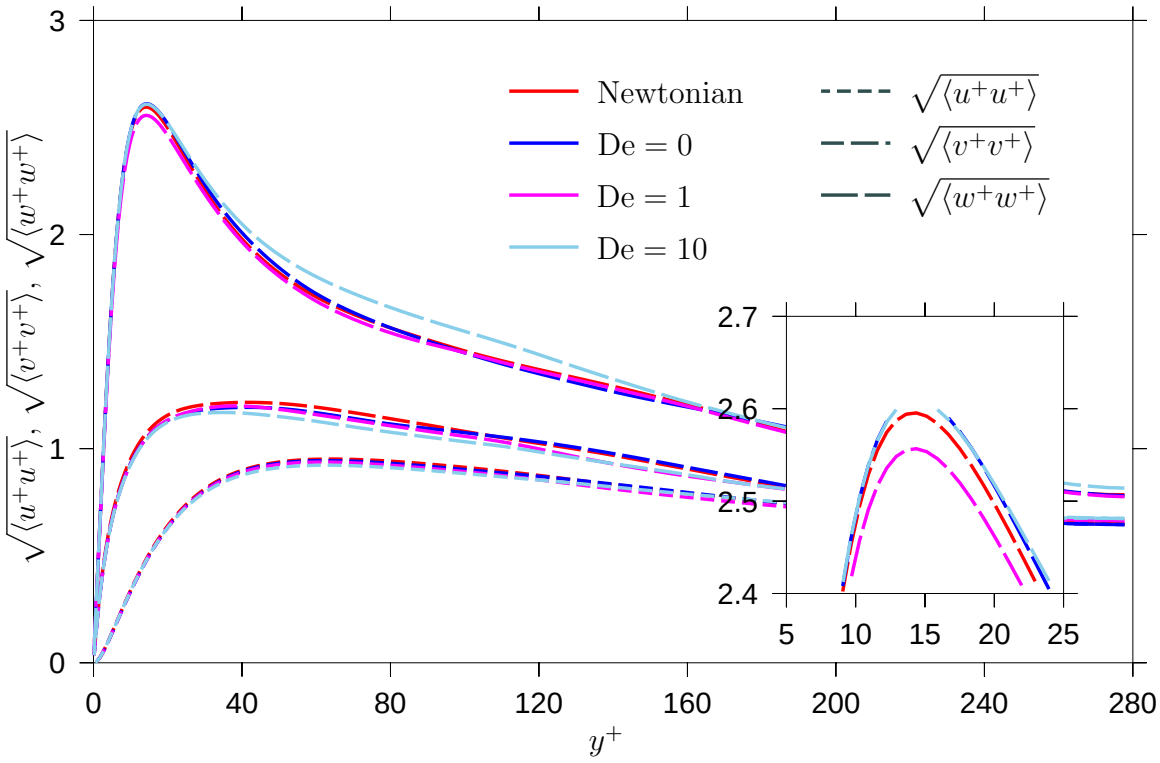

Figure 5.2 – Average r.m.s velocity profiles for the solvent.

It can be seen in figure 5.3 that this is indeed the case for the Newtonian profile. When drag reduction is occurring the amount of momentum transport to the wall my the solvent is reduced, resulting in a lower shear stress at the wall and thus a less steep slope for the total shear stress as function of the distance from the wall. This phenomenon is called the "Reynolds stress deficit" and is also observed for other drag reduced flows (Choi et al. 1994). The difference is made up for by the polymer stress tensor because the total wall shear stress still needs to be balanced with the pressure gradient, or Newtons second law would be violated.

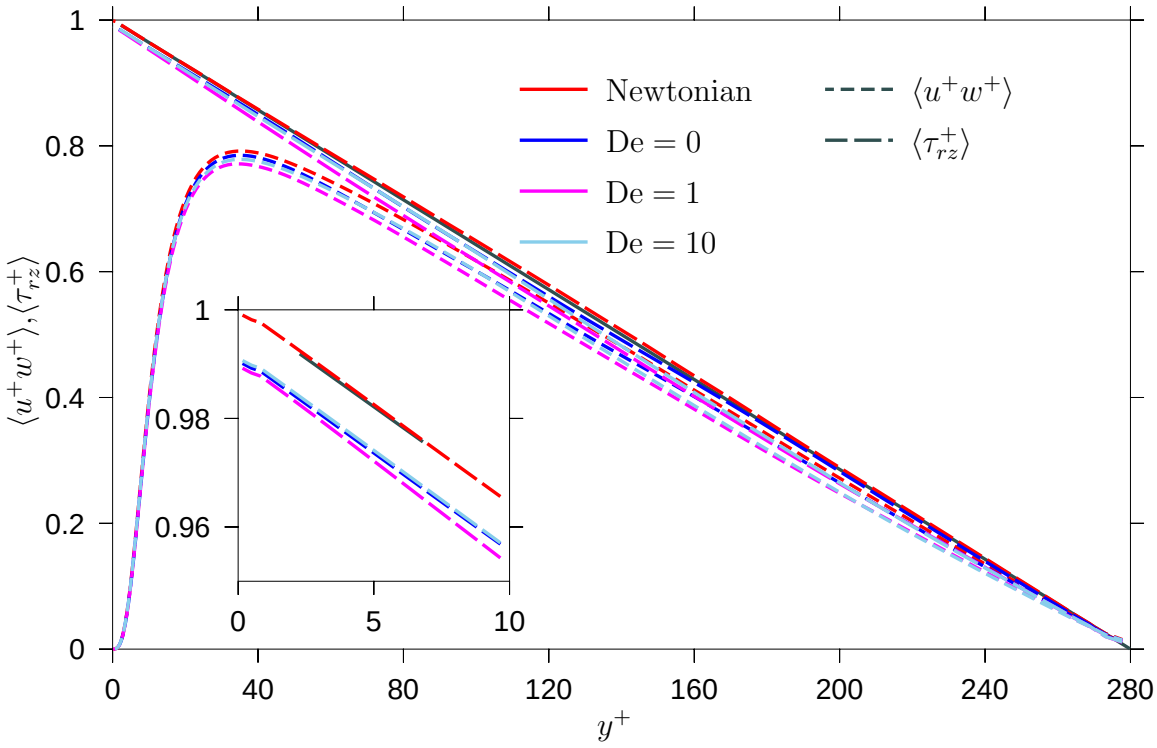

Figure 5.3 – Reynolds shear stress and total shear stress for the solvent.

5.2 Polymers

Figures 5.4 and 5.5 show the average velocities and the root-mean-square velocities of the polymer chains compared to the solvent velocities and root-mean-square velocities (i.e. Reynolds stresses) as function of the distance from the wall. As expected, due to the small particle relaxation time of the beads of the dumbbells, the polymer chains almost exactly track both the average velocity as well as the velocity fluctuations of the solvent. This opposed to heavier beads, which would show a clear lag for especially the velocity fluctuations (Boelens & Portela 2007). Another effect of the small particle relaxation times of the beads of the dumbbells can be seen in graph 5.6, which shows the relative concentration profile for the different Deborah numbers. Contradictory to the findings of Dimitropoulos et al. (2006) all simulations show a completely flat concentration profile. While for larger particle relaxation times there would be a higher concentration at the wall, the polymer beads have such a

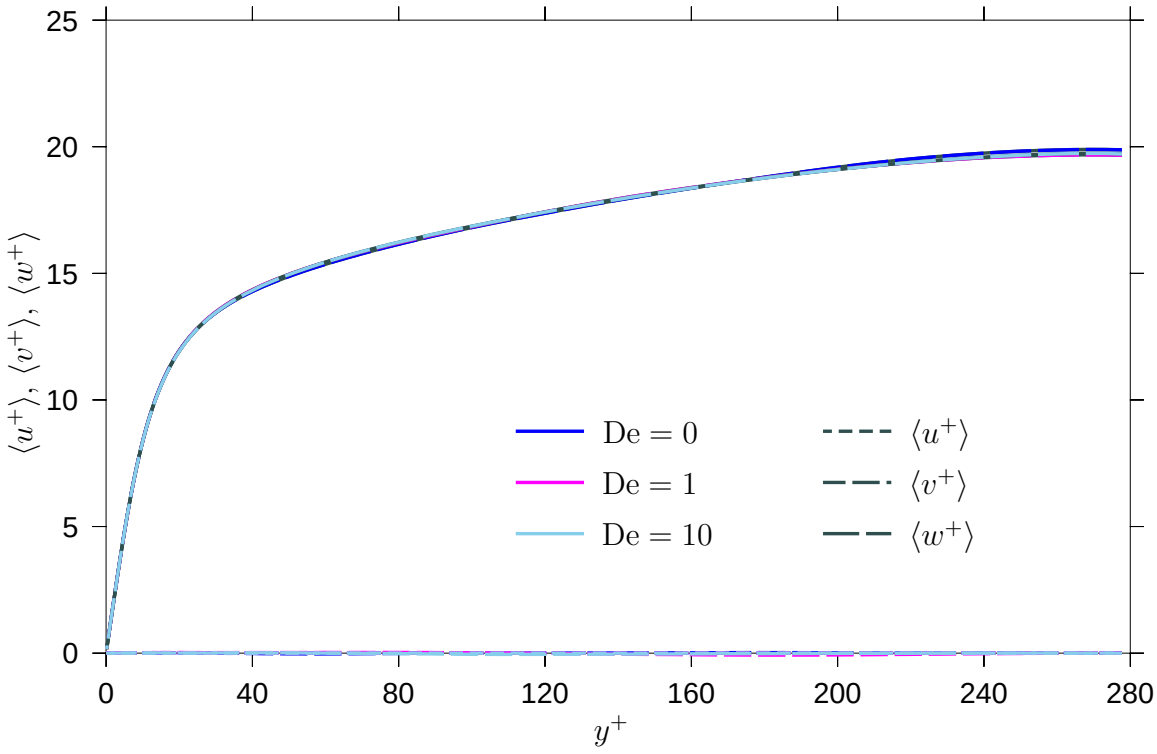

Figure 5.4 – Average mean velocity profiles for the polymers. Average polymer velocity profiles compared with the solvent velocity profiles in gray.

small relaxation time that this is prevented by Brownian motion (Davila & Hunt 2001). The fact that, because it is a continuum model, the FENE-P model used by Dimitropoulos et al. (2006) does not explicitly contain Brownian motion could explain why their model predicts a build up of polymer chains at the wall, while this is not found in the simulations presented here.

Figure 5.7 shows the average length of the end-to-end vector of all dumbbells normalized by their maximum extension. Because the molecular weight is kept constant between the different simulations, the maximum extension is 1 for all cases. However, because the equilibrium length is equal to the radius of gyration in wall units, it varies depending on the value of the Deborah number. For the infinite stiff spring, De = 0, the equilibrium and the maximum length are the same. For the other two cases the equilibrium length scales as:

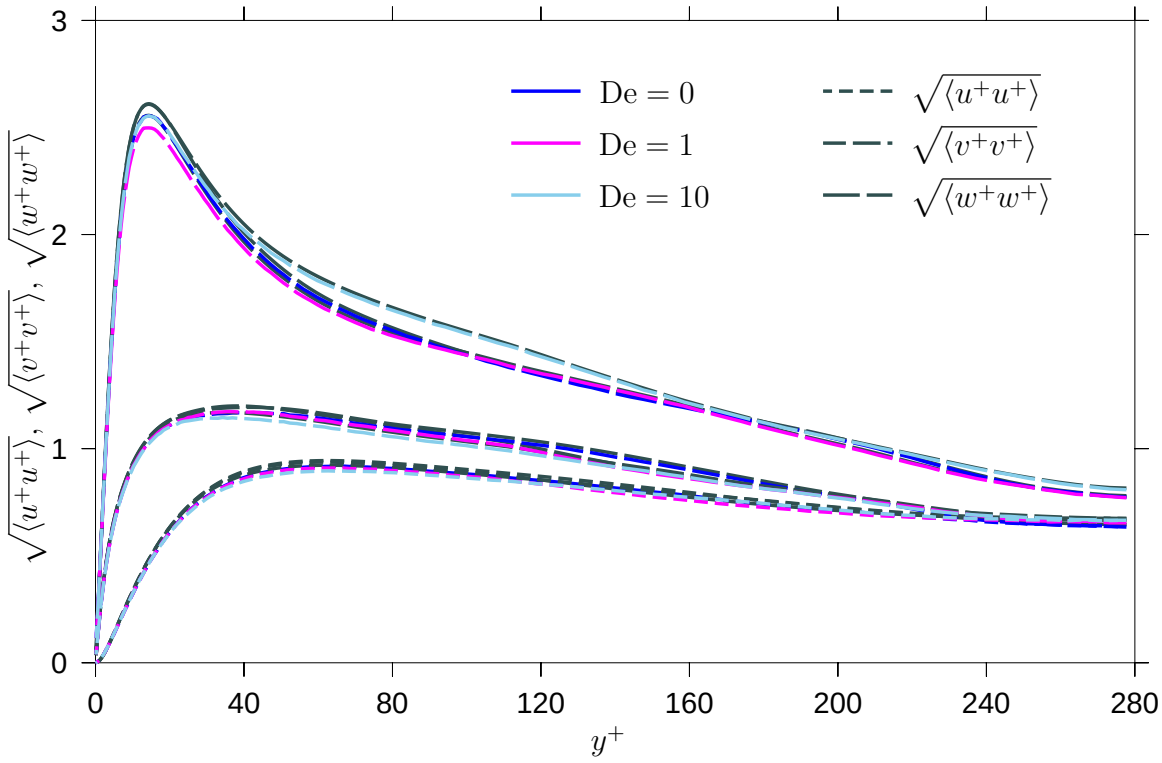

Figure 5.5 – Average r.m.s velocity profiles for the polymers. Average root-mean-square velocity profiles of the polymer chains compared to the solvent values.

$$R_g^+ \propto \mathrm{De}^{1/3} \tag{5.2}$$

as is derived in appendix B. For De = 0 it can be seen how the RATTLE algorithm correctly enforces the constraint of keeping the beads at fixed distance from each other. Because it represents the most flexible chain with the longest relaxation time, the dumbbell with a Deborah number of De = 10 gets stretched the furthest. Both flexible chains are stretched the most close to the wall where gradients are the largest, and relax towards the center of the pipe. However, on average they never return to their equilibrium conformation. In graph 5.8 the orientation of the polymer chains as function of distance from the wall is shown. The orientation is defined by two angles, the inclination θ, and the azimuth ϕ. The main axis of the spherical coordinate system in which these angles are defined is in the streamwise direction. The inclination is calculated with the formula:

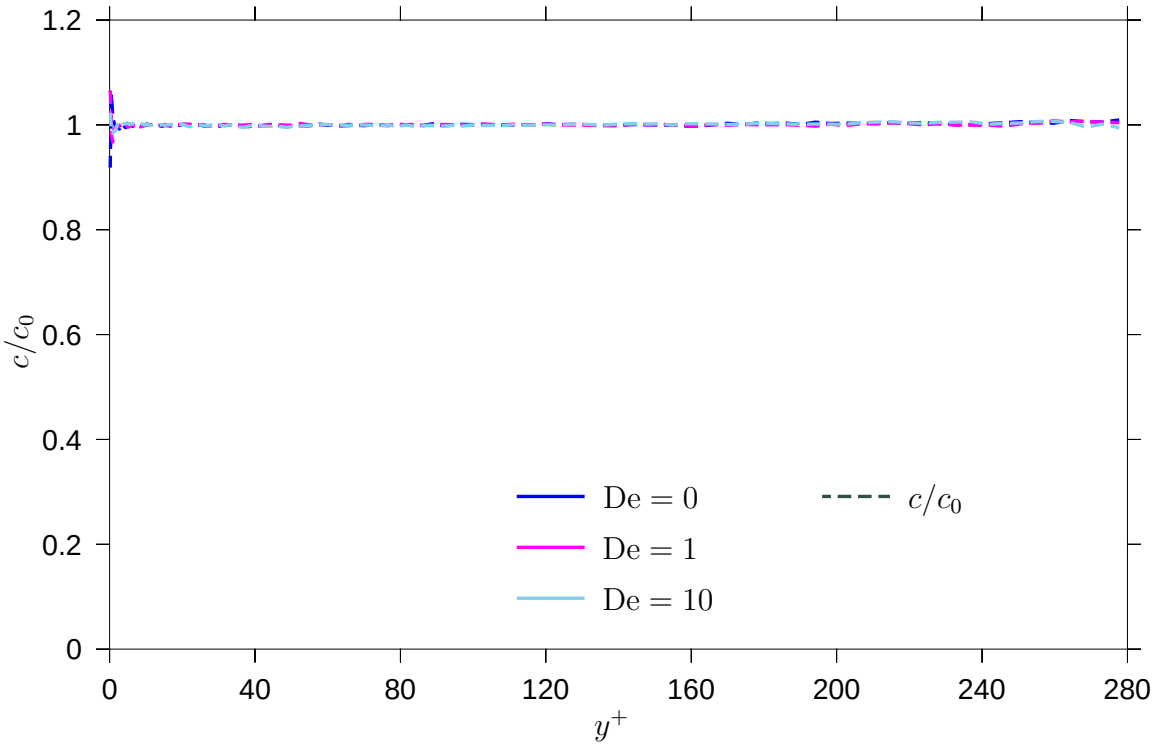

Figure 5.6 – Relative concentration profiles of the polymers.

$$\theta = \cos^{-1}\left(|z|/r\right) \tag{5.3}$$

where is absolute value is introduced because, since the polymer chains are homopolymers, there is no distinction between the front and the back of a chain. Without taking the absolute value, the average value of the inclination would simply be zero. The inclination ranges from $\theta = [0, \pi/2]$, where $\theta = 0$ means that a chain is completely aligned in the streamwise direction, and $\theta = \pi/2$ means that a chain is aligned in the radial direction. For random oriented chains the average inclination is $\langle\theta\rangle = \pi/4$. The azimuth ranges from $\phi = [-\pi, \pi]$ and for a set of random oriented chains its value is $\langle\phi\rangle = 0$. Looking at the average inclination, $\langle\theta\rangle$, The graphs show that, because of the high shear stresses, polymers orientate in streamwise direction at the wall. In the center, however, the orientation is close to random for all Deborah numbers. The average value of the azimuth $\langle\phi\rangle = 0$ shows that everywhere in the flow the polymer chains tumble freely around the axis in streamwise direction. Figure 5.9 shows

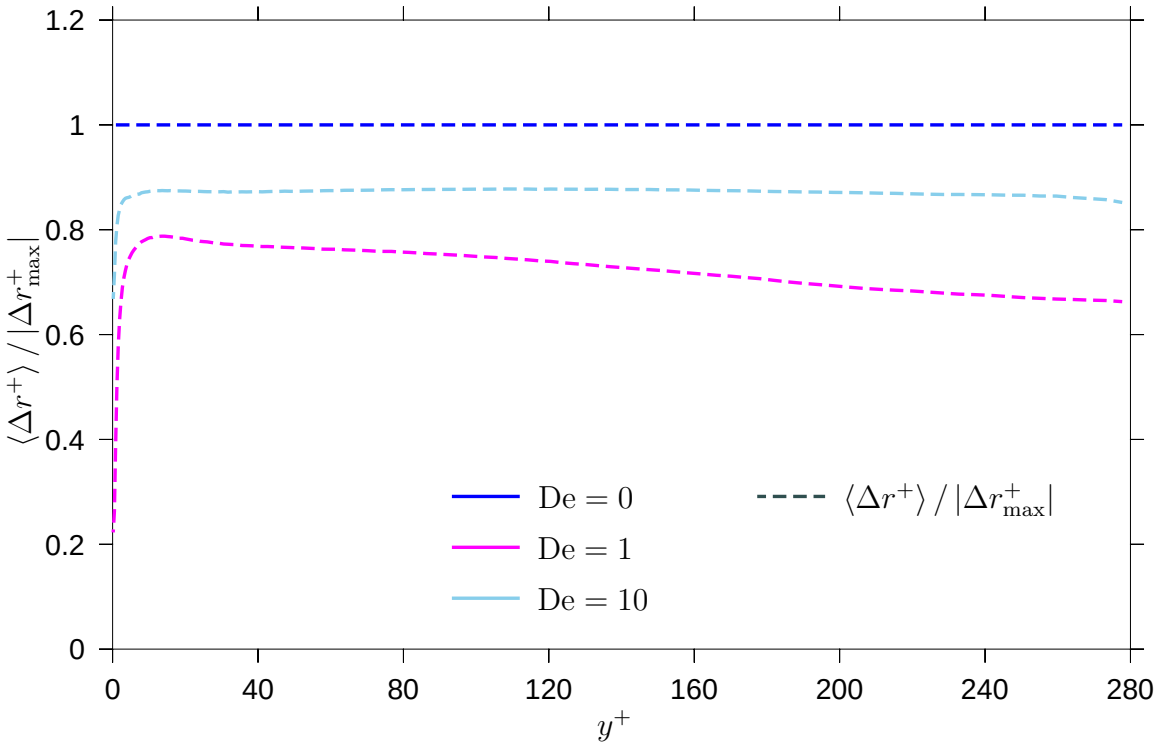

Figure 5.7 – Average relative length of the end-to-end vector. Average relative length of the end-to-end vector of the polymer chains.

the inner product of the velocity difference of the two beads with the normalized end-to-end vector. This physically represents the relative velocity between the two beads of a dumbbell along the connecting vector. Since it is one of the constrains of the RATTLE algorithm this velocity should be close to zero for the simulation with De = 0, which is indeed the case. The other two runs confirm that polymer chains are suddenly stretched at the wall but gradually relax, giving an on average positive velocity difference between beads at the wall.

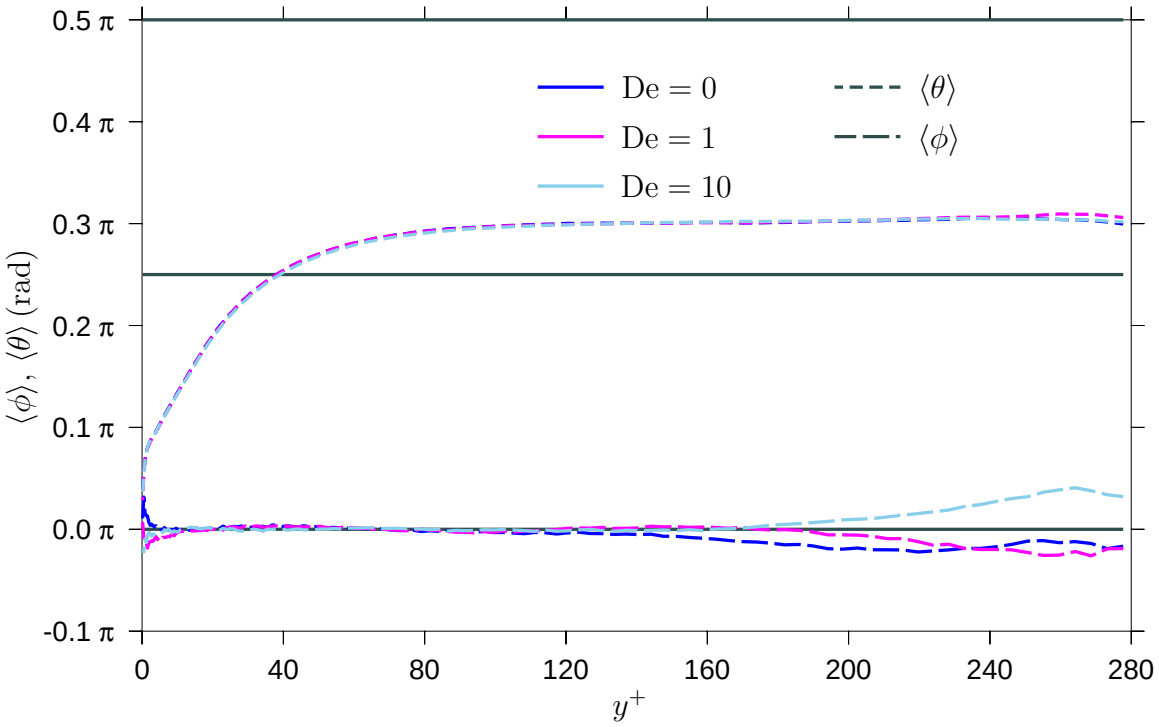

Figure 5.8 – **Average orientation of the end-to-end vector.** Average orientation of the end-to-end vector of the polymer chains. The zenith direction is the streamwise direction.

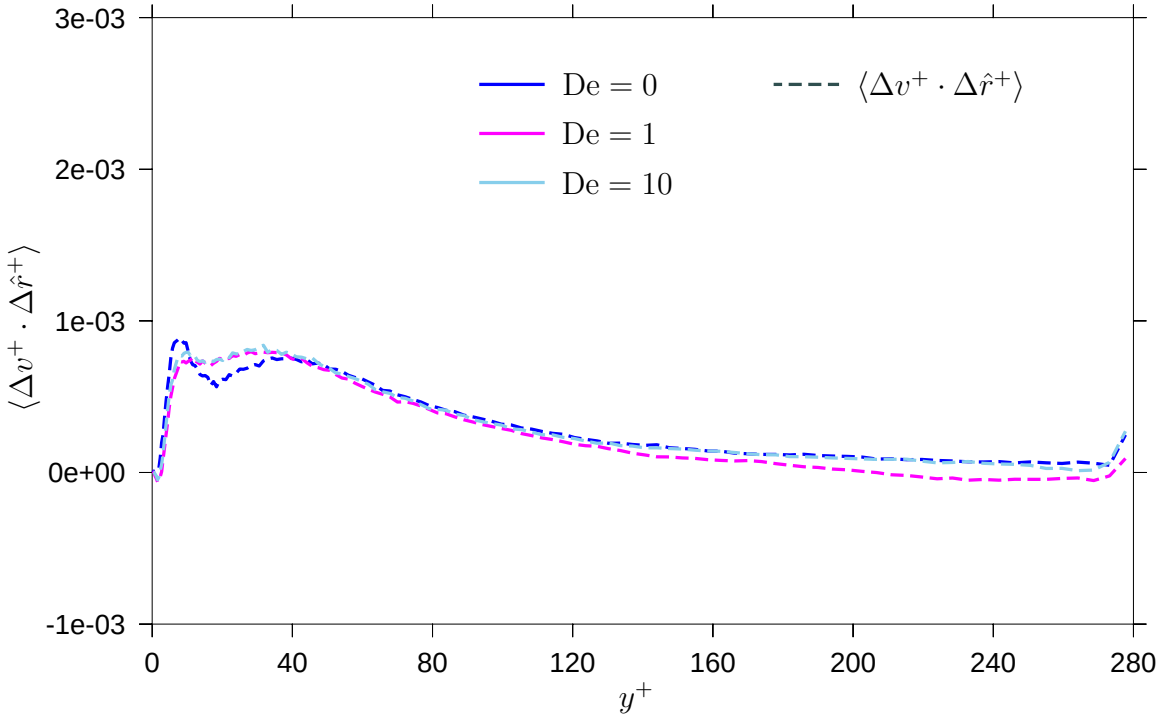

Figure 5.9 – **Average value of the relative velocity between beads.** Average value of the relative velocity between beads on the same chain.

5.3 Interaction

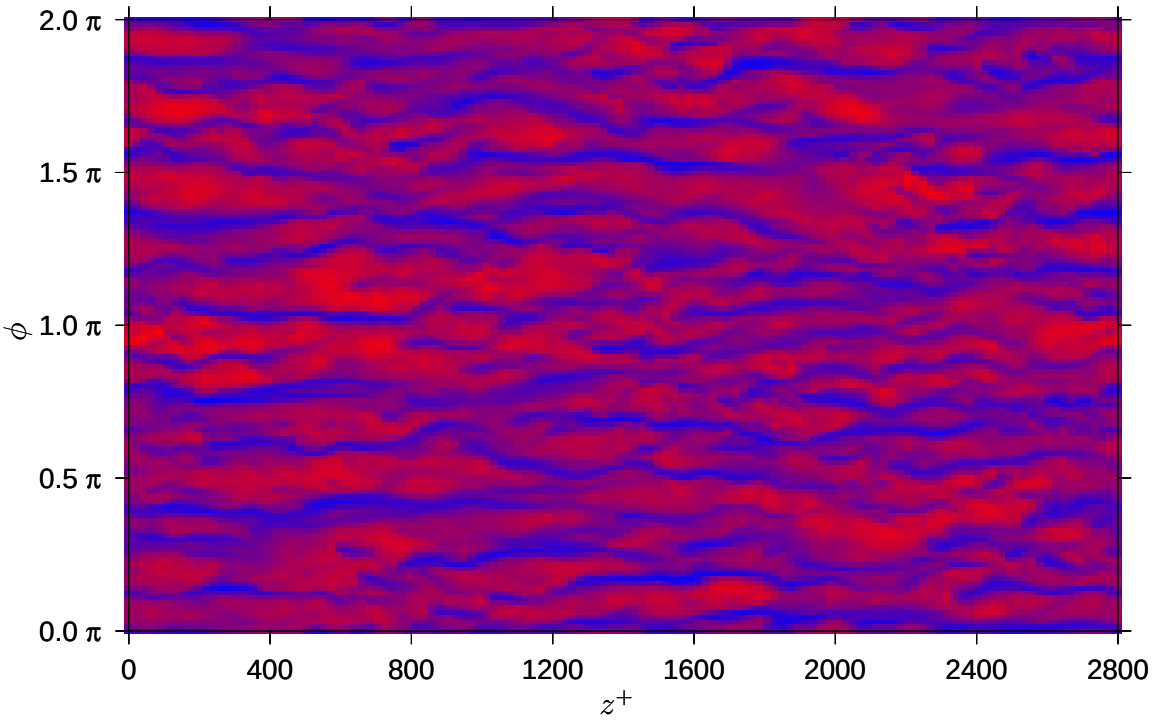

Figure 5.10 – Iso plot of the streamwise velocity for Newtonian flow. Iso plot of the streamwise velocity at $y^+ = 20$ wall units away from the wall for Newtonian flow.

With the previous two sections focussing on the solvent and the polymer phase individually, this section looks at the interaction between the two. As mentioned in the literature section drag reduction has been associated with streak stabilization. In the figures 5.10 and 5.11 two iso plots are shown of the streamwise velocity at a distance $y^+ = 20$ from the wall with the color blue indicating a low velocity streaks and red high velocity streaks. While for highly drag reduced flows using continuum modeling streaks have been observed to become straighter and wider (De Angelis et al. 2002), this can not be observed in the graphs presented here. However, figure 5.12 shows the auto correlation function of the streamwise velocity component on the streamwise direction and indeed a small difference in the correlation length can be observed. The longer correlation lengths for the drag reduced flow simulations suggest

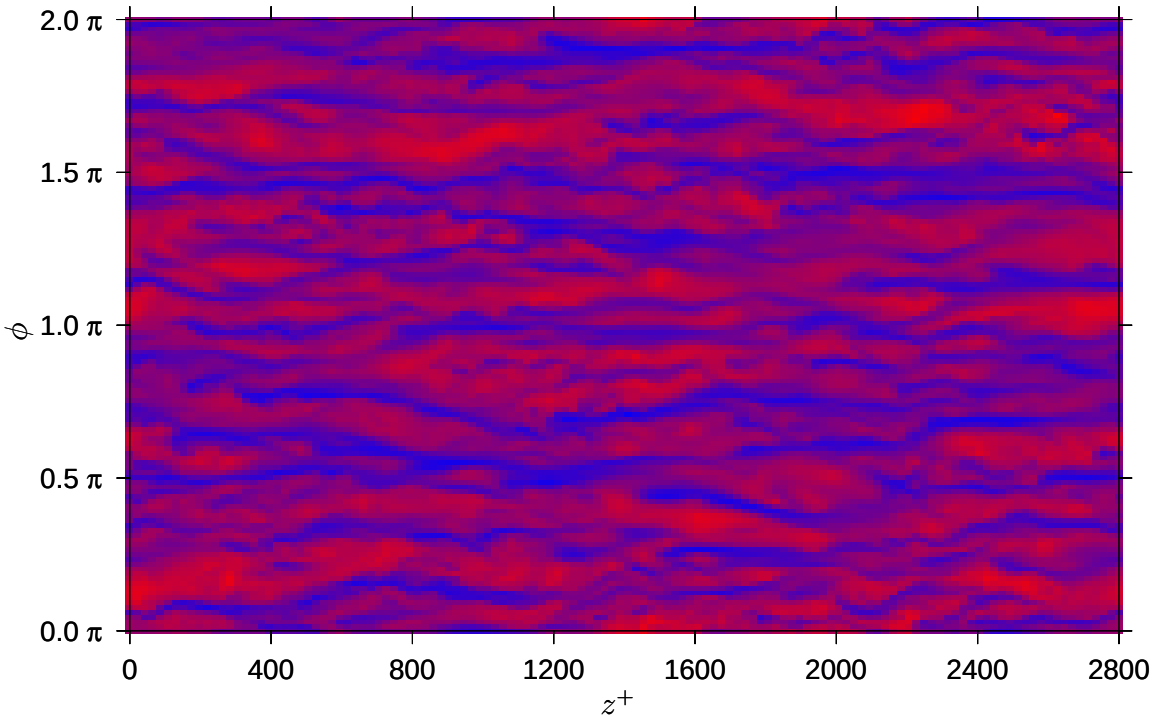

Figure 5.11 – Iso plot of the streamwise velocity for De = 0. Iso plot of the streamwise velocity at $y^+ = 20$ wall units away from the wall for De = 0.

that the streaks are indeed straighter and wiggle less and thus that the polymers and fibers have a stabilizing effect.

Now it has been confirmed that there is a correlation between drag reduction by polymers and streak stabilization, it is now time to take a closer look at the interaction between polymers and streaks. Graphs 5.13 and 5.14 show the different components of the polymer stress tensor calculated with the Kramers-Kirkwood equation (Kramers 1944):

$$\sigma_2^+ = -\frac{n_2}{V^+} \left\langle \Delta \mathbf{r}^+ \Delta \mathbf{F}^{h^+} \right\rangle \tag{5.4}$$

where n_2 is the number of polymer chains in volume V^+, $\Delta \mathbf{r}^+ = 1/2 \left(r_1^+ - r_2^+ \right)$ is half the end-to-end vector, $\Delta \mathbf{F}^{h^+} = \mathbf{F}_1^{h^+} - \mathbf{F}_2^{h^+}$ is the difference between the hydrodynamic force on each bead of the dumbbell, and $\langle\rangle$ denotes a conformational average. This formula is valid for both the flexible as well as the rigid dumbbells (Bird & Curtiss 1985). In both graphs a strong similarity to the corresponding components of the

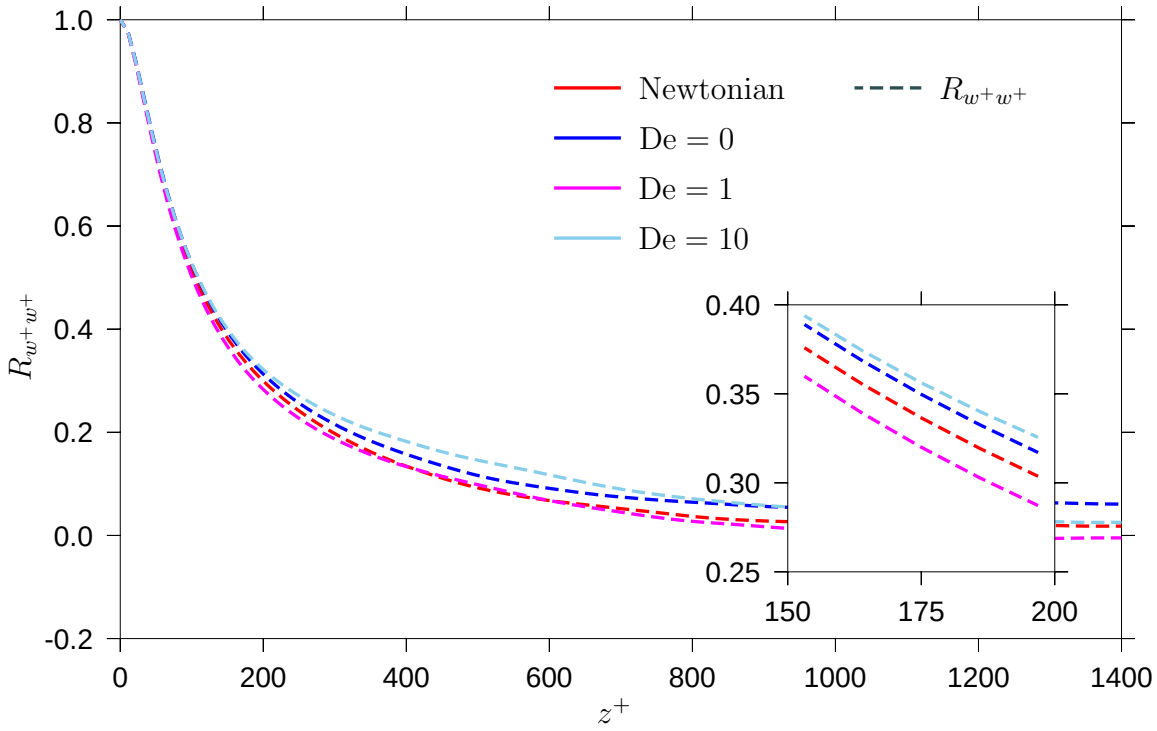

Figure 5.12 – Autocorrelation function of the streamwise velocity. Autocorrelation function of the streamwise velocity at $y^+ = 20$ wall units away from the wall.

Reynolds stresses can be seen, where in graph 5.13 the stresses have the opposite sign and in 5.14 they have the same sign. Also, the diagonal components are larger than the off-diagonal components. By analyzing this stress tensor two kinds of polymer-solvent interactions can be observed which are depicted in figures 5.18 and 5.19. Figure 5.19 shows a polymer stretching due to encountering a velocity gradient along its end-to-end vector, $\mathbf{r}_1 - \mathbf{r}_2$. Since the hydrodynamic forces and the end-to-end vector are tangential, this contribution is responsible for the diagonal components of the stress tensor. The fact that all the diagonal components are negative, means that on average the solvent exerts a stretching force on the polymers and the solvent is subject to negative work by the polymers.

Figure 5.18 illustrates what kind of polymer-solvent interaction is responsible for the off-diagonal components of the polymer stress tensor. All off-diagonal components turn out to be zero, except the $\sigma^+_{2,rz}$ and $\sigma^+_{2,zr}$ components. This is equivalent to the

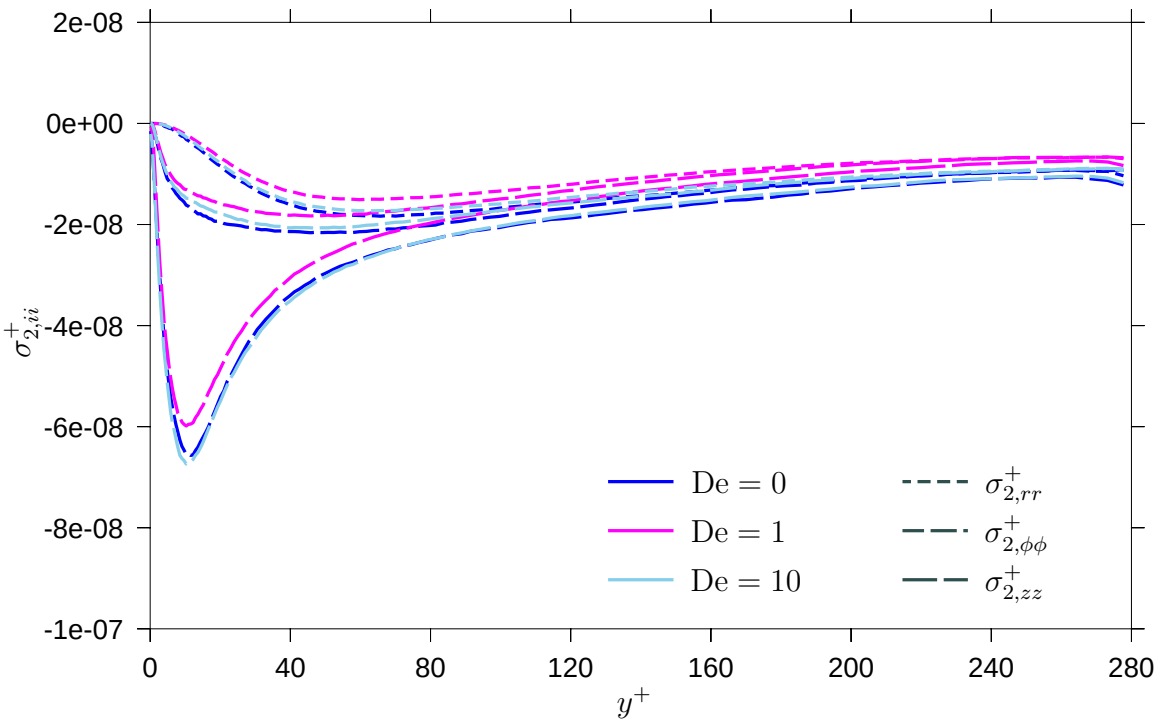

Figure 5.13 – Diagonal components of the polymer stress tensor.

solvent exerting a torque on the polymers trying to orientate them, and the polymers exerting a torque back on the solvent. The positive sign of the $\sigma^+_{2,rz}$ stress tensor component suggests that the orientation in the direction show in the illustration is dominant, with the direction of flow being in the z direction. With these two contributions to the stress tensor having been identified, the next question is which one of these two is responsible for the drag reducing effect of polymers and fibers.

When there is drag reduction, the pressure gradient over the pipe still needs to balance the total wall shear stress:

$$\left\langle \sigma^+_{rz} \right\rangle = \left\langle u^+ w^+ \right\rangle - \frac{\partial w^+}{\partial r^+} + \left\langle \sigma^+_{2,rz} \right\rangle = 2\frac{r^+}{Re_\tau} \tag{5.5}$$

When any form of drag reduction occurs, there is an increased velocity gradient $\partial w_1^+/\partial r^+$ and the Reynolds stress component $\left\langle u_1^+ w_1^+ \right\rangle$ is suppressed, resulting in the so called "Reynolds stress deficit" (White & Mungal 2008). This is compensated for by

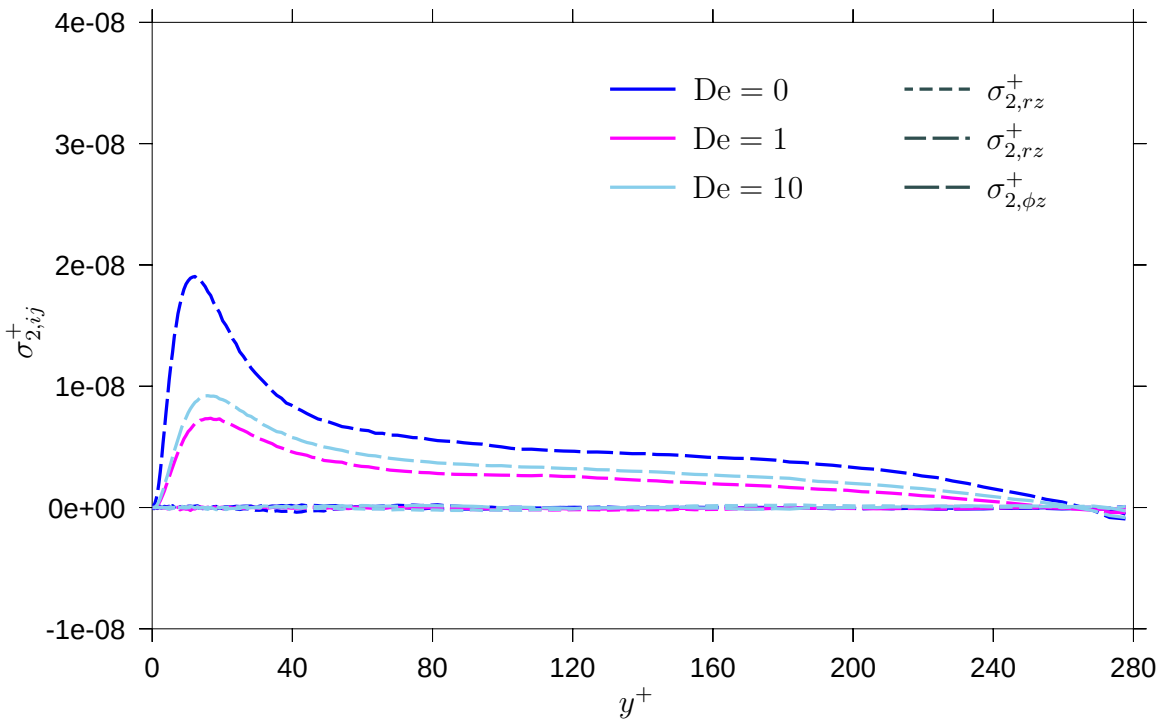

Figure 5.14 – Off-diagonal components of the polymer stress tensor.

an extra stress contribution from the drag reducing mechanism, because independent of the kind of flow, Newton's second law still needs to be obeyed. This extra stress contribution happen to be the $\langle \sigma^+_{2,rz} \rangle$ component of the polymer stress tensor, which is caused by the polymers resisting orientation by the solvent and exerting a torque. This suggest that the characteristic property of polymers for having a drag reducing effect is their ability to exert a torque on the solvent, instead of their elastic properties. The stretching contribution is important, because by stretching the moment arm of polymers is increased, but is not strictly necessary. This hypothesis is confirmed by the simulation with a Deborah number De = 0. In this simulation the spring connecting the two beads of the dumbbells is infinitely stiff and thus is not able to store any potential energy in its backbone. The results can be seen in the above figures and indeed, the simulations with De = 0 show even stronger drag reduction than the flexible polymers, because, fibers are always-fully-stretched polymers and

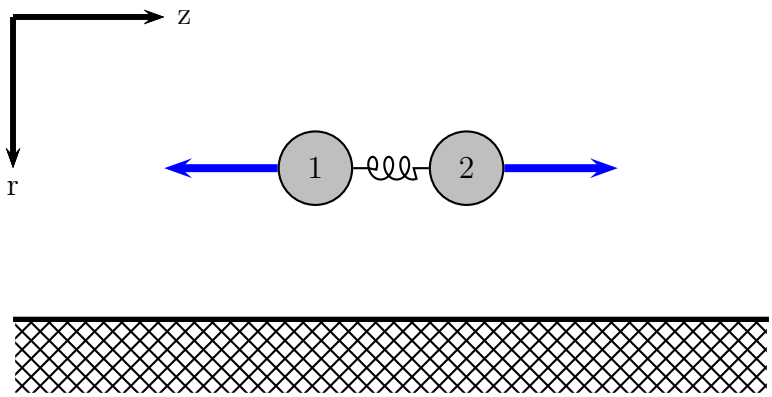

Figure 5.15 – Schematic representation stretched dumbbell. A schematic representation of a dumbbell being stretched by the solvent and exerting negative work back on the solvent.

have the largest moment arm. This also implies that instead of the Zimm relaxation time, which is undefined for fibers anyway, a better time scale would probably be the rotational relaxation time. For rod-like molecules this time scale is defined by Kirkwood & Auer (1951) (see also Muthukumar & Edwards (1983)), and for polymers it is proportional to the Zimm relaxation time. The importance of torque in drag reduction is also confirmed by Kim et al. (2008), who found that polymers exerting "counter-torque" cause suppression of the formation of hairpin vortices at the wall.

The shape of the stress component suggests that the polymers have the effect of an extra effective viscosity which increases with the distance from the wall, as was first suggested by De Angelis et al. (2004). This is illustrated in figure 5.17 which shows what the off-diagonal polymer stress terms would look like if the following viscosity profile is chosen:

$$\nu_2^+ = \begin{cases} 0.04\ y^+ & \text{if } y^+ < 150 \\ 6.0 & \text{if } y^+ \geq 150 \end{cases} \tag{5.6}$$

combined with the average rate of shear tensor of the Newtonian flow simulation. The shape of all the off-diagonal components is the same as the polymer stress components calculated with the kramers-Kirkwood equation. However, since the diagonal

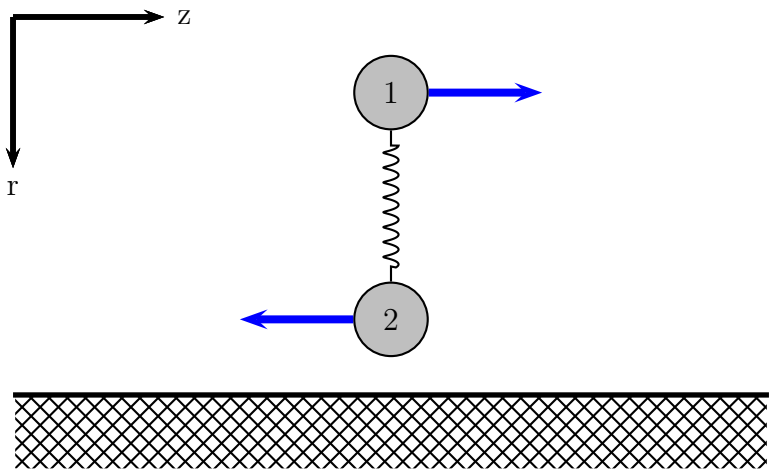

Figure 5.16 – Schematic representation oriented dumbbell. A schematic representation of a dumbbell being oriented by the solvent and exerting a torque back on solvent.

components of the average rate of shear tensor are all zero, the model suggested by De Angelis et al. (2004) would predict zero diagonal components for the polymer stress tensor, and this is not the case. This implies that the mechanism for drag reduction observed in a flow with an increasing viscosity profile is not necessarily the same as the mechanism causing drag reduction due to polymer additive. Nevertheless, using an increasing effective viscosity might be useful in, for example, RANS modeling of drag reduction.

To get more insight into the average torques and compression acting on the solvent, the next graphs take a look at the average absolute torque the stretch forces acting along the end-to-end vector. The torque on the solvent is defined as:

$$\tau_2^+ = -\frac{n_2}{V^+}\left\langle \Delta\mathbf{r}^+ \times \Delta\mathbf{F}^{h+} \right\rangle \tag{5.7}$$

where again n_2 is the number of polymer chains in volume V^+, $\Delta\mathbf{r}^+ = 1/2\left(\mathbf{r}_1^+ - \mathbf{r}_2^+\right)$ is half the end-to-end vector, $\Delta\mathbf{F}^{h+} = \mathbf{F}_1^{h+} - \mathbf{F}_2^{h+}$ is the difference between the hydrodynamic force on each bead of the dumbbell, and $\langle\rangle$ denotes a conformational

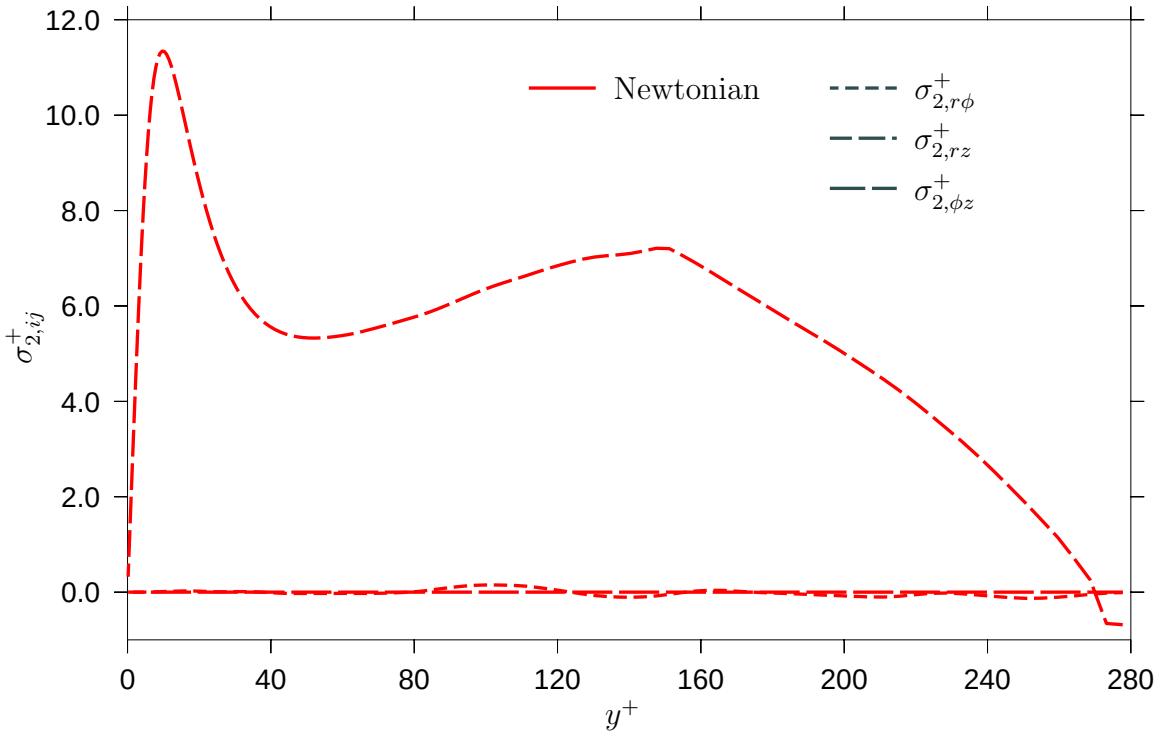

Figure 5.17 – Off-diagonal polymer stress components due to effective viscosity. Off-diagonal polymer stress components resulting from a viscosity profile which increases linearly with the distance away from the wall as suggested by De Angelis et al. (2004).

average. However with this definition left and right turning polymer chains would cancel each other out for the torques in radial and streamwise direction, so in graph 5.18 the absolute value of the torque is shown for each direction. It can be seen how in the bulk the polymer chains randomly tumble around resulting in the absolute torque having the same value in every direction. However toward the wall, because of the orientation of the chains, the torque in the z direction significantly decreases while the torque in the radial direction increase. This is because the orientation results in a smaller moment arm for the torque in the streamwise direction while it gives a larger moment arm for the radial direction. Also an increase of the absolute torque in the angular direction can be seen, the component responsible for balancing the Reynolds stress deficit. The stretch is defined as:

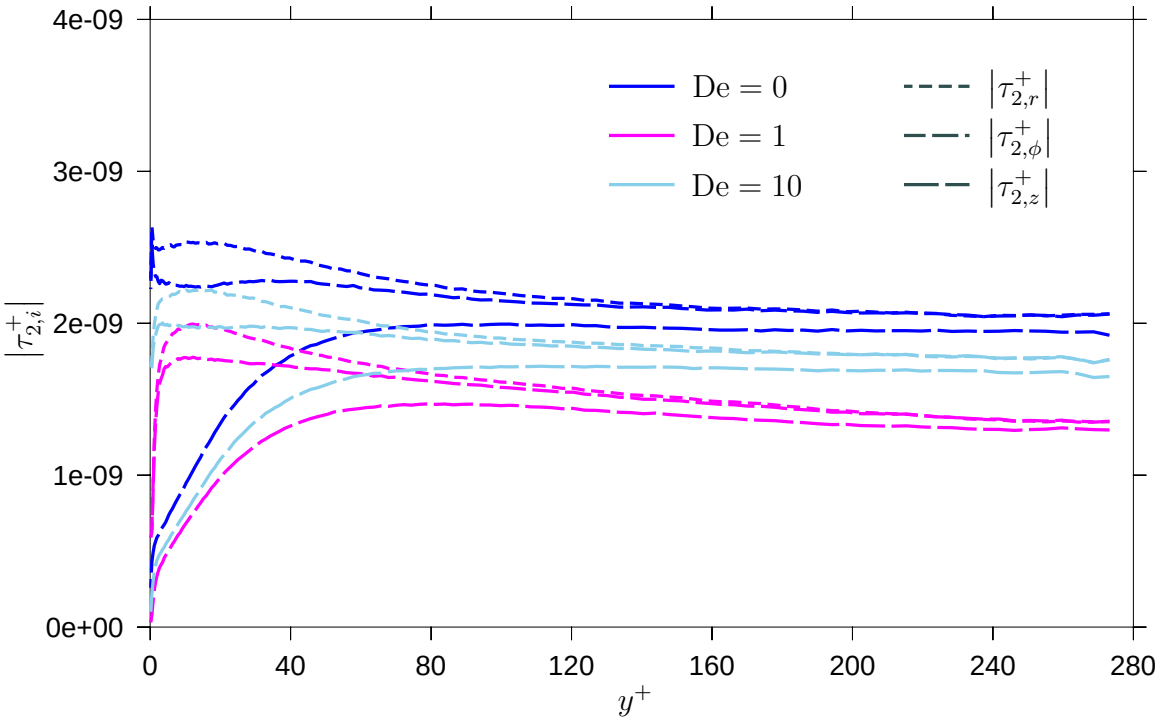

Figure 5.18 – Absolute value of the polymer torque. Absolute value of the torque exerted by the polymer chains on the solvent.

$$\upsilon_2^+ = -\frac{n_2}{V^+}\left\langle \Delta\mathbf{r}^+ \cdot \Delta\mathbf{F}^{h+} \right\rangle \tag{5.8}$$

where the end-to-end vector $\Delta\mathbf{r}^+$ is not normalized to be able to compare this contribution to the torque vector and the stress tensor. Looking at the scaling on the y-axis is can be seen that average stretch contribution is more than an order larger than the absolute average torque. Also, as predicted based on the stress tensor the stretch contribution is actually a contraction and negative work is performed on the solvent by the polymer chains. Physically this corresponds to a polymer encountering a velocity gradient tangential to its end-to-end vector and working against it. The polymer stretches and forces two points in the direction of the velocity gradient to have the same velocity. Also in the case of a polymer the stretching of the polymer makes sure that there is enough of a moment arm to create the torque needed to drag reduction. For fibers the negative work on the solvent probably helps dampening

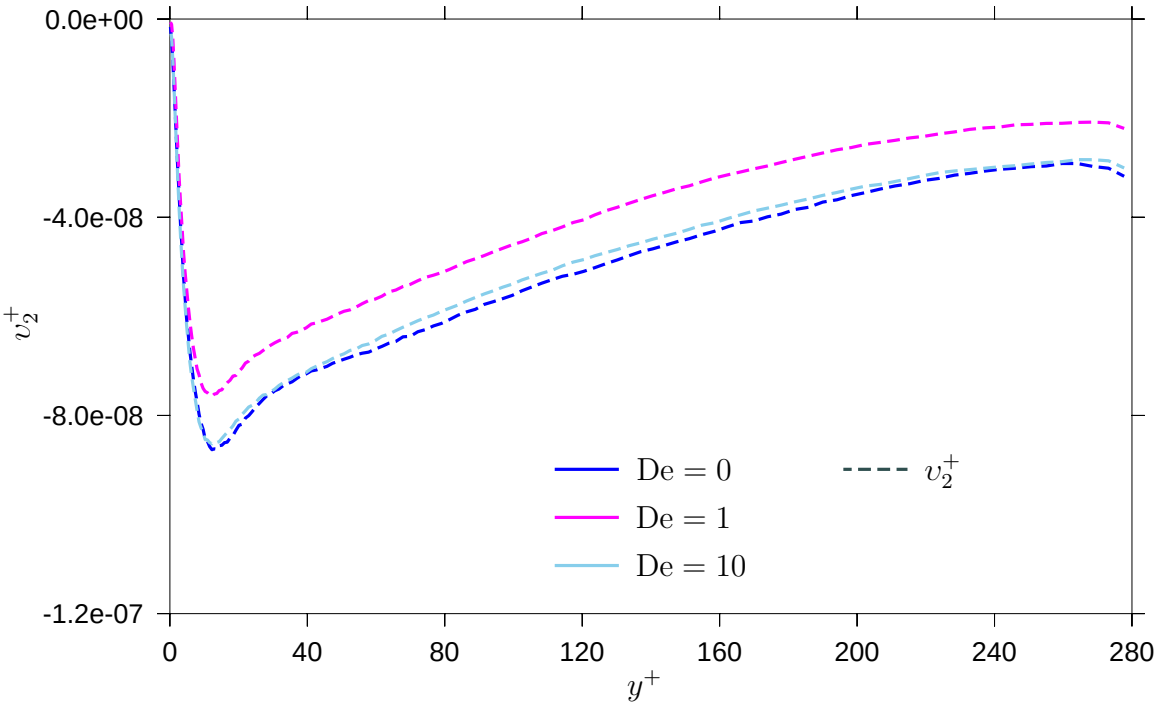

Figure 5.19 – Expansion and compression forces of polymers. Expansion and compression forces exerted by the polymers on the solvent.

instabilities and thus enhances the orientation of fibers at the wall, but is not strictly necessary to have drag reduction.

The last two graphs 5.20 and 5.21 address the questions where the torque and contraction are acting on the solvent. Both graphs show the iso streamwise velocity graph show in figure 5.11, but this time with the positions of maximum torque and stretch imposed on top as white dots. Although this only gives a qualitative idea of what determines there interaction between the polymers and solvent takes place it gives some insight nevertheless. It has been suggested that vortices close to the wall are dominant in polymer-solvent interactions (Dubief et al. 2005). However, splitting up the interactions in compression and torque, it would be expected that compression acts in regions with high velocity gradients and torque in regions with high vorticity. Because of the nature of streaks being alternating region of high and low streamwise velocity, the higher velocity gradients can be found on the interface between these

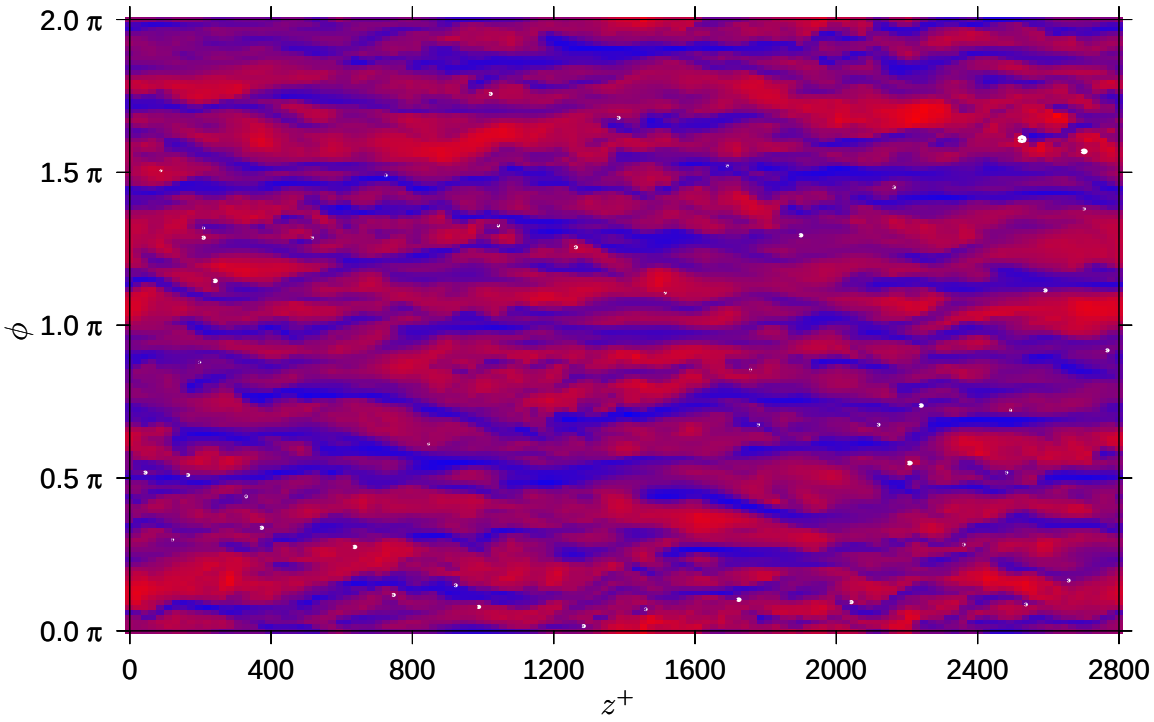

Figure 5.20 – Contour plot of maximum torque for De = 0. Contour plot of the maximum angular torque superimposed on an iso plot of the streamwise velocity at $y^+ = 20$ wall units away from the wall for De = 0.

regions. In figure 5.21 can be seen that most white dots can indeed be found in the on the interface between these blue and red colored regions. Polymers exerting torque can also be found in the middle of the low and high speed regions, but still mostly act on the interface.

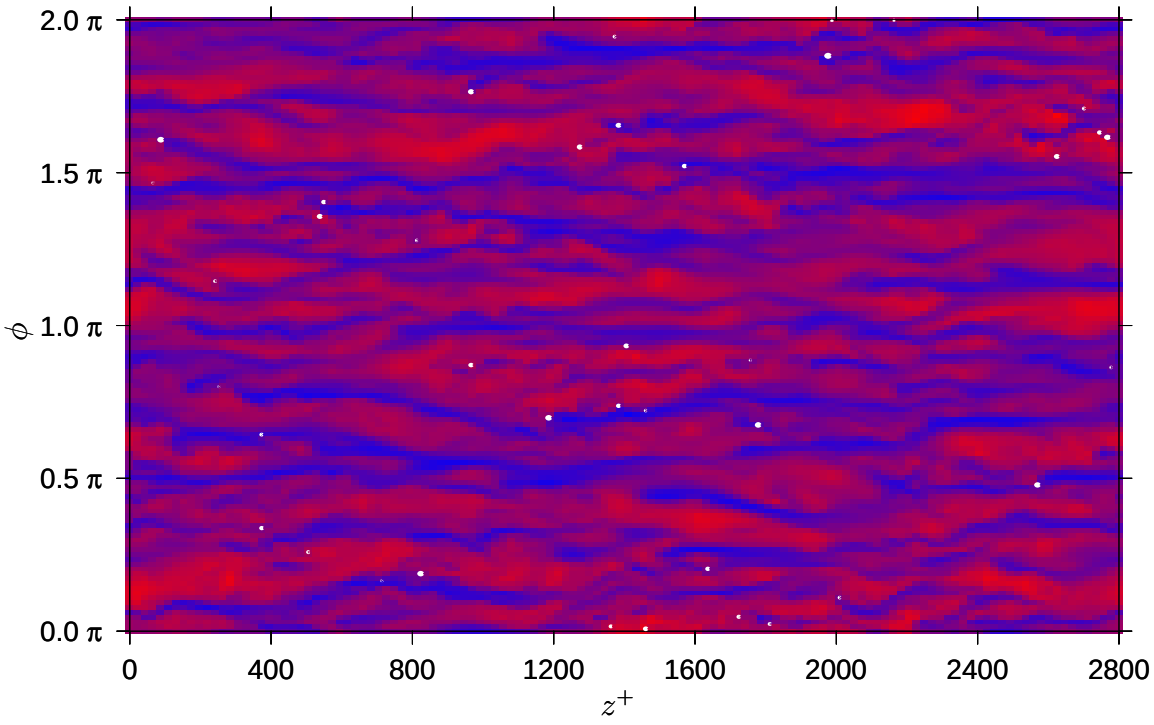

Figure 5.21 – **Contour plot of maximum stretch for De = 0.** Contour plot of the maximum stretch superimposed on an iso plot of the streamwise velocity at $y^+ = 20$ wall units away from the wall for De = 0.

CHAPTER 6

CONCLUSIONS

Simulations were performed for turbulent pipe flow at a friction Reynolds number of $\mathrm{Re}_\tau = 560$ on a grid of $128 \times 256 \times 256$ with 960.000 dumbbells of Deborah numbers $\mathrm{De} = 0$, $\mathrm{De} = 1$, and, $\mathrm{De} = 10$. Drag reduction is observed through reduced Reynolds stresses, the Reynolds stress deficit, and a rz polymer stress tensor component to balance the Reynolds stress deficit. It can be concluded that drag reduction can be observed using only first principles, that is using a hybrid D.N.S. with Langevin dynamics approach.

Streak stabilization can not be seen by visual inspection of the iso streamwise velocity at $y^+ = 20$ wall units away from the wall, but an increase in the correlation length of the streamwise velocity can be seen, indicating that there is indeed a correlation between drag reduction due to polymers and streak stabilization. Streak stabilization could also explain the phenomenon of the Maximum Drag Reduction (M.D.R.) asymptote. As drag reduction becomes stronger and stronger, it is possible that there is eventually a state in which the streaks do not wander around along the wall anymore and are completely stabilized. At this point it would not be possible to get more drag reduction and M.D.R. is reached.

Polymer solvent interaction takes place trough two different contributions. For a polymer or fiber to be able to have a drag reducing effect, it needs to be able to perform a torque on the solvent in the spanwise or angular direction by orientating in the streamwise direction. This torque is responsible for generating a positive rz stress component which causes a reduction of the rz Reynolds stress component,

and thus reduces the flux of momentum towards the wall. In addition to the torque there is compression contribution on the solvent which in the case of polymers is responsible for stretching them. It is this stretching contribution which makes sure the polymers have a large enough moment arm to exert the torque on the solvent which cause drag reduction. For the polymers with the Deborah number $\mathrm{De} = 0$ (i.e. fibers) this contribution is probably not necessary because they are fully stretched already. However, it would be interesting to validate this in future work by switching off the stretching contribution completely and see whether the same amount of drag reduction is still occuring. Another interesting topic for follow-up research would be whether the rotational orientation time is actually the correct time scale and how the amount of drag reduction varies with it. Although Lumley (1969) his analysis of length and time scales was for polymers in isotropic homogeneous turbulence, there still needs to be a time scale that describes solvent-polymer/fiber interaction. While for flexible polymers their rotational relaxation time is proportional to their Zimm relaxation time, for fibers this would mean a new onset criterion. It is expected that for very small rotational relaxation times fibers and polymers have an immediate response to the solvent's changing vorticity, and thus will not have a drag reducing effect. On the other hand, too large a rotational relaxation time might imply an also large "particle" relaxation time which might result in increased drag.

Last but not least there is the effect of concentration. Because of the form of the Kramers-Kirkwood equation and the fact that, due to brownian motion, the concentration profile is completely flat, the polymer stress tensor would increase linearly with increased polymer concentration. However, there is no guaranty that the respons of the coherent structures (e.g. streaks and vortices) in the boundary layer is independent of polymer concentration, which could explain the $\propto c$ correlation found by Virk (1975). In the limit for high concentration every polymer added will have a less drag reducing effect than the previous polymer till the Maximum Drag Reduction

asymptote is reached, where there is no dependence on concentration anymore. For the low concentration limit, initially the stress excerted by polymers on the solvent will grow linearly with the concentration. For example, adding two polymers instead of one will make the number density twice as large, but will not have any influence on the hydrodynamic forces because the concentration is too low to modify any coherent structure. This means the stress tensor will simply become twice as large. For higher concentrations it is possible that there is a positive feedback loop in the sense that modified coherent structures cause more efficient orientating of newly added polymers. This would lead to the perceived observation of a critical onset concentration.

APPENDIX A

PRANDTL - KÁRMÁN PLOTS

A lot of experimental data is presented in the form of Prandtl - Kármán plots, where $1/\sqrt{f}$ is plotted as a function of $\mathrm{Re}\sqrt{f}$, with Re being the bulk Reynolds number, and f being either the fanning friction factor:

$$f_F = \frac{R}{L}\frac{\Delta p}{\rho \bar{u}^2} \tag{A.1}$$

or the Darcy friction factor:

$$f_D = 4\frac{R}{L}\frac{\Delta p}{\rho \bar{u}^2} \tag{A.2}$$

Here Δp is the pressure drop over length L, R is the radius of the pipe, ρ is the density of the liquid, and $\bar{u}$ is the average bulk velocity.

Using the definition of the friction velocity u_τ:

$$\rho u_\tau^2 = \tau_w \tag{A.3}$$

where τ_w is the shear at the wall, and the following force balance, which is valid for pipe flow:

$$\Delta p \pi R^2 = \tau_w 2\pi R L \tag{A.4}$$

it can be derived that:

$$\frac{1}{\sqrt{f_F}} = \frac{\bar{u}^+}{\sqrt{2}} \tag{A.5}$$

and:

$$\mathrm{Re}\sqrt{f_F} = \sqrt{2}\mathrm{Re}_\tau \tag{A.6}$$

or for the Darcy friction factor:

$$\sqrt{\frac{2}{f_D}} = \frac{\bar{u}^+}{2} \tag{A.7}$$

and:

$$\mathrm{Re}\sqrt{f_D} = 2\sqrt{2}\mathrm{Re}_\tau \tag{A.8}$$

where $\bar{u}^+$ is the average bulk velocity in wall units, and Re_τ is the friction Reynolds number.

APPENDIX B

DENSITY AND DIAMETER RATIOS

To map a bead chain system to an actual polymer molecule, the following properties need to be preserved:

- The diffusion coefficient of the bead spring model needs to match the diffusion as calculated by the Zimm model.
- The Deborah number matches the Zimm relaxation time in wall units.
- The mass of the bead spring model needs to be the same of weight one molecule.

Again, for implicitly, it is assumed here that the polymer chain is modeled by a dumbbell. Lets first find an expression for $\rho^* = \rho_1/\rho_2$. Since the density of the solvent is know, this means an expression for ρ_2 needs to be found. Assuming the mass of the bead spring model and a polymer chain is the same, it can be derived that:

$$\rho_2 = \frac{M_w u}{n} \frac{6}{\pi d_2^3} \tag{B.1}$$

In this equation n is the number of beads (here $n = 2$), u is the atomic mass to kg conversion constant, and M_w and d_2 are the molecular weight of the polymer molecule and the diameter of a bead respectively, which are both unknown. The bead diameter can be calculated from the condition that the diffusion constants of the dumbbell and the polymer molecule need to be the same. Öttinger (1989) derived that the diffusion

constant of a hookean dumbbell can be approximated with $D_d \approx k_B T/\zeta$, and the Zimm (1956) model gives for the diffusion constant, D_Z, of a polymer molecule:

$$D_Z \approx \frac{k_B T}{\nu_1 \rho_1 R_g} \tag{B.2}$$

where R_g is the radius of gyration of the polymer molecule. Setting the two equations for the diffusion constant equal to each other and using $\zeta = 3\pi\rho_1\nu d_2$, an expression for the bead diameter can be found:

$$d_2 = \frac{R_g}{3\pi} \tag{B.3}$$

which makes that the two unknowns are now the radius of gyration, R_g, and the molecular weight, M_w. However, these two are related through the equation:

$$R_g = N^{3/5} a = \left(\frac{M_w}{M_a}\right)^{3/5} a \tag{B.4}$$

with, M_a the molecular weight per Kuhn length, and a the Kuhn length, which only leaves either R_g or M_w as unknown. To close the expression for ρ_*, the Deborah number is set equal to the zimm relaxation time in wall units and solved for the radius of gyration:

$$R_g = \left(\frac{\mathrm{De}}{\mathrm{Re}_\tau^2}\left(\frac{d_1}{\nu}\right)^2 \frac{k_B T}{\rho_1}\right)^{1/3} \tag{B.5}$$

Combining all the above equations the density ratio, $\rho^* = \rho_1/\rho_2$, is found to be:

$$\rho^* = \frac{a^{5/3}}{18}\frac{n}{M_a u}\frac{\rho_1}{(3\pi)^2}\left(\frac{\mathrm{De}}{\mathrm{Re}_\tau^2}\left(\frac{d_1}{\nu}\right)^2 \frac{k_B T}{\rho_1}\right)^{4/9} \tag{B.6}$$

Also, an expression is needed for d^*. Using equation B.3 is can be found that:

$$d^* = \frac{d_1}{d_2} = 3\pi\frac{d_1}{R_g} \tag{B.7}$$

which using equation B.5, can be rewritten as:

$$d^* = 3\pi d_1 \left(\frac{\mathrm{Re}_\tau^2}{\mathrm{De}} \left(\frac{\nu}{d_1} \right)^2 \frac{\rho_1}{k_B T} \right)^{1/3} \tag{B.8}$$

With the diameter and density ratios known, all the dimensionless groups can be determined.

The equilibrium length between two beads $x_{2,0}^+$ is the equal to the Radius of gyration in wall units, R_g^+, which, as can be found above, is equal to:

$$R_g^+ = 3\pi \frac{\mathrm{Re}_\tau}{d^*} \tag{B.9}$$

The last variable which has to be calculated is the number of chains that need to be simulated. In a pipe segment with diameter d_1 and length $5d_1$, the number of particles is equal to:

$$N_2 = \frac{5}{4}\pi d_1^3 c_{\,\mathrm{mol\,m^{-3}}} N_A \tag{B.10}$$

where the concentration in mole per cubic meter, $c_{\,\mathrm{mol\,m^{-3}}}$, equals:

$$c_{\,\mathrm{mol\,m^{-3}}} = \frac{c_{\,\mathrm{p.p.m.w.}} \rho_1}{M_w} 10^3 \tag{B.11}$$

with the factor 10^3 stemming from the fact that the molecular weight, M_w, is given in $\mathrm{g\ mol^{-1}}$ instead of $\mathrm{kg\ mol^{-1}}$. Combining the above two equations and using the equation for the just calcuated bead density gives:

$$N_2 = \frac{15}{4\pi} \rho^* d^{*3} c_{\,\mathrm{p.p.m.w.}} \tag{B.12}$$

which is the number of chains in the computational domain corresponding to a concentration of 1 p.p.m.w..

APPENDIX C

SCALING OF MDR THEORY

In this appendix the scaling behavior of MDR theory is analyzed. We start with equation 18 from L'vov et al. (2004):

$$S^+\left(y^+\right) = \frac{1}{\kappa_V y^+}\left\{\left(\frac{y^+ L}{\mathrm{Re}_\tau l}\right) + \sqrt{1+\left[\left(2\kappa_K y_v^+ c_V\right)^2 - 1\right]\left(\frac{y^+ L}{\mathrm{Re}_\tau l}\right)^2}\right\} \tag{C.1}$$

This equation is supposed to be scaled in wall units, but parameters L and l are not. Non-dimensionalizing l and L to make the whole equation dimensionless gives:

$$S^+\left(y^+\right) = \frac{1}{\kappa_V y^+}\left\{\left(\frac{y^+}{l^+}\right) + \sqrt{1+\left[\left(2\kappa_K y_v^+ c_V\right)^2 - 1\right]\left(\frac{y^+}{l^+}\right)^2}\right\} \tag{C.2}$$

with:

$$l^+ = 2\kappa_K y_v^+ c_V \tau_p^+ \tag{C.3}$$

Here $\tau_p^+ = g\tilde{\tau}_p^+$, with $\tilde{\tau}_p^+$ the longest non-dimensional polymer relaxation time. This show that L'vov's theory does not actually scale with Re_τ, but has only τ_p^+ as parameter. Now lets take the limits $\tau_p^+ \to 0$ and $\tau_p^+ \to \infty$. For $\tau_p^+ \to \infty$, $S^+\left(y^+\right)$ correctly approaches $S^+\left(y^+\right) = \frac{1}{\kappa_V y^+}$. However, for $\tau_p^+ \to 0$, $S^+\left(y^+\right) \propto 1/\tilde{\tau}_p^+$ and not $S^+\left(y^+\right) = \frac{1}{\kappa_K y^+}$ as would be expected for polymer additives with a zero relaxation time.

APPENDIX D

VALIDATION

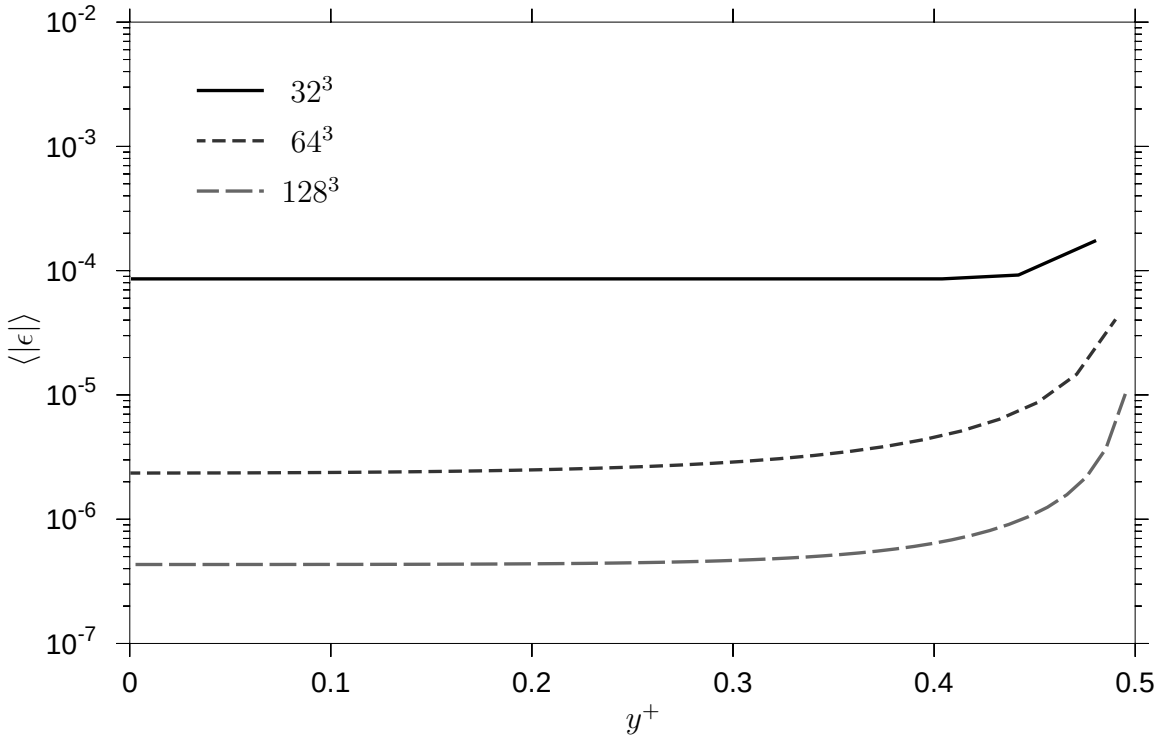

Figure D.1 – Average absolute error for the Poisson solver. The average absolute error compared with the analytical solution given by equation D.2. The error decreases almost 200 fold when decreasing the grid size 4 times, which makes the algorithm very close to 4th order accurate.

This section deals with the validation of the Poisson solver, the DNS code and the Langevin dynamics code. First we take a look at the Poisson solver. The Poisson solver was validated using the function:

$$f = -\frac{4}{25}(75 - 750r^2 - 4r^2\pi^2 + 8r^4\pi^2)\sin(\phi)\sin(\frac{2}{5}\pi z) \tag{D.1}$$

which has the following solution for the pressure field:

$$p = (\frac{1}{2}(2r)^4 - (2r)^2) * \sin(\phi) \sin(\frac{2}{5}\pi z) \tag{D.2}$$

This function is periodic in angular and streamwise direction, continuous in the center and has a derivative:

$$\left.\frac{\partial p}{\partial r}\right|_{r=0.5} = (4(2r)^3 - 4(2r)) * \sin(\phi) \sin(\frac{2}{5}\pi z)\Big|_{r=0.5} = 0 \tag{D.3}$$

at the wall, and thus obeys all boundary conditions. In figure D.1 the average absolute error can be seen. Even though the Poisson equation is solved on a non-homogeneous grid, the solver is very close to 4th order accurate in the center with a slightly higher error at the wall due to the Neumann boundary condition.

In graph D.2 the flow profile for laminar flow with a friction Reynolds number of $\mathrm{Re}_\tau = 100$ can be seen. The flow profile generated by the code exactly matches the equation:

$$w^+_{\text{theory}} = \frac{1}{\mathrm{Re}_\tau}\left(\left(\frac{\mathrm{Re}_\tau}{2}\right)^2 - r^{+2}\right) \tag{D.4}$$

which is the analytical solution of the Navier-Stokes equation for low-Reynolds-number Poiseuille flow.

The graphs D.3 and D.4 are a comparison of the code with LDA measurements done by Durst et al. (1993). It can be seen how the LDA measurements and the velocity and stresses are nearly identical and how, due to using a 4th order algorithm, there is no discontinuity in the stresses in the center of the pipe.

Figure D.5 shows the Reynolds shear stress $\langle u^+ w^+ \rangle$ and total shear stress $\langle \sigma^+_{rz} \rangle$. Because steady state is reached, the total shear stress must be a straight line to

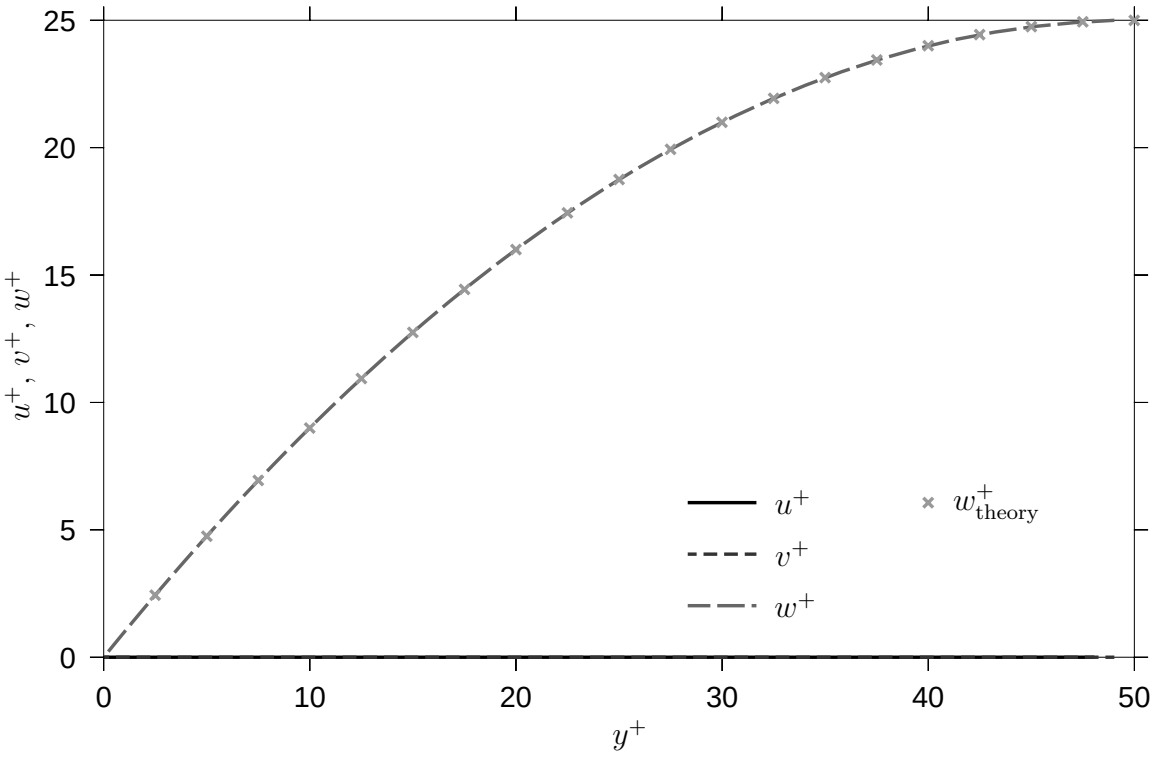

Figure D.2 – Average mean velocity profiles for $\mathbf{Re}_\tau = 100$. Laminar velocity profiles for $\mathrm{Re}_\tau = 100$. Both the result from the DNS and the profile for Poiseuille flow are shown, which match exactly.

balance the pressure gradient and the following relation can be derived from the momentum equation for mean axial velocity:

$$\left\langle \sigma^+_{rz} \right\rangle = \left\langle u^+ w^+ \right\rangle - \frac{\partial w^+}{\partial r^+} = 2\frac{r^+}{Re_\tau} \tag{D.5}$$

It can be seen in figure D.5 that this is indeed the case.

Graph D.6 shows the validation of the dissipation fluctuation theorem. In the graph it can be seen how $< r^+ >$ reaches a maximum value of 30 and how $< r^{+2} >$ is equal to $6D^+t^+$ till a value of 900 is reached. 30 and 900 are the diameter of the pipe and the diameter squared respectively in wall units for $Re_\tau = 30$. This confirms that the Brownian motion algorithm is working correctly.

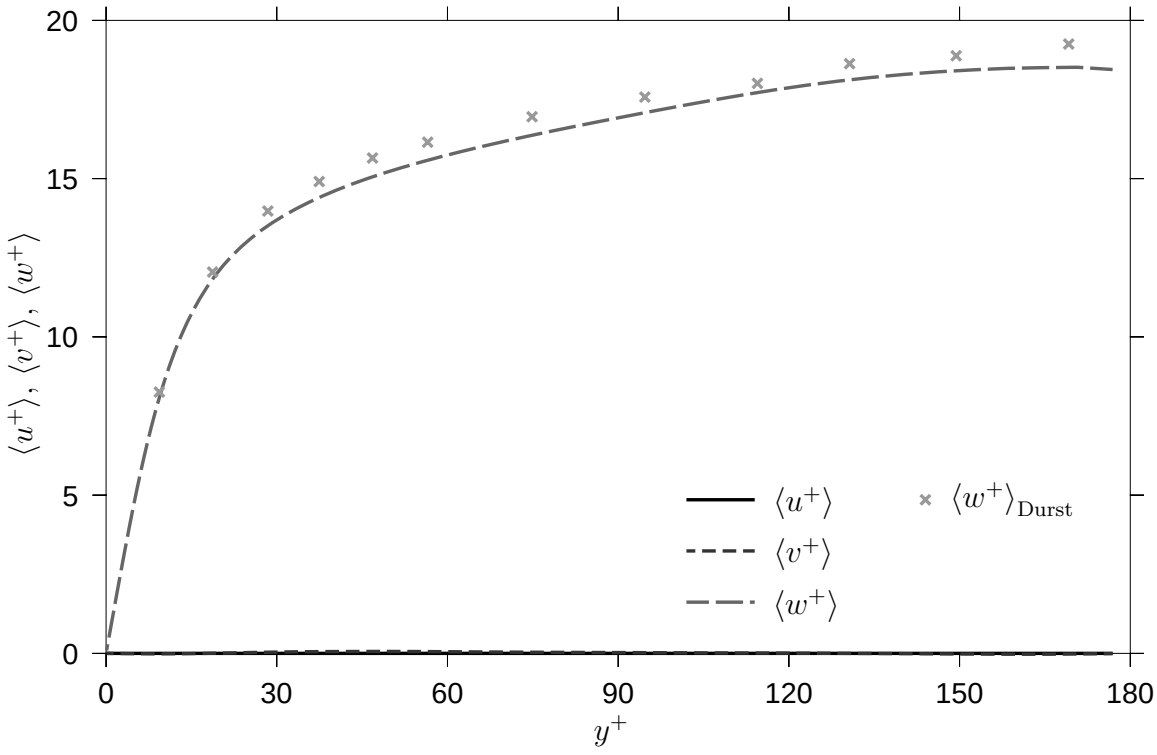

Figure D.3 – Average mean velocity profiles for $\mathbf{Re}_\tau = 360$. Turbulent velocity profiles for $\mathrm{Re}_\tau = 360$ comparing the code with LDA measurements made by Durst et al. (1993). The grid size is $72 \times 128 \times 256$ with a grid constant of 2.45.

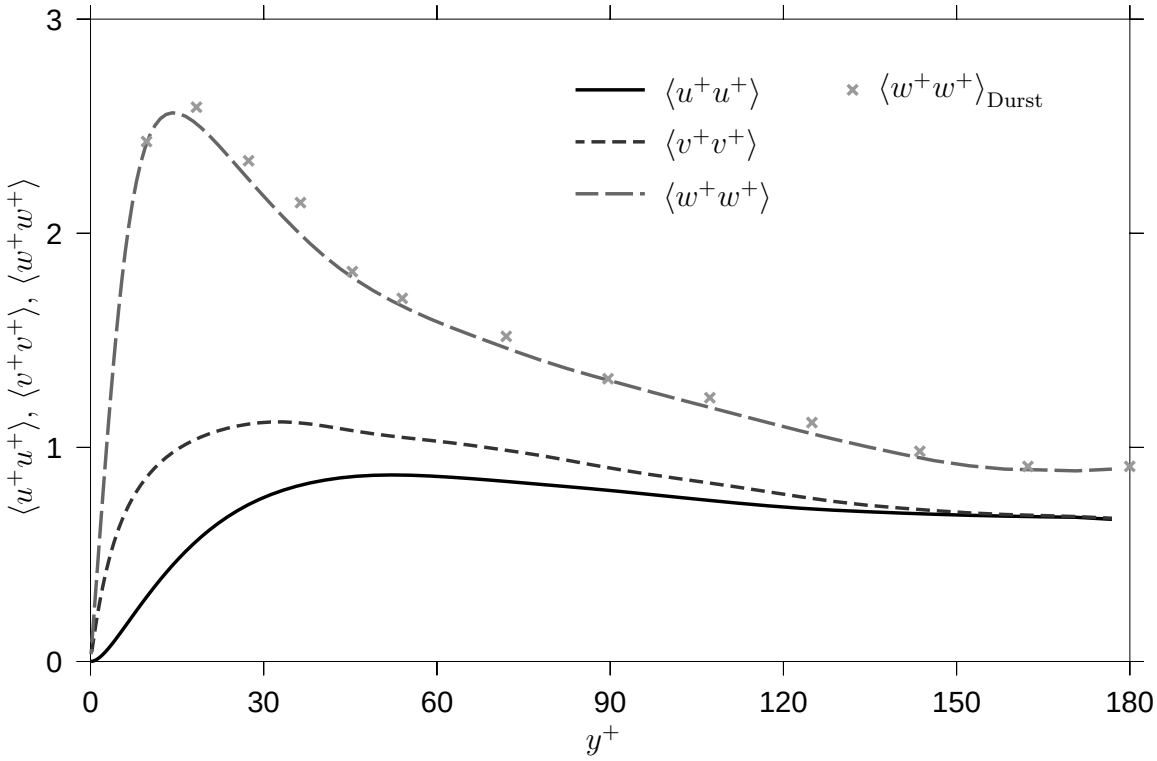

Figure D.4 – Average r.m.s velocity profiles for $\mathbf{Re}_\tau = 360$. Diagonal Reynolds stress profiles for $\mathrm{Re}_\tau = 360$. Comparing the code with LDA measurements made by Durst et al. (1993). The grid size is $72 \times 128 \times 256$ with a grid constant of 2.45.

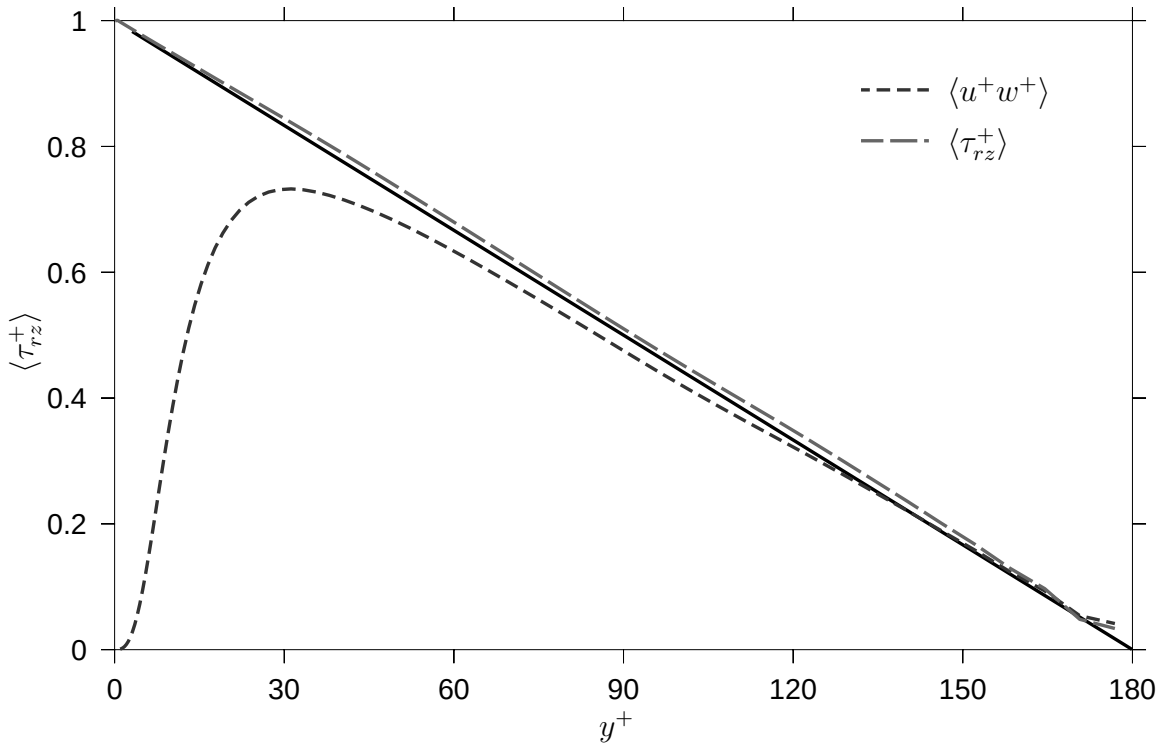

Figure D.5 – Reynolds shear stress and total shear stress for $\mathbf{Re}_\tau = 360$. Reynolds shear stress and total shear stress for $\mathrm{Re}_\tau = 360$. The grid size is $72 \times 128 \times 256$ with a grid constant of 2.45.

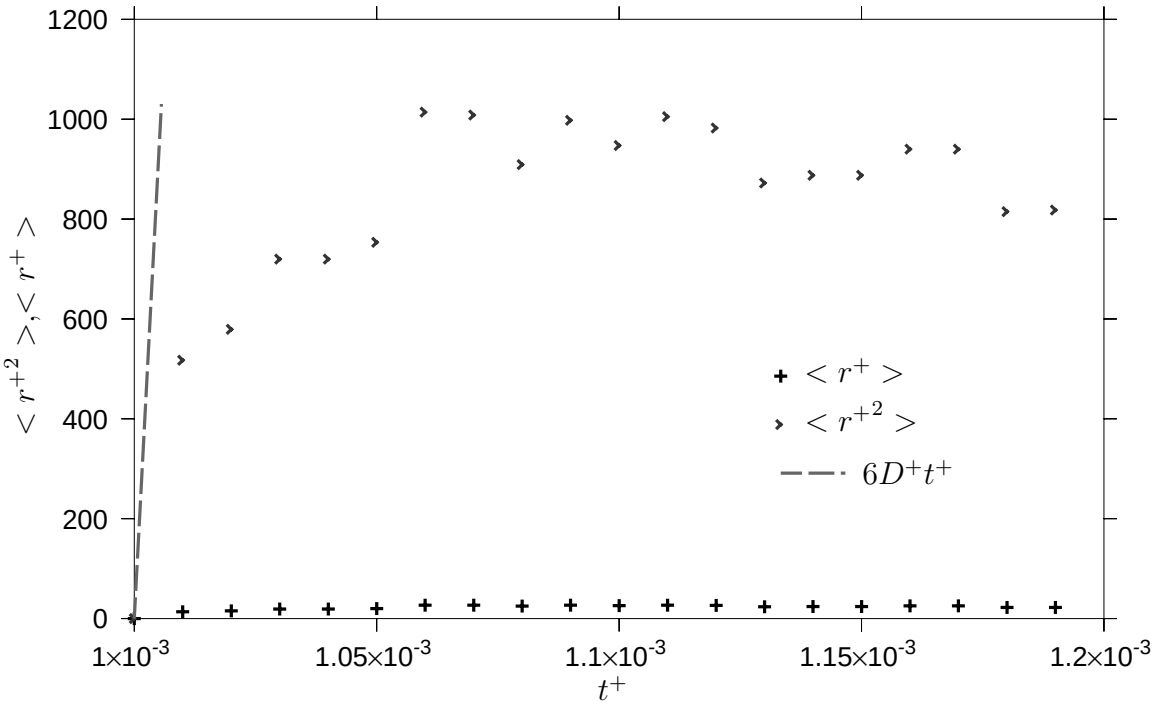

Figure D.6 – Validation of the fluctuation-dissipation theorem. The average distance traveled by the Brownian particles, $< r^+ >$, and the variance of the distance traveled by the Brownian particle, $< r^{+2} >$, as a function of time, t^+. $\mathrm{Re}_\tau = 30$, $\tau_2^+ = 7.51 \cdot 10^{-4}$ and $D^+ = 3.07 \cdot 10^7$

APPENDIX E

ENERGY BUDGETS OF REYNOLDS STRESSES

Using cylindrical coordinates and splitting up the polymer contribution in a body force contribution from the center of mass of each chain, f_2, and a stress contribution, τ_2, the radial component of the Navier-Stokes equation can be written as:

$$\begin{aligned}
&\rho\left(\frac{\partial u}{\partial t}+u\frac{\partial u}{\partial r}+\frac{v}{r}\frac{\partial u}{\partial \phi}-\frac{v^2}{r}+w\frac{\partial u}{\partial z}\right)= \\
&- \quad \frac{\partial p}{\partial r} \\
&+ \quad \mu\left[\frac{1}{r}\frac{\partial}{\partial r}\left(r\frac{\partial u}{\partial r}\right)-\frac{u}{r^2}+\frac{1}{r^2}\frac{\partial^2 u}{\partial \phi^2}-\frac{2}{r^2}\frac{\partial v}{\partial \phi}+\frac{\partial^2 u}{\partial z^2}\right] \\
&- \quad \left[\frac{1}{r}\frac{\partial}{\partial r}\left(r\tau_{rr,2}\right)+\frac{1}{r}\frac{\partial \tau_{r\phi,2}}{\partial \phi}-\frac{\tau_{\phi\phi,2}}{r}+\frac{\partial \tau_{rz,2}}{\partial z}\right] \\
&+ \quad f_{r,2}
\end{aligned} \tag{E.1}$$

the angular component as:

$$\begin{aligned}
&\rho\left(\frac{\partial v}{\partial t}+u\frac{\partial v}{\partial r}+\frac{v}{r}\frac{\partial v}{\partial \phi}+\frac{uv}{r}+w\frac{\partial v}{\partial z}\right) \\
&= \quad -\frac{1}{r}\frac{\partial p}{\partial \phi} \\
&+ \quad \mu\left[\frac{1}{r}\frac{\partial}{\partial r}\left(r\frac{\partial v}{\partial r}\right)-\frac{v}{r^2}+\frac{1}{r^2}\frac{\partial^2 v}{\partial \phi^2}+\frac{2}{r^2}\frac{\partial u}{\partial \phi}+\frac{\partial^2 v}{\partial z^2}\right] \\
&- \quad \left[\frac{1}{r^2}\frac{\partial}{\partial r}\left(r^2\tau_{\phi r,2}\right)+\frac{1}{r}\frac{\partial \tau_{\phi\phi,2}}{\partial \phi}+\frac{\partial \tau_{\phi z,2}}{\partial z}\right] \\
&+ \quad f_{\phi,2}
\end{aligned} \tag{E.2}$$

and the streamwise component as:

$$\begin{aligned}
&\rho\left(\frac{\partial w}{\partial t}+u\frac{\partial w}{\partial r}+\frac{v}{r}\frac{\partial w}{\partial \phi}+w\frac{\partial w}{\partial z}\right)\\
&= -\frac{\partial p}{\partial z}\\
&+ \mu\left[\frac{1}{r}\frac{\partial}{\partial r}\left(r\frac{\partial w}{\partial r}\right)+\frac{1}{r^2}\frac{\partial^2 w}{\partial \phi^2}+\frac{\partial^2 w}{\partial z^2}\right]\\
&- \left[\frac{1}{r}\frac{\partial}{\partial r}\left(r\tau_{zr,2}\right)+\frac{1}{r}\frac{\partial \tau_{z\phi,2}}{\partial \phi}+\frac{\partial \tau_{zz,2}}{\partial z}\right]\\
&+ f_{z,2}
\end{aligned} \tag{E.3}$$

Because the solvent is incompressible, the mass ballance in cylindrical coordinates is equal to:

$$\frac{1}{r}\frac{\partial}{\partial r}\left(ru\right)+\frac{1}{r}\frac{\partial v}{\partial \phi}+\frac{\partial w}{\partial z}=0 \tag{E.4}$$

Using the approach used in Tennekes & Lumley (1972) the different contributions to the Reynolds stress components can be calculated from the above equations. The calculation consists of subtracting the Reynolds averaged Navier-Stokes equations from the non averaged equation, to get the expression for the velocity fluctuations. The equations for the velocity fluctuations are then multiplied with the fluctuating velocity components and averaged again to get the different contributions to the Reynolds stress components. When the flow is steady state, summing up the different contributions should give an average value of zero, indicating that energy is conserved. For the diagonal Reynolds stress components this gives:

$$
\begin{aligned}
\frac{\partial}{\partial t}\langle uu\rangle = & \\
- & \underbrace{\frac{1}{r}\frac{\partial}{\partial r}\left(r\langle uuu\rangle\right) + 2\frac{\langle uvv\rangle}{r}}_{\text{TD}} \\
- & \underbrace{\frac{2}{\rho}\left\langle u\frac{\partial p}{\partial r}\right\rangle}_{\text{VP}} + \underbrace{\nu\frac{1}{r}\frac{\partial}{\partial r}\left(r\frac{\partial}{\partial r}\langle uu\rangle\right) - 2\nu\left[\frac{\langle uu\rangle}{r^2} - \frac{\langle vv\rangle}{r^2}\right]}_{\text{VD}} \\
- & \underbrace{2\nu\left[\left\langle\left(\frac{\partial u}{\partial r}\right)^2\right\rangle + \left\langle\left(\frac{1}{r}\frac{\partial u}{\partial \phi} - \frac{v}{r}\right)^2\right\rangle + \left\langle\left(\frac{\partial u}{\partial z}\right)^2\right\rangle\right]}_{\text{DS}} \\
+ & \underbrace{\frac{2}{\rho}\langle u f_{r,2}\rangle}_{\text{VF}} - \underbrace{\frac{2}{\rho}\left[\frac{1}{r}\frac{\partial}{\partial r}\left(r\langle u\tau_{rr,2}\rangle\right) - \frac{\langle u\tau_{\phi\phi,2}\rangle}{r} - \frac{\langle v\tau_{r\phi,2}\rangle}{r}\right]}_{\text{PD}} \\
+ & \underbrace{\frac{2}{\rho}\left[\left\langle\tau_{rr,2}\frac{\partial u}{\partial r}\right\rangle + \left\langle\tau_{r\phi,2}\left(\frac{1}{r}\frac{\partial u}{\partial \phi} - \frac{v}{r}\right)\right\rangle + \left\langle\tau_{rz,2}\frac{\partial u}{\partial z}\right\rangle\right]}_{\text{PS}}
\end{aligned}
\tag{E.5}
$$

$$
\begin{aligned}
\frac{\partial}{\partial t}\langle vv\rangle = & \\
- & \underbrace{\frac{1}{r}\frac{\partial}{\partial r}\left(r\langle uvv\rangle\right) - 2\frac{\langle uvv\rangle}{r}}_{\text{TD}} \\
- & \underbrace{\frac{2}{\rho}\left\langle v\frac{1}{r}\frac{\partial p}{\partial \phi}\right\rangle}_{\text{VP}} + \underbrace{\nu\frac{1}{r}\frac{\partial}{\partial r}\left(r\frac{\partial}{\partial r}\langle vv\rangle\right) + 2\nu\left[\frac{\langle uu\rangle}{r^2} - \frac{\langle vv\rangle}{r^2}\right]}_{\text{VD}} \\
- & \underbrace{2\nu\left[\left\langle\left(\frac{\partial v}{\partial r}\right)^2\right\rangle + \left\langle\left(\frac{1}{r}\frac{\partial v}{\partial \phi} + \frac{u}{r}\right)^2\right\rangle + \left\langle\left(\frac{\partial v}{\partial z}\right)^2\right\rangle\right]}_{\text{DS}} \\
+ & \underbrace{\frac{2}{\rho}\langle v f_{\phi,2}\rangle}_{\text{VF}} - \underbrace{\frac{2}{\rho}\left[\frac{1}{r^2}\frac{\partial}{\partial r}\left(r^2\langle v\tau_{\phi r,2}\rangle\right) + \frac{\langle u\tau_{\phi\phi,2}\rangle}{r}\right]}_{\text{PD}} \\
+ & \underbrace{\frac{2}{\rho}\left[\left\langle\tau_{\phi r,2}\frac{\partial v}{\partial r}\right\rangle + \left\langle\tau_{\phi\phi,2}\left(\frac{1}{r}\frac{\partial v}{\partial \phi} + \frac{u}{r}\right)\right\rangle + \left\langle\tau_{\phi z,2}\frac{\partial v}{\partial z}\right\rangle\right]}_{\text{PS}}
\end{aligned}
\tag{E.6}
$$

$$
\begin{aligned}
\frac{\partial}{\partial t}\left\langle ww\right\rangle = & \\
- & \underbrace{\frac{1}{r}\frac{\partial}{\partial r}\left(r\left\langle uww\right\rangle\right)}_{\mathrm{TD}} - \underbrace{2\left\langle uw\right\rangle\frac{\partial W}{\partial r}}_{\mathrm{PR}} \\
- & \underbrace{\frac{2}{\rho}\left\langle w\frac{\partial p}{\partial z}\right\rangle}_{\mathrm{VP}} + \underbrace{\nu\frac{1}{r}\frac{\partial}{\partial r}\left(r\frac{\partial}{\partial r}\left\langle ww\right\rangle\right)}_{\mathrm{VD}} \\
- & \underbrace{2\nu\left[\left\langle\left(\frac{\partial w}{\partial r}\right)^2\right\rangle + \left\langle\left(\frac{1}{r}\frac{\partial w}{\partial\phi}\right)^2\right\rangle + \left\langle\left(\frac{\partial w}{\partial z}\right)^2\right\rangle\right]}_{\mathrm{DS}} \\
+ & \underbrace{\frac{2}{\rho}\left\langle wf_{w,2}\right\rangle}_{\mathrm{VF}} - \underbrace{\frac{2}{\rho}\left[\frac{1}{r}\frac{\partial}{\partial r}\left(r\left\langle w\tau_{zr,2}\right\rangle\right)\right]}_{\mathrm{PD}} \\
+ & \underbrace{\frac{2}{\rho}\left[\left\langle\tau_{zr,2}\frac{\partial w}{\partial r}\right\rangle + \left\langle\tau_{z\phi,2}\frac{1}{r}\frac{\partial w}{\partial\phi}\right\rangle + \left\langle\tau_{zz,2}\frac{\partial w}{\partial z}\right\rangle\right]}_{\mathrm{PS}}
\end{aligned}
\tag{E.7}
$$

and for the off-diagonal components the contributions are:

$$
\begin{aligned}
\frac{\partial}{\partial t}\left\langle uv\right\rangle = & \\
- & \underbrace{\frac{1}{r}\frac{\partial}{\partial r}\left(r\left\langle uuv\right\rangle\right)+\frac{\left\langle vvv\right\rangle}{r}-\frac{\left\langle uuv\right\rangle}{r}}_{\text{TD}} \\
- & \underbrace{\frac{1}{\rho}\left\langle u\frac{1}{r}\frac{\partial p}{\partial\phi}\right\rangle-\frac{1}{\rho}\left\langle v\frac{\partial p}{\partial r}\right\rangle}_{\text{VP}}+\underbrace{\nu\frac{1}{r}\frac{\partial}{\partial r}\left(r\frac{\partial}{\partial r}\left\langle uv\right\rangle\right)-4\nu\frac{\left\langle uv\right\rangle}{r^2}}_{\text{VD}} \\
- & \underbrace{2\nu\left[\left\langle\left(\frac{\partial u}{\partial r}\right)\left(\frac{\partial v}{\partial r}\right)\right\rangle+\left\langle\left(\frac{1}{r}\frac{\partial u}{\partial\phi}-\frac{v}{r}\right)\left(\frac{1}{r}\frac{\partial v}{\partial\phi}+\frac{u}{r}\right)\right\rangle+\left\langle\left(\frac{\partial u}{\partial z}\right)\left(\frac{\partial v}{\partial z}\right)\right\rangle\right]}_{\text{DS}} \\
+ & \underbrace{\frac{1}{\rho}\left\langle uf_{\phi,2}\right\rangle+\frac{1}{\rho}\left\langle vf_{r,2}\right\rangle}_{\text{VF}} \\
- & \underbrace{\frac{1}{\rho}\left[\frac{1}{r^2}\frac{\partial}{\partial r}\left(r^2\left\langle u\tau_{\phi r,2}\right\rangle\right)+\frac{1}{r}\frac{\partial}{\partial r}\left(r\left\langle v\tau_{rr,2}\right\rangle\right)-2\frac{\left\langle v\tau_{\phi\phi,2}\right\rangle}{r}+\frac{\left\langle u\tau_{r\phi,2}\right\rangle}{r}\right]}_{\text{PD}} \\
+ & \underbrace{\frac{1}{\rho}\left[\left\langle\tau_{\phi r,2}\frac{\partial u}{\partial r}\right\rangle+\left\langle\tau_{\phi\phi,2}\left(\frac{1}{r}\frac{\partial u}{\partial\phi}-\frac{v}{r}\right)\right\rangle+\left\langle\tau_{\phi z,2}\frac{\partial u}{\partial z}\right\rangle\right]}_{\text{PS}} \\
+ & \underbrace{\frac{1}{\rho}\left[\left\langle\tau_{rr,2}\frac{\partial v}{\partial r}\right\rangle+\left\langle\tau_{r\phi,2}\left(\frac{1}{r}\frac{\partial v}{\partial\phi}+\frac{u}{r}\right)\right\rangle+\left\langle\tau_{rz,2}\frac{\partial v}{\partial z}\right\rangle\right]}_{\text{PS}}
\end{aligned}
\tag{E.8}
$$

$$
\begin{aligned}
&\frac{\partial}{\partial t}\langle uw\rangle = \\
&- \underbrace{\frac{1}{r}\frac{\partial}{\partial r}\left(r\langle uuw\rangle\right) + \frac{\langle wvv\rangle}{r}}_{\text{TD}} - \underbrace{\langle uu\rangle\frac{\partial W}{\partial r}}_{\text{PR}} \\
&- \underbrace{\frac{1}{\rho}\left\langle u\frac{\partial p}{\partial z}\right\rangle - \frac{1}{\rho}\left\langle v\frac{\partial p}{\partial r}\right\rangle}_{\text{VP}} + \underbrace{\nu\frac{1}{r}\frac{\partial}{\partial r}\left(r\frac{\partial}{\partial r}\langle uw\rangle\right) - \nu\frac{\langle uw\rangle}{r^2}}_{\text{VD}} \\
&- \underbrace{2\nu\left[\left\langle\left(\frac{\partial u}{\partial r}\right)\left(\frac{\partial w}{\partial r}\right)\right\rangle + \left\langle\left(\frac{1}{r}\frac{\partial u}{\partial \phi} - \frac{v}{r}\right)\left(\frac{1}{r}\frac{\partial w}{\partial \phi}\right)\right\rangle + \left\langle\left(\frac{\partial u}{\partial z}\right)\left(\frac{\partial w}{\partial z}\right)\right\rangle\right]}_{\text{DS}} \\
&+ \underbrace{\frac{1}{\rho}\langle uf_{z,2}\rangle + \frac{1}{\rho}\langle wf_{r,2}\rangle}_{\text{VF}} \\
&- \underbrace{\frac{1}{\rho}\left[\frac{1}{r}\frac{\partial}{\partial r}\left(r\langle u\tau_{zr,2}\rangle\right) + \frac{1}{r}\frac{\partial}{\partial r}\left(r\langle w\tau_{rr,2}\rangle\right) - \frac{\langle w\tau_{\phi\phi,2}\rangle}{r} - \frac{\langle v\tau_{z\phi,2}\rangle}{r}\right]}_{\text{PD}} \\
&+ \underbrace{\frac{1}{\rho}\left[\left\langle\tau_{zr,2}\frac{\partial u}{\partial r}\right\rangle + \left\langle\tau_{z\phi,2}\left(\frac{1}{r}\frac{\partial u}{\partial \phi} - \frac{v}{r}\right)\right\rangle + \left\langle\tau_{zz,2}\frac{\partial u}{\partial z}\right\rangle\right]}_{\text{PS}} \\
&+ \underbrace{\frac{1}{\rho}\left[\left\langle\tau_{rr,2}\frac{\partial w}{\partial r}\right\rangle + \left\langle\tau_{r\phi,2}\frac{1}{r}\frac{\partial w}{\partial \phi}\right\rangle + \left\langle\tau_{rz,2}\frac{\partial w}{\partial z}\right\rangle\right]}_{\text{PS}}
\end{aligned}
\tag{E.9}
$$

$$
\begin{aligned}
&\frac{\partial}{\partial t}\langle vw\rangle = \\
&- \underbrace{\frac{1}{r}\frac{\partial}{\partial r}\left(r\langle uvw\rangle\right) - \frac{\langle uvw\rangle}{r}}_{\text{TD}} - \underbrace{\langle uv\rangle\frac{\partial W}{\partial r}}_{\text{PR}} \\
&- \underbrace{\frac{1}{\rho}\left\langle v\frac{\partial p}{\partial z}\right\rangle - \frac{1}{\rho}\left\langle w\frac{1}{r}\frac{\partial p}{\partial \phi}\right\rangle}_{\text{VP}} + \underbrace{\nu\frac{1}{r}\frac{\partial}{\partial r}\left(r\frac{\partial}{\partial r}\langle vw\rangle\right) - \nu\frac{\langle vw\rangle}{r^2}}_{\text{VD}} \\
&- \underbrace{2\nu\left[\left\langle\left(\frac{\partial v}{\partial r}\right)\left(\frac{\partial w}{\partial r}\right)\right\rangle + \left\langle\left(\frac{1}{r}\frac{\partial v}{\partial \phi} + \frac{u}{r}\right)\left(\frac{1}{r}\frac{\partial w}{\partial \phi}\right)\right\rangle + \left\langle\left(\frac{\partial v}{\partial z}\right)\left(\frac{\partial w}{\partial z}\right)\right\rangle\right]}_{\text{DS}} \\
&+ \underbrace{\frac{1}{\rho}\langle vf_{z,2}\rangle + \frac{1}{\rho}\langle wf_{\phi,2}\rangle}_{\text{VF}} \\
&- \underbrace{\frac{1}{\rho}\left[\frac{1}{r}\frac{\partial}{\partial r}\left(r\langle v\tau_{zr,2}\rangle\right) + \frac{1}{r^2}\frac{\partial}{\partial r}\left(r^2\langle w\tau_{\phi r,2}\rangle\right) + \frac{\langle u\tau_{z\phi,2}\rangle}{r}\right]}_{\text{PD}} \\
&+ \underbrace{\frac{1}{\rho}\left[\left\langle\tau_{zr,2}\frac{\partial v}{\partial r}\right\rangle + \left\langle\tau_{z\phi,2}\left(\frac{1}{r}\frac{\partial v}{\partial \phi} + \frac{u}{r}\right)\right\rangle + \left\langle\tau_{zz,2}\frac{\partial v}{\partial z}\right\rangle\right]}_{\text{PS}} \\
&+ \underbrace{\frac{1}{\rho}\left[\left\langle\tau_{\phi r,2}\frac{\partial w}{\partial r}\right\rangle + \left\langle\tau_{\phi\phi,2}\frac{1}{r}\frac{\partial w}{\partial \phi}\right\rangle + \left\langle\tau_{\phi z,2}\frac{\partial w}{\partial z}\right\rangle\right]}_{\text{PS}}
\end{aligned}
\tag{E.10}
$$

The above equations are the same equations as found in Eggels (1994), exept for the polymer contributions. The different contributions are: TD: Turbulent Diffusion, PR: PRoduction, CT: Convective Transport, VP: Velocity-Pressure gradient interaction, VD: Viscous Diffusion, DS: viscous DiSsipation, PD: Polymer Diffusion, PS: Polymer diSsipation, and VF: Velocity-polymer Force interaction.

In the graphs in this section the different contributions derived above are shown. Because they are very small, the polymer contributions are shown seperately in graphs E.5, E.6, E.7, and E.8. All the graps are for Deborah number De = 0, which was choosen because it shows the strongest drag reduction. It can be seen that the stress contribution from the polymers and fibers have the tendency dampen the reynolds stresses, while the translational contribution is a production term. This could explain

why for fibers with a too large particle relaxation time there is an increase in the drag, because increased drag force on the fiber results in an increase of the reynolds stresses. Looking at graphs E.1, E.2, E.3, and E.4, it can be seen that all gain and loss terms indeed average out to a zero net contribution.

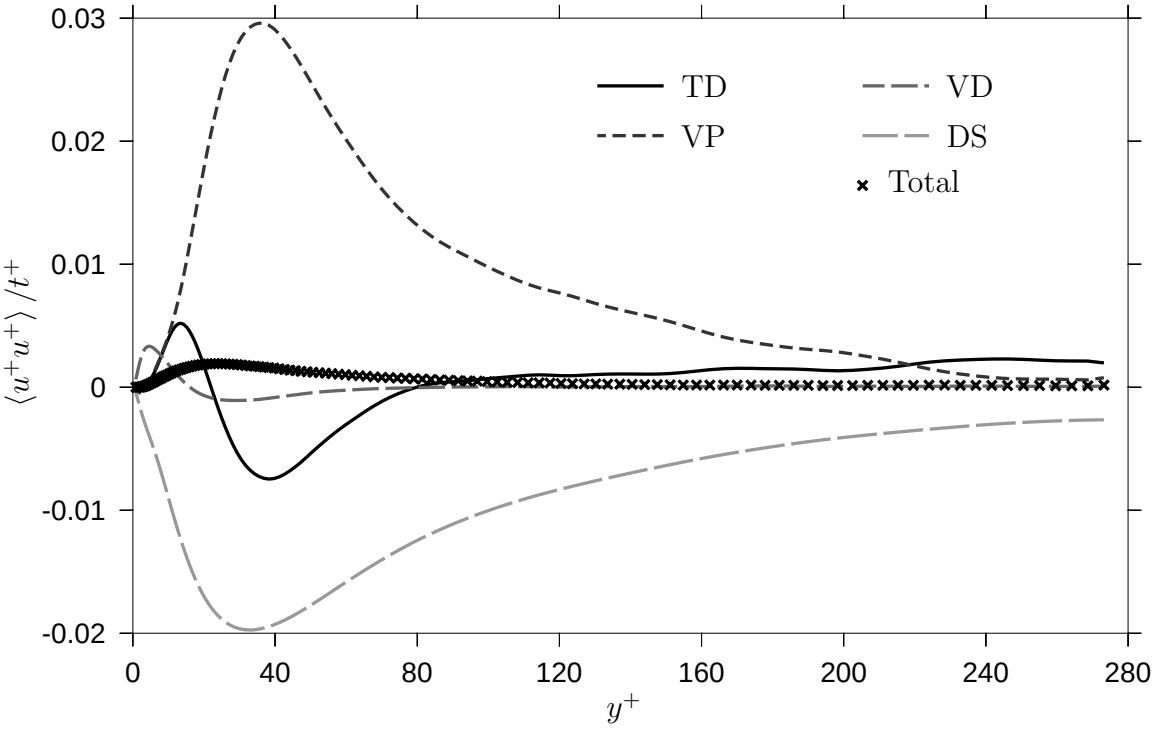

Figure E.1 – Contributions to $\langle u^+u^+\rangle$ Reynolds stress component. Contributions to the $\langle u^+u^+\rangle$ Reynolds stress component for $\mathrm{Re}_\tau = 560$ and $\mathrm{De} = 0$.

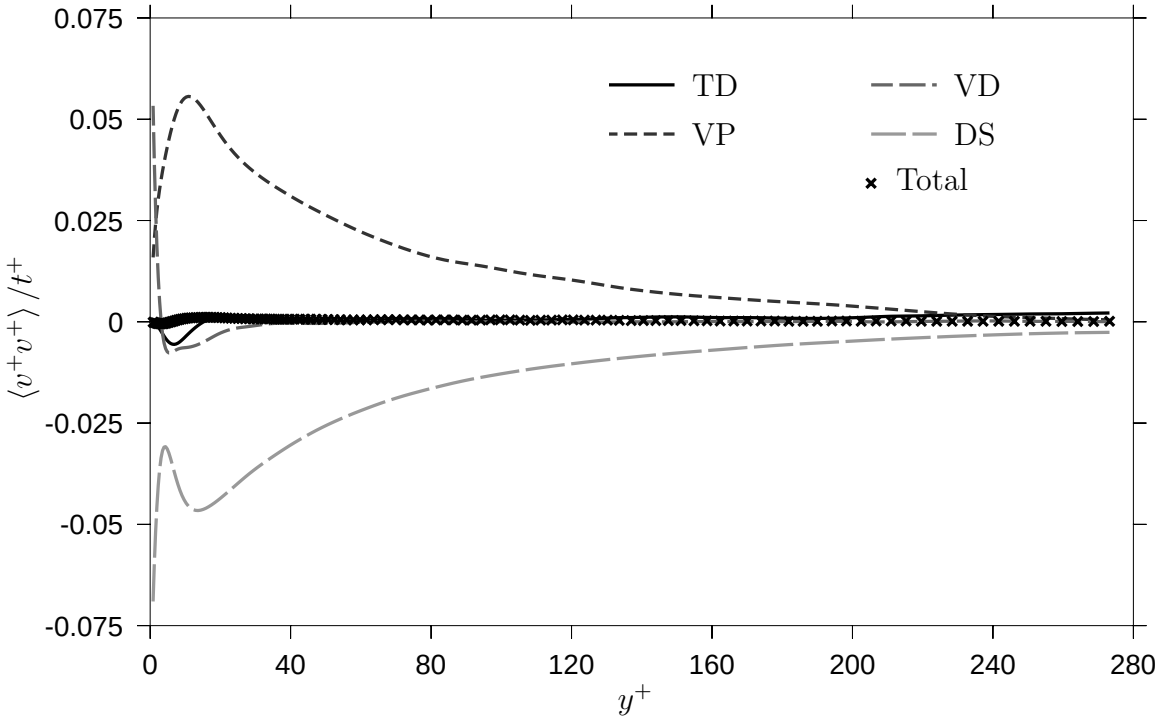

Figure E.2 – Contributions to $\langle v^+v^+\rangle$ Reynolds stress component. Contributions to the $\langle v^+v^+\rangle$ Reynolds stress component for $\mathrm{Re}_\tau = 560$ and $\mathrm{De} = 0$.

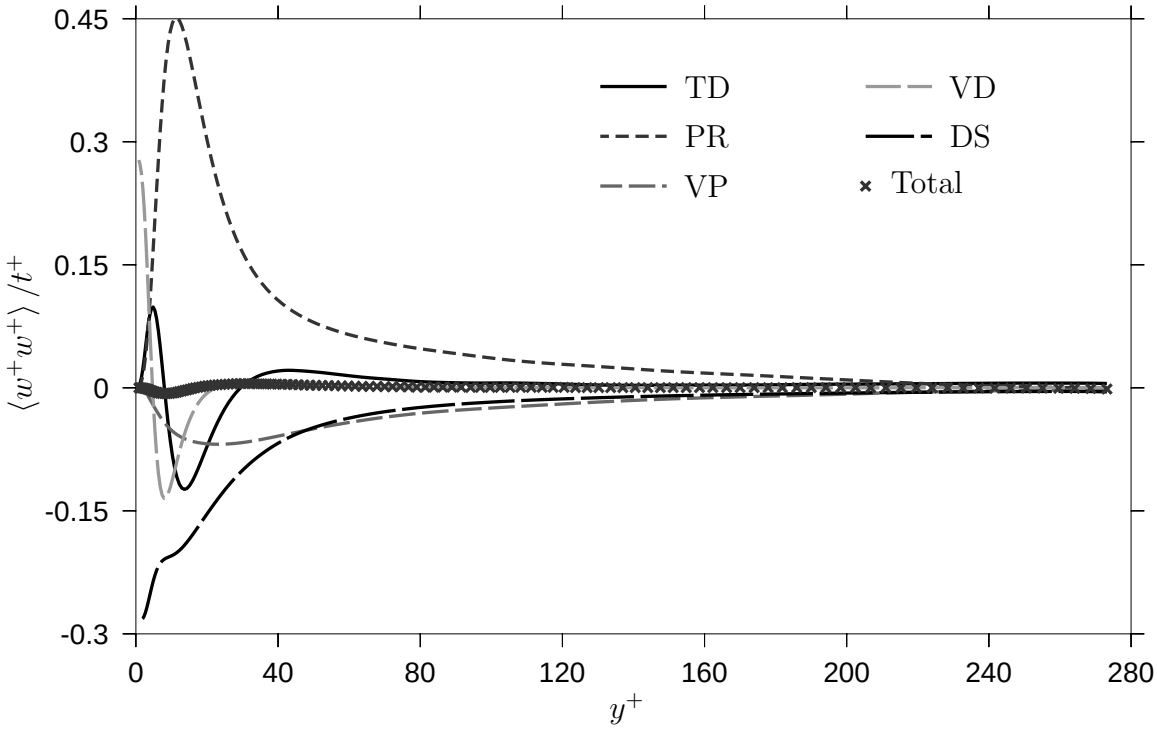

Figure E.3 – Contributions to $\langle w^+w^+\rangle$ Reynolds stress component. Contributions to the $\langle w^+w^+\rangle$ Reynolds stress component for $\mathrm{Re}_\tau = 560$ and $\mathrm{De} = 0$.

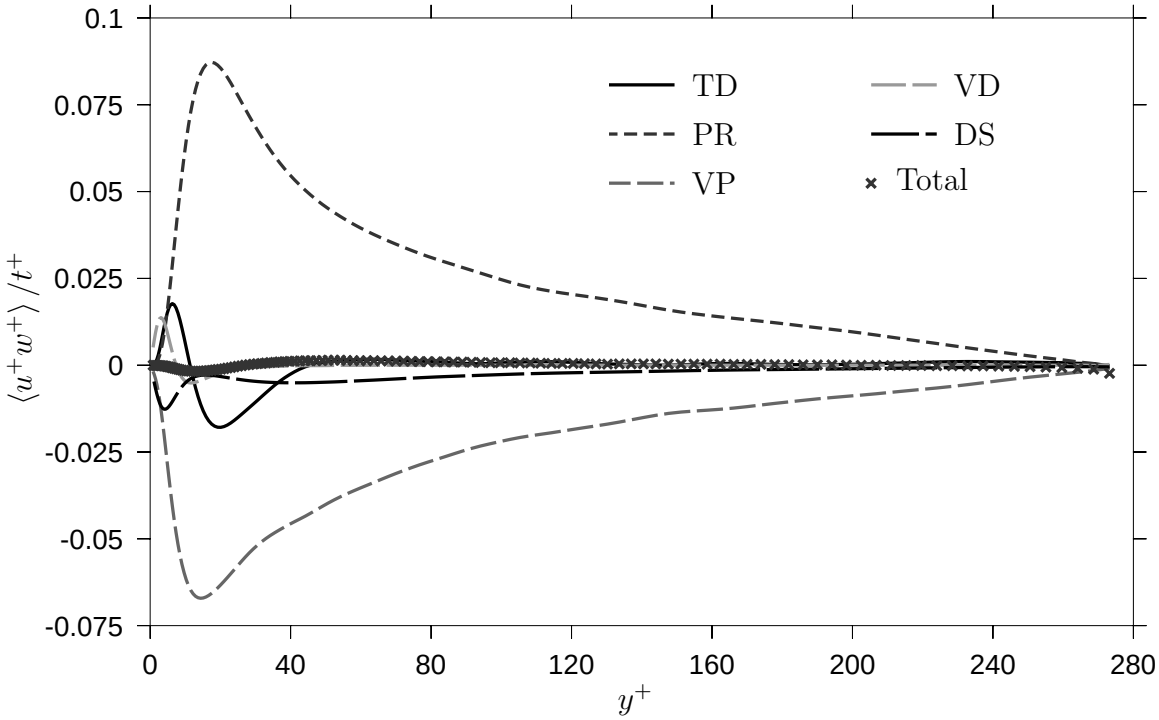

Figure E.4 – Contributions to $\langle u^+w^+\rangle$ Reynolds stress component. Contributions to the $\langle u^+w^+\rangle$ Reynolds stress component for $\mathrm{Re}_\tau = 560$ and $\mathrm{De} = 0$.

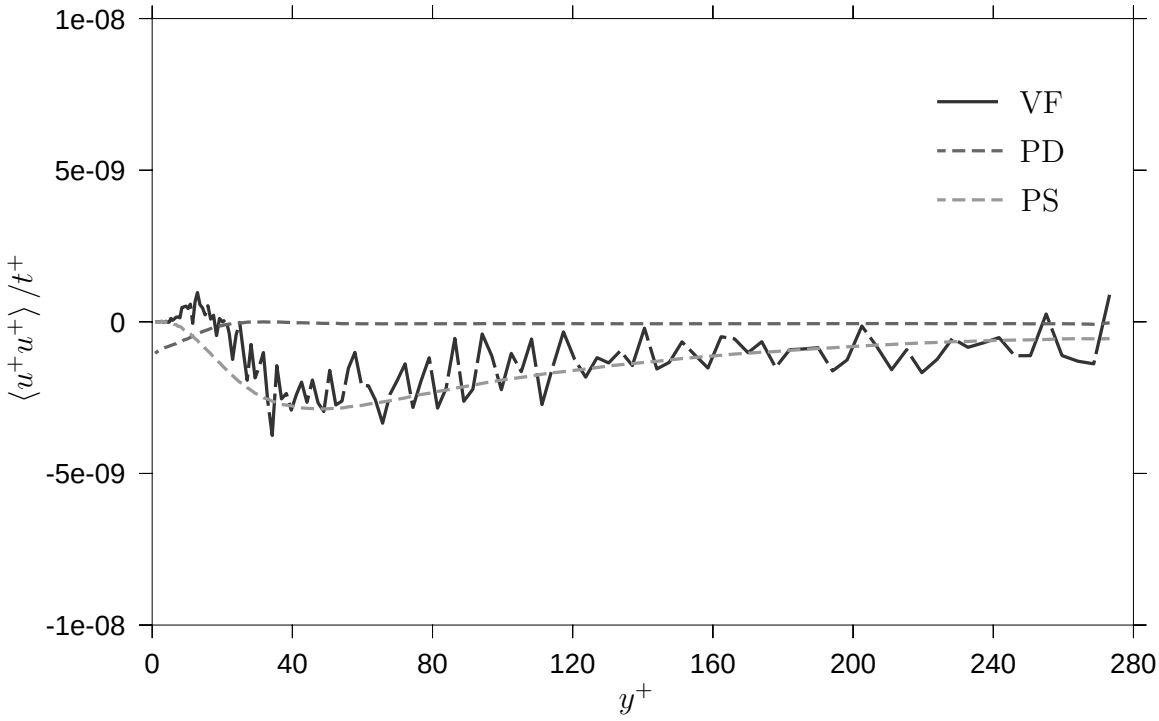

Figure E.5 – Polymer Contributions to $\langle u^+u^+\rangle$ Reynolds stress component. Polymer contributions to the $\langle u^+u^+\rangle$ Reynolds stress component for $\mathrm{Re}_\tau = 560$ and $\mathrm{De} = 0$.

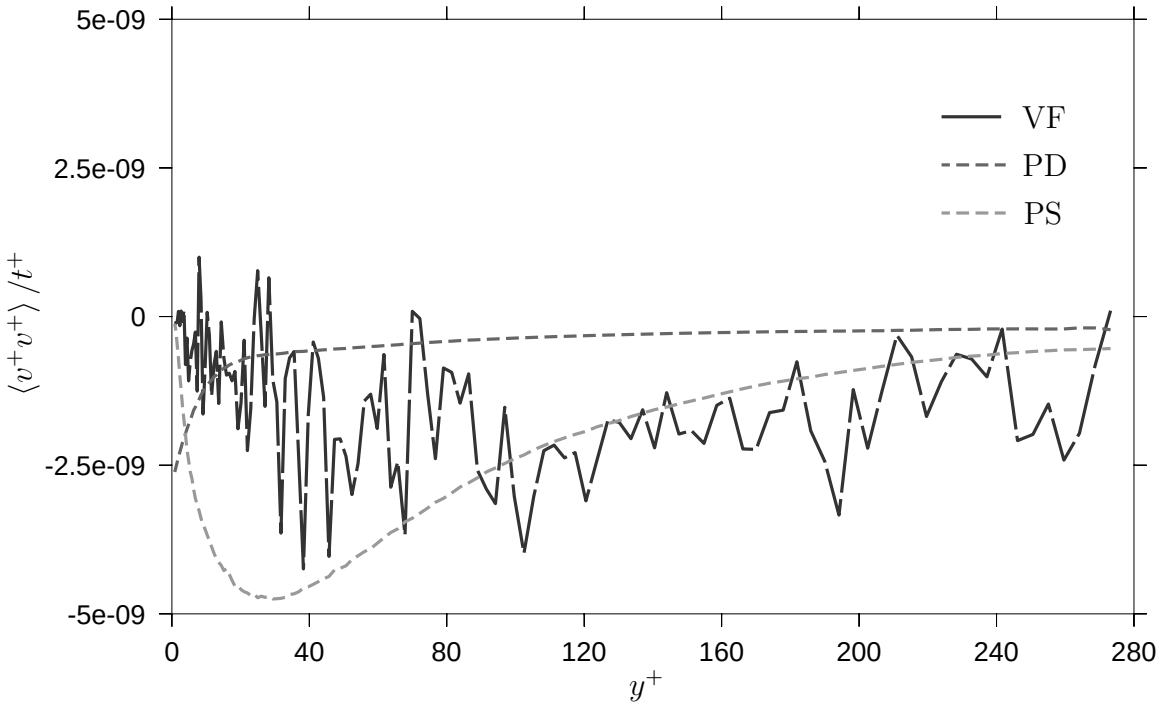

Figure E.6 – Polymer Contributions to $\langle v^+v^+\rangle$ Reynolds stress component. Polymer contributions to the $\langle v^+v^+\rangle$ Reynolds stress component for $\mathrm{Re}_\tau = 560$ and $\mathrm{De} = 0$.

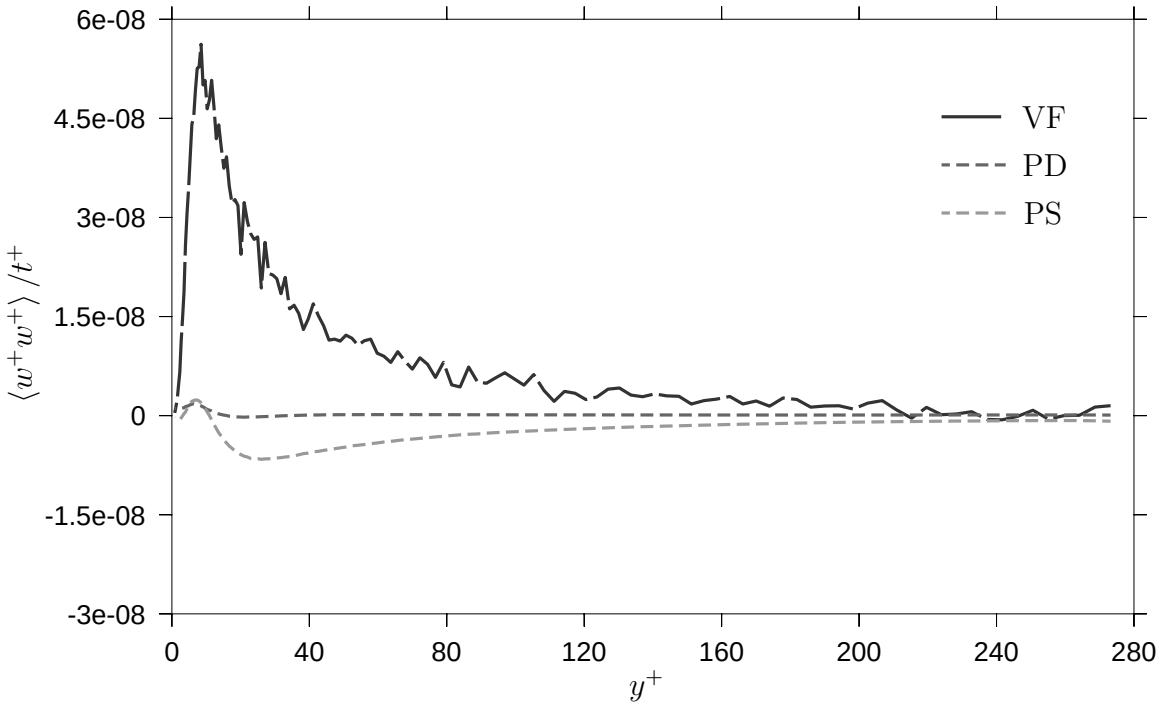

Figure E.7 – Polymer Contributions to $\langle w^+w^+\rangle$ Reynolds stress component. Polymer contributions to the $\langle w^+w^+\rangle$ Reynolds stress component for $\mathrm{Re}_\tau = 560$ and $\mathrm{De} = 0$.

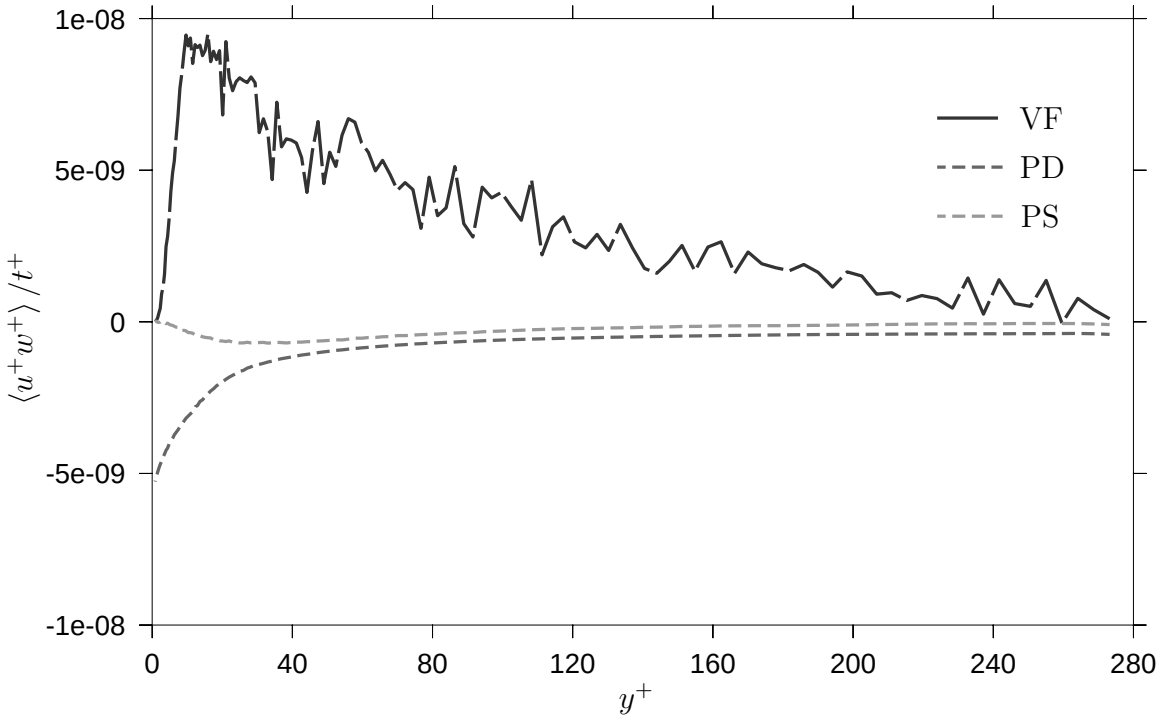

Figure E.8 – Polymer Contributions to $\langle u^+w^+\rangle$ Reynolds stress component. Polymer contributions to the $\langle u^+w^+\rangle$ Reynolds stress component for $\mathrm{Re}_\tau = 560$ and $\mathrm{De} = 0$.

APPENDIX F

KOLMOGOROV SCALE

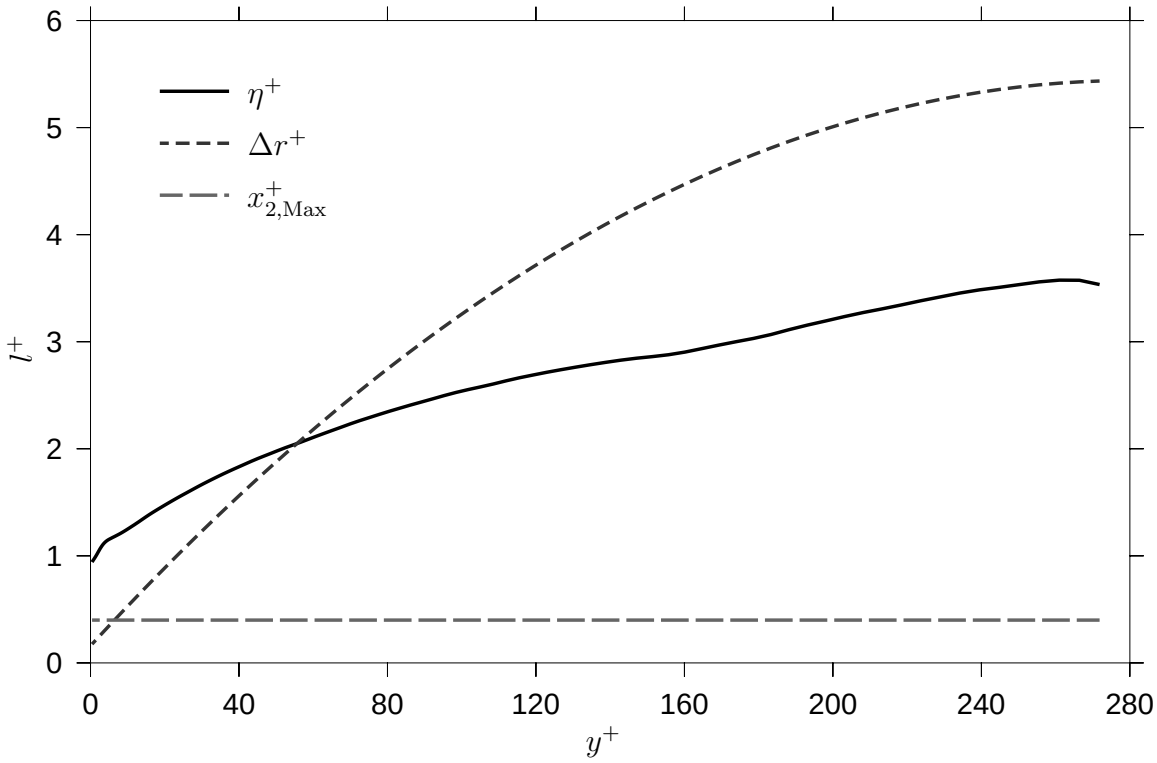

Figure F.1 – Comparison with Kolmogorov length scale. A comparison of the grid spacing for grid size $128 \times 256 \times 256$ with a grid constant of 2.45, the maximum polymer extension, and the Kolmogorov length scale.

Figure F.1 shows the Kolmogorov length scale in wall units, η^+, the radial grid spacing, Δr^+, and the maximum polymer extension, $x^+_{2,\mathrm{Max}}$. The Kolmogorov length scale is calculated as:

$$\eta^+ = \left(\frac{1}{\epsilon^+}\right)^{\frac{1}{4}} \tag{F.1}$$

where ϵ^+ is the dissipation rate of Turbulent Kinetic Energy (TKE). Comparing the Kolmogorov scale with the maximum extension, it can be seen that as expected both the polymers and fibers are always shorter than the Kolmogorov length scale. Comparing the grid spacing for the used grid size ($128 \times 256 \times 256$ with a grid constant of 2.45) with the kolmogorov scale, confirms that the grid size is slightly coarse. Since the grid at the wall is fine enough and considering other drag reduction result using a coarse grid (Choi et al. 1994), it is expected that the results hold when all the length scales are fully resolved.

BIBLIOGRAPHY

Andersen, H. C. (1983), 'Rattle: a "velocity" version of the shake algorithm for molecular dynamics calculations', *Journal of Computational Physics* **52**(1), 24–34.

Benzi, R., De Angelis, E., L'vov, V. S., Procaccia, I. & Tiberkevich, V. (2006), 'Maximum drag reduction asymptotes and the cross-over to the newtonian plug', *Journal of Fluid Mechanics* **551**, 185–195.

Benzi, R., L'vov, V. S., Procaccia, I. & Tiberkevich, V. (2004), 'Saturation of turbulent drag reduction in dilute polymer solutions', *Europhysics Letters* **68**(6), 825–831.

Berman, N. S. (1977*a*), 'Drag reduction of the highest molecular weight fractions of polyethylene oxide', *Physics of Fluids* **20**, 715–718.

Berman, N. S. (1977*b*), 'Flow time scales and drag reduction', *Physics of Fluids* **20**(10), S168–S174.

Berman, N. S. (1978), 'Drag reduction by polymers', *Annual Review of Fluid Mechanics* **10**(1), 47–64.

Berman, N. S. & George Jr, W. K. (1974), 'Onset of drag reduction in dilute polymer solutions', *Physics of Fluids* **17**, 250–251.

Bewersdorff, H. W., Gyr, A., Hoyer, K. & Tsinober, A. (1993), 'An investigation of possible mechanisms of heterogeneous drag reduction in pipe and channel flows', *Rheologica Acta* **32**(2), 140–149.

Bird, R. B. & Curtiss, C. F. (1985), Molecular theory expressions for the stress tensor in flowing polymeric liquids, *in* 'Journal of polymer science: Polymer symposia', Vol. 73, Wiley Online Library, pp. 187–199.

Bird, R. B., Curtiss, C. F., Armstrong, R. C., Hassager, O. & Wiley, J. (1987), *Dynamics of Polymeric Liquids, Kinetic Theory*, Vol. 2, 2 edn, John Wiley & Sons, Inc., New York.

Bird, R. B. & Hassager, O. (1987), *Dynamics of Polymeric Liquids: Fluid mechanics*, Dynamics of Polymeric Liquids, Wiley.

Boelens, A. M. P. & Portela, L. (2007), 'DNS study of local-equilibrium models in dilute particle-laden turbulent pipe flows', *Particle-Laden Flow* pp. 193–206.

Burger, E. D., Chorn, L. G. & Perkins, T. K. (1980), 'Studies of drag reduction conducted over a broad range of pipeline conditions when flowing Prudhoe Bay crude oil', *Journal of Rheology* **24**, 603–626.

Bushnell, D. M. & McGinley, C. (1989), 'Turbulence control in wall flows', *Annual Review of Fluid Mechanics* **21**(1), 1–20.

Cadot, O., Bonn, D. & Douady, S. (1998), 'Turbulent drag reduction in a closed flow system: Boundary layer versus bulk effects', *Physics of Fluids* **10**, 426–436.

Canham, H. J. S., Catchpole, J. P. & Long, R. (1970), *Boundary layer additives to reduce ship resistance*, Royal Institution of Naval Architects.

Choi, H., Moin, P. & Kim, J. (1993), 'Direct numerical simulation of turbulent flow over riblets', *Journal of Fluid Mechanics* **255**(-1), 503–539.

Choi, H., Moin, P. & Kim, J. (1994), 'Active turbulence control for drag reduction in wall-bounded flows', *Journal of Fluid Mechanics* **262**(-1), 75–110.

Corino, E. & Brodkey, R. S. (1969), 'A visual investigation of the wall region in turbulent flow', *Journal of Fluid Mechanics* **37**(01), 1–30.

Daoudi, S. & Brochard, F. (1978), 'Flows of flexible polymer-solutions in pores', *Macromolecules* **11**(4), 751–758.

Davila, J. & Hunt, J. C. R. (2001), 'Settling of small particles near vortices and in turbulence', *Journal of Fluid Mechanics* **440**, 117–145.

Davoudi, J. & Schumacher, J. (2006), 'Stretching of polymers around the kolmogorov scale in a turbulent shear flow', *Physics of Fluids* **18**(2), 025103.

De Angelis, E., Casciola, C. M., L'vov, V. S., Pomyalov, A., Procaccia, I. & Tiberkevich, V. (2004), 'Drag reduction by a linear viscosity profile', *Physical Review E* **70**(5), 055301.

De Angelis, E., Casciola, C. M. & Piva, R. (2002), 'Dns of wall turbulence: dilute polymers and self-sustaining mechanisms', *Computers & Fluids* **31**(4-7), 495–507.

De Gennes, P. G. (1986), 'Towards a scaling theory of drag reduction', *Physica A* **140**(1-2), 9–25.

De Gennes, P. G. (1990), *Introduction to polymer dynamics*, Cambridge.

Den toonder, J. M. J., Hulsen, M. A., Kuiken, G. D. C. & Nieuwstadt, F. T. M. (1997), 'Drag reduction by polymer additives in a turbulent pipe flow: Numerical and laboratory experiments', *Journal of Fluid Mechanics* **337**, 193–231.

Dimitropoulos, C. D., Dubief, Y., Shaqfeh, E. & Moin, P. (2006), 'Direct numerical simulation of polymer-induced drag reduction in turbulent boundary layer flow of inhomogeneous polymer solutions', *Journal of Fluid Mechanics* **566**(1), 153–162.

Doering, C. R., Eckhardt, B. & Schumacher, J. (2006), 'Failure of energy stability in Oldroyd-B fluids at arbitrarily low Reynolds numbers', *Journal of Non-Newtonian Fluid Mechanics* **135**(2-3), 92–96.

Doi, M. & Edwards, S. F. (1986), *The theory of polymer dynamics*, Clarendon Press, Oxford.

Dubief, Y., Terrapon, V. E., White, C. M., Shaqfeh, E. S. G., Moin, P. & Lele, S. K. (2005), 'New answers on the interaction between polymers and vortices in turbulent flows', *Flow, turbulence and combustion* **74**(4), 311–329.

Dubief, Y., White, C. M., Terrapon, V. E., Shaqfeh, E. S. G., Moin, P. & Lele, S. K. (2004), 'On the coherent drag-reducing and turbulence-enhancing behaviour of polymers in wall flows', *Journal of Fluid Mechanics* **514**, 271–280.

Durst, F., Jovanovic, J. & Sender, J. (1993), 'Detailed measurements of the near wall region of turbulent pipe flow', *ASME-PUBLICATIONS-FED* **146**, 79–79.

Eggels, J. (1994), Direct and Large Eddy Simulation of Turbulent flow in a Cylindrical Pipe Geometry, PhD thesis, TU Delft, Delft.

Elghobashi, S. & Truesdell, G. C. (1993), 'On the two-way interaction between homogeneous turbulence and dispersed solid particles. i: Turbulence modification', *Physics of Fluids A Fluid Dynamics* **5**, 1790–1790.

Fisher, D. & Rodriguez, F. (1971), 'Degradation of drag-reducing polymers', *Journal of Applied Polymer Science* **15**(12), 2975–2985.

Gampert, B. & Wagner, P. (1982), 'Turbulent-flow with polymer additives', *Archives of Mechanics* **34**(4), 493–502.

Gillissen, J. J. J. (2008), Numerical Simulation of Fibre-Induced Drag Reduction in Turbulent Channel Flow, PhD thesis, TU Delft.

Gupta, V. K., Sureshkumar, R. & Khomami, B. (2004), 'Polymer chain dynamics in newtonian and viscoelastic turbulent channel flows', *Physics of Fluids* **16**(5), 1546–1566.

Hershey, H. C. & Zakin, J. L. (1967), 'A molecular approach to predicting the onset of drag reduction in the turbulent flow of dilute polymer solutions', *Chemical Engineering Science* **22**, 1847–1856.

Hinze, J. O. (1975), 'Turbulence', *New York: McGraw* .

Hoyt, J. W. (1972), 'The effect of additives on fluid friction', *Transactions of the ASME. Series D, Journal of Basic Engineering* **94**, 258–285.

Hunt, J. C. R. & Durbin, P. (1999), 'Perturbed vortical layers and shear sheltering', *Fluid dynamics research* **24**, 375.

Huntson, D. & Reischman, M. M. (1975), 'The role of polydispersity in the mechanism of drag reduction', *Physics of Fluids* **18**, 1626.

Jiménez, J. J. I. M. & Pinelli, A. (1999), 'The autonomous cycle of near-wall turbulence', *Journal of Fluid Mechanics* **389**, 335–359.

Joseph, D. D. (1990), *Fluid dynamics of viscoelastic liquids*, Springer New York.

Joseph, D. D. & Christodoulou, C. (1993), 'Independent confirmation that delayed die swell is a hyperbolic transition', *Journal of Non-Newtonian Fluid Mechanics* **48**(3), 225–235.

Karniadakis, G. & Choi, K. (2003), 'Mechanisms on transverse motions in turbulent wall flows', *Annual Review of Fluid Mechanics* **35**(1), 45–62.

Kim, K., Adrian, R. J., Balachandar, S. & Sureshkumar, R. (2008), 'Dynamics of hairpin vortices and polymer-induced turbulent drag reduction', *Physical review letters* **100**(13), 134504.

Kirkwood, J. G. & Auer, P. L. (1951), 'The visco-elastic properties of solutions of rod-like macromolecules', *The Journal of Chemical Physics* **19**, 281.

Kline, S. J., Reynolds, W. C., Schraub, F. A. & Runstadler, P. W. (1967), 'The structure of turbulent boundary layers', *Journal of Fluid Mechanics* **30**(4), 741–773.

Kramers, H. A. (1944), 'Het gedrag van macromoleculen in een stroomende vloeistof', *Physica* **11**(1), 1–19.

Landahl, M. T. (1973), Drag reduction by polymer addition, *in* E. Becker & G. K. Mikhailov, eds, 'Proceedings of the 13th International Congress of Theoretical and Applied Mechanics', Springer, pp. 177–199.

Liaw, G. C., Zakin, J. L. & Patterson, G. K. (1971), 'Effects of molecular characteristics of polymers on drag reduction', *AIChE Journal* **17**(2), 391–397.

Lu, S. & Willmarth, W. W. (1973), 'Measurements of the structure of the reynolds stress in a turbulent boundary layer', *Journal of Fluid Mechanics* **60**(3), 481–511.

Lumley, J. L. (1969), 'Drag reduction by additives', *Annual Review of Fluid Mechanics* **1**, 367–384.

Lumley, J. L. (1973), 'Drag reduction in turbulent flow by polymer additives', *Journal of Polymer Science Macromolecular Reviews* **7**(1), 263–290.

L'vov, V. S., Pomyalov, A., Procaccia, I. & Tiberkevich, V. (2004), 'Drag reduction by polymers in wall bounded turbulence', *Physical Review Letters* **92**(24).

McComb, W. & Rabie, L. (1979), 'Development of local turbulent drag reduction due to nonuniform polymer concentration', *Physics of Fluids* **22**, 183–185.

Merrill, E. W., Smith, K. A., Shin, H. & Mickley, H. S. (1966), 'Study of Turbulent Flows of Dilute Polymer Solutions in a Couette Viscometer', *Journal of Rheology* **10**, 335–351.

Metzner, A. B. & Metzner, A. P. (1970), 'Stress levels in rapid extensional flows of polymeric fluids', *Rheologica Acta* **9**(2), 174–181.

Min, T., Jung, Y. Y., Choi, H. & Joseph, D. D. (2003), 'Drag reduction by polymer additives in a turbulent channel flow', *Journal of Fluid Mechanics* **486**, 213–238.

Moin, P. (2001), *Fundamentals of engineering numerical analysis*, Cambridge University Press.

Muthukumar, M. & Edwards, S. (1983), 'Screening of hydrodynamic interaction in a solution of rodlike macromolecules', *Macromolecules* **16**(9), 1475–1478.

Nadolink, R. (1987), Friction reduction in dilute polystyrene solutions, PhD thesis, University of California at San Diego, La Jolla, CA.

Öttinger, H. C. (1989), 'Gaussian approximation for Hookean dumbbells with hydrodynamic interaction: Translational diffusivity', *Colloid & Polymer Science* **267**(1), 1–8.

Paterson, R. W. & Abernath, F. H. (1970), 'Turbulent flow drag reduction and degradation with dilute polymer solutions', *Journal of Fluid Mechanics* **43**, 689–710.

Peters, T. & Schumacher, J. (2007), 'Two-way coupling of finitely extensible nonlinear elastic dumbbells with a turbulent shear flow', *Physics of Fluids* **19**(6), 1–12.

Pope, S. B. (2000), *Turbulent flows*, Cambridge University Press.

Procaccia, I., L'vov, V. S. & Benzi, R. (2008), 'Colloquium: Theory of drag reduction by polymers in wall-bounded turbulence', *Reviews of Modern Physics* **80**(1), 225–247.

Ptasinski, P. K., Boersma, B. J., Nieuwstadt, F. T. M., Hulsen, M. A., van den Brule, B. H. A. A. & Hunt, J. C. R. (2003), 'Turbulent channel flow near maximum drag reduction: simulations, experiments and mechanisms', *Journal of Fluid Mechanics* **490**, 251–291.

Reischman, M. M. & Tiederman, W. G. (1975), 'Laser-Doppler anemometer measurements in drag-reducing channel flows', *Journal of Fluid Mechanics* **70**(02), 369–392.

Rudd, M. J. (1969), 'Measurements made on a drag reducing solution with a laser velocimeter', *Nature* **224**(5219), 587–588.

Ryskin, G. (1987), 'Turbulent drag reduction by polymers: a quantitative theory', *Physical review letters* **59**(18), 2059–2062.

Sreenivasan, K. R. & White, C. M. (2000), 'The onset of drag reduction by dilute polymer additives, and the maximum drag reduction asymptote', *Journal of Fluid Mechanics* **409**, 149–164.

Stone, P. & Graham, M. (2003), 'Polymer dynamics in a model of the turbulent buffer layer', *Physics of Fluids* **15**, 1247.

Sureshkumar, R., Beris, A. N. & Handler, R. A. (1997), 'Direct numerical simulation of the turbulent channel flow of a polymer solution', *Physics of Fluids* **9**(3), 743–755.

Swope, W., Andersen, H. C., Berens, P. H. & Wilson, K. (1982), 'A computer simulation method for the calculation of equilibrium constants for the formation of physical clusters of molecules: Application to small water clusters', *The Journal of Chemical Physics* **76**, 637.

Tabor, M. & De Gennes, P. G. (1986), 'A cascade theory of drag reduction', *Europhysics Letters* **2**(7), 519–522.

Temmen, H., Pleiner, H., Liu, M. & Brand, H. R. (2000), 'Convective nonlinearity in non-Newtonian fluids', *Physical Review Letters* **84**(15), 3228–3231.

Tennekes, H. & Lumley, J. L. (1972), *A first course in turbulence*, MIT press.

Terrapon, V. E., Dubief, Y., Moin, P., Shaqfeh, E. S. G. & Lele, S. K. (2004), 'Simulated polymer stretch in a turbulent flow using brownian dynamics', *Journal of Fluid Mechanics* **504**, 61–71.

Toms, B. A. (1948), 'Some observations on the flow of linear polymer solutions through straight tubes at large reynolds number', *Proceedings of the 1st International Congress on Rheology* **2**, 135–141.

Vaithianathan, T. & Collins, L. R. (2003), 'Numerical approach to simulating turbulent flow of a viscoelastic polymer solution', *Journal of Computational Physics* **187**(1), 1–21.

Virk, P. S. (1975), 'Drag reduction fundamentals', *AIChE Journal* **21**(4), 625–656.

Virk, P. S., Merrill, E. W., Mickley, H. S., Smith, K. A. & Mollochr, E. L. (1967), 'Toms phenomenon - turbulent pipe flow of dilute polymer solutions', *Journal of Fluid Mechanics* **30**, 305–328.

Vogel, W. & Patterson, A. M. (1964), *An experimental investigation of the effect of additives injected into the boundary layer of an underwater body*, Pacific Naval Laboratory, Defence Research Board of Canada.

Walsh, M. (1982), Turbulent boundary layer drag reduction using riblets, *in* 'AIAA, Aerospace Sciences Meeting', Vol. 1.

Warholic, M. D., Massah, H. & Hanratty, T. J. (1999), 'Influence of drag-reducing polymers on turbulence: effects of reynolds number, concentration and mixing', *Experiments in Fluids* **27**(5), 461–472.

White, C. M. & Mungal, M. G. (2008), 'Mechanics and prediction of turbulent drag reduction with polymer additives', *Annual Review of Fluid Mechanics* **40**, 235–256.

Zhou, Q. & Akhavan, R. (2003), 'A comparison of fene and fene-p dumbbell and chain models in turbulent flow', *Journal of Non-Newtonian Fluid Mechanics* **109**(2), 115–155.

Zimm, B. H. (1956), 'Dynamics of polymer molecules in dilute solution - viscoelasticity, flow birefringence and dielectric loss', *Journal of Chemical Physics* **24**(2), 269–278.